Novel Rates of OH induced Sulfur Oxidation. Implications to the Plume Chemistry of Jet Aircraft

H. Somnitz, G.Gleitsmann, R. Zellner[*]
Institut für Physikalische Chemie, Universität Duisburg Essen,Campus Essen, Essen, Germany

Keywords: Contrail formation, plume chemistry, OH + SO_2 kinetics

ABSTRACT: Novel rate coefficients for the most important and rate controlling sulfur oxidation reaction, OH + $SO_2 \rightarrow HSO_3$, over an extended range of pressure and temperature have been derived from ab initio quantum chemical/RRKM dynamical calculations. From these calculations the rate of oxidation of S(IV) to S(VI) under typical conditions of a jet aircraft plume is predicted to be considerably slower than previously accepted on the basis of interpolations of experimental data (i.e. Tremmel and Schumann, 1999). These kinetic results have been incorporated into a chemical-dynamical code of the jet regime of a B-747 airliner (BOAT code) to predict sulfur conversion efficiencies in this regime of less than 1%. It is concluded therefore that overall conversion efficiencies in the order of several % are caused by corresponding conversions in the combustor and/or turbine of the jet engine and not in the plume.

1 INTRODUCTION

A number of environmental aspects of aircraft emissions such as contrail formation and impact on cirrus formation have been suggested to depend on sulfuric acid formation from the fuel sulfur content (FSC) as a result of the rapid rates of oxidation of S(IV)in the engine and/or the plume. Despite this importance the chemical kinetic date base to assess this oxidation is far from being reliable.

Since many years, the abundance of H_2SO_4 in aircraft plumes has been identified as an important input parameter controlling aerosol dynamics. Up to date the S(VI)/S(IV) conversion of SO_2 has been identified to proceed following the Stockwell and Calvert (1983) mechanism, viz.

$$SO_2 + OH + M \rightarrow HSO_3 + M \qquad \text{(R1)}$$

$$HSO_3 + O_2 \rightarrow SO_3 + HO_2 \qquad \text{(R2)}$$

The subsequent formation of H_2SO_4 by addition of water molecules to SO_3 proceeds sufficiently fast for SO_3 and H_2SO_4 to be jointly denoted S(VI). Up to now conversion efficiencies in an aircraft plume in the order of $\varepsilon = 1\%$ could be reproduced in model calculations in which the emission indices of SO_3 and H_2SO_4 in the engine have been assumed to be zero (cf. for instance: Kärcher et al., 1995; Gleitsmann and Zellner, 1998).

On the other hand, higher conversion efficiencies have been postulated by Fahey et al. (1995) as well as Miake-Lye et al. (1998) which in turn require direct emissions of S(VI) species. Evidence for the latter has emerged from modelling calculations focusing on the gas phase chemistry inside combustor and turbine (Hunter, 1982; Brown et al., 1996; Lukachko et al., 1998; Starik et al., 2002), which yield conversion efficiencies in the order of $\varepsilon = 10\%$ even in the engine exit plane.

In order to resolve this discrepancy, both emission indices and rate constants of reaction (R1) need to be critically checked, especially since the available experimental kinetic data only cover limited temperature ranges $T \leq 400$ K (Atkinson et al., 1997; DeMore et al., 1997).

---

[*] *Corresponding author:* Reinhard Zellner, Institut für Physikalische Chemie, Universität Duisburg Essen, Campus Essen, D-45117 Essen, Germany. Email: reinhard.zellner@uni-essen.de

2 QUANTUM CHEMICAL CALCULATIONS

In the present study the recombination reaction of the OH radical with SO_2 has been investigated using current theoretical methods. Quantum chemical calculations were performed to locate the stationary points on the Potential Energy Surface (PES) for the recombination/dissociation process, including structures and vibrational frequencies calculated at the B3LYP/aug-cc-pVTZ(+1) and QCISD/6-311G(d,p) level of theory. Furthermore, the energetics are characterised by the application of G3X-theory which provides all sensitive data such as the critical energy barrier and the enthalpy of reaction (see Figure 1 below).

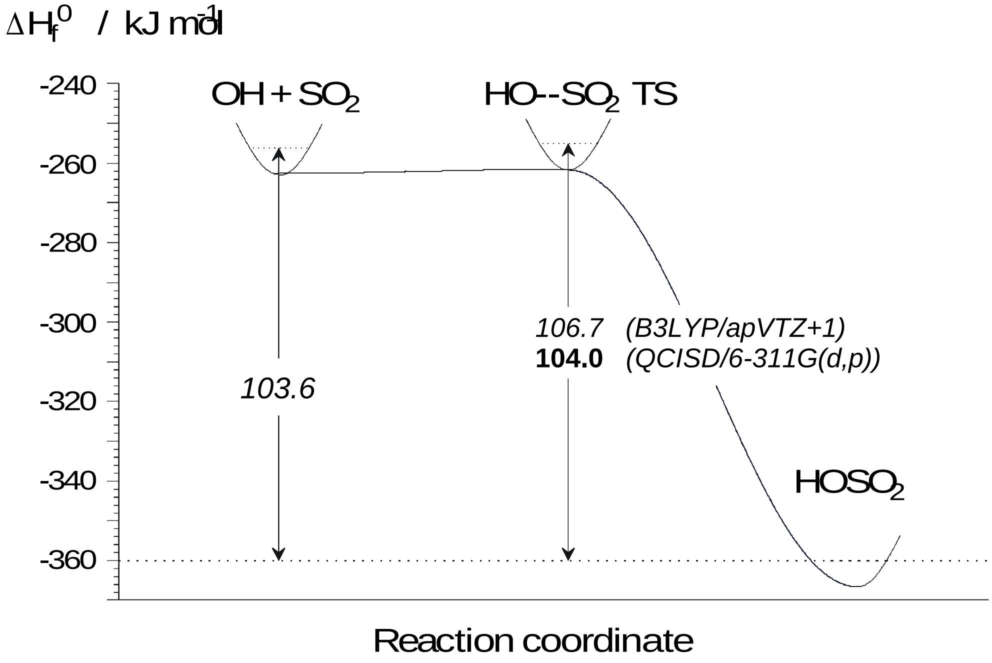

Figure 1. G3X calculated minimum energy path for the dissociation of HOSO2? OH+SO2.

The results obtained give clear evidence for a compact transition state with regards to the dissociation of $HOSO_2$. Combining the calculated enthalpy of formation for the $HOSO_2$ radical ($\Delta H_f^0(T=0\text{ K}) = -360.0$ kJ/mol) and the well known enthalpy of formation for OH and SO_2 this allows the calculation of the temperature dependent equilibrium constant $K_{eq}(T)$. In addition, a very shallow barrier ($\approx$ 0.5 kJ/mol) is predicted for the recombination process at $T = 0$ K.

3 STATISTICAL CALCULATIONS ON THE OH + SO_2 KINETICS

These novel data have been used as input to statistical kinetic calculations. Focussing on the reverse process (e.g. the $HOSO_2$ dissociation), RRKM-theory in conjunction with a subsequent solution of the master equation has been utilised to derive complete fall-off curves for the thermal decomposition of $HOSO_2$ in a weak collision scenario ($M = N_2$). The final rate coefficients for the recombination reaction of OH + SO_2 are derived by multiplication of the temperature dependent equilibrium constant and the temperature and pressure dependent rate coefficients of the back-dissociation (i.e. $k_{rec}(T,p) = K_{eq}(T)\ k_{diss}\ (T,p)$). The final results for $k_{rec}(T,p)$ are summarised in form of pressure dependent fall-off curves, shown in Figure 2 for selected temperatures in the range of 150 K to 1500 K.

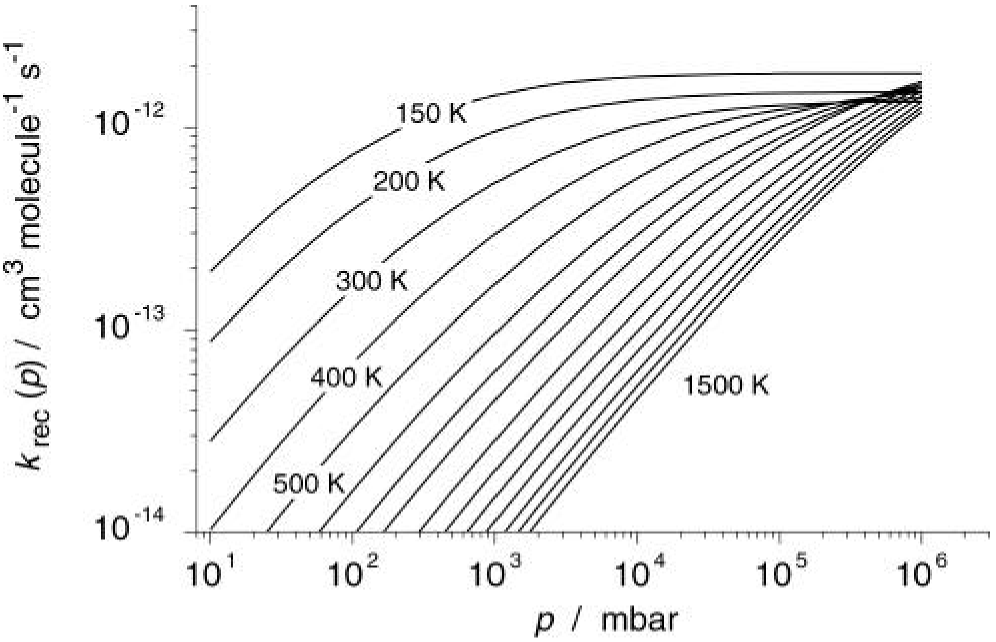

Figure 2. Complete fall-off curves for the recombination reaction of OH + SO_2.

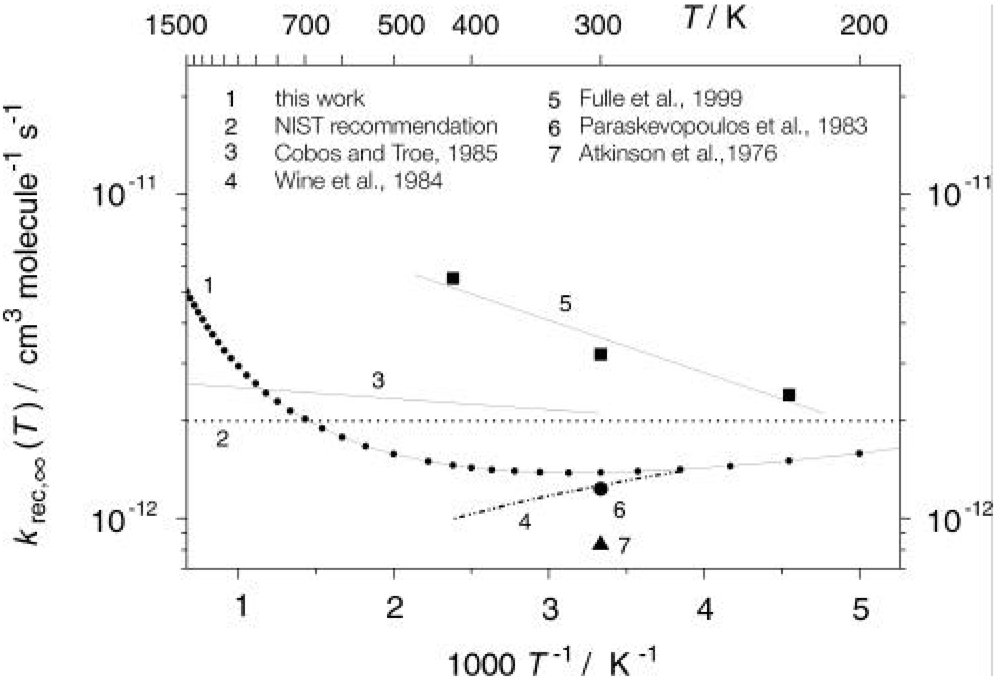

Figure 3. Calculated temperature dependence of the high pressure limiting rate coefficient of the OH + SO_2 recombination compared to extrapolated values known in the literature.

Further topics of this work cover the derivation of Arrhenius expressions for the low and high pressure limits as well as for specific pressures which are of interest in atmospheric chemistry. These have been extracted at each pressure from the "numerically exact" fall-off data, which are shown in the figure above. The resulting kinetic data are compared with rate constants suggested in the literature from experiments up to atmospheric pressures (Atkinson et al., 1997; DeMore et al., 1997) and recently reported measurements performed at temperatures between 220 K – 400 K and pressures up to 96 bar (Fulle et al.; 1999).

Although there is a fair agreement of the absolute magnitude of the rate coefficients at atmosperic pressures und temperatures, our calculation suggest up to a factor of three lower rate coefficients compared to previous extrapolations of the sparse experimental data into the pressure und temperature ranges of interest for combustion modelling. This is mainly due to the more complicated temperature behaviour of the high-pressure limiting rate coefficient of the recombination reaction, which changes from positive to negative Arrhenius-behaviour around T=300 K. This is demonstrated in Figure 3, together with a comparison of the available literature data.

The effective rate coefficient for reaction (R1) at 1 bar and as a function of temperature, together with recent values suggested by Tremmel and Schumann (1999) is shown in Figure 4. As can be seen the difference between both sets of data is in the order of a factor of 3 to 5 at temperatures below 700 K but amounts more than an order of magnitude in the combustion temperature regime.

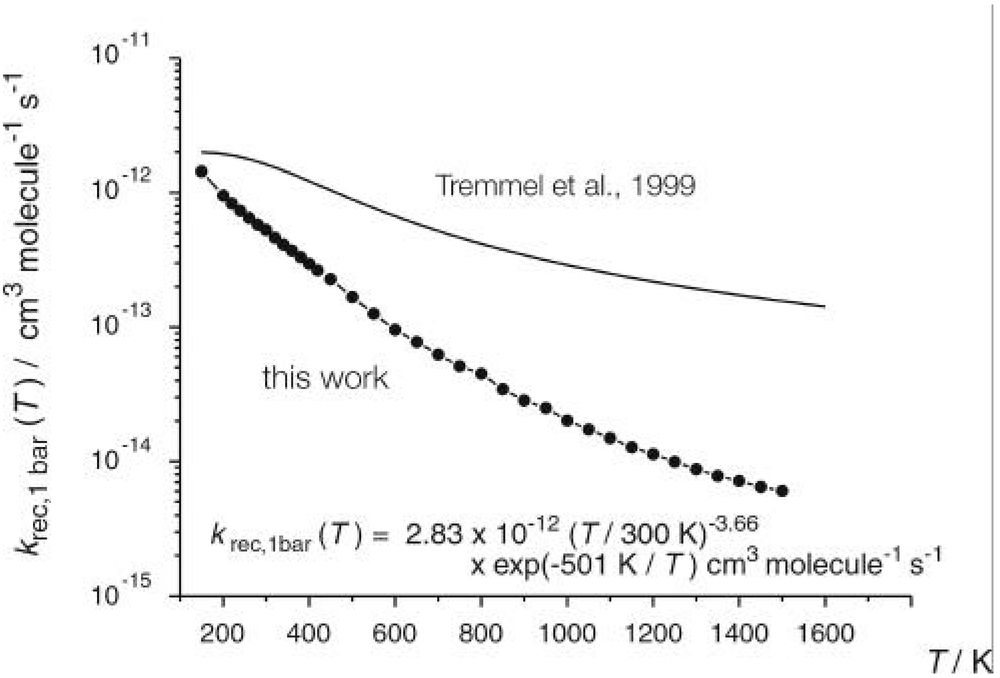

Figure 4. Calculated second order recombination rate coefficients at p = 1 bar compared to the values assumed in recent model simulations (Tremmel and Schumann, 1999).

4 CHEMICAL DYNAMICAL BOAT CODE

To describe the chemical/dynamical evolution of the plume the BOAT code has been used (Dash and Pergament, 1978). This model accounts for the detailed dynamical and thermochemical processes in the plume of a modern by-pass jet engine of cylindrical symmetry. In the model the jet plume is subdivided into a number of stream shells for which the Navier-Stokes equations are solved for turbulent flow and transport. Simultaneously, the complex gas phase reaction system is solved using local physical parameters such as temperature and species concentrations. All physical and chemical quantities are calculated as a function of the axial distance from the nozzle exit (cf. Figure 5) as well as of the normalised plume radius. The initial conditions chosen correspond to a CF6-80C2 engine of a B-747 airliner at cruise.

In order to implement our chemical code we have extended the original BOAT model to include, next to O_2, H_2, H_2O, CO, and CO_2, all O_x (O, O_3), HO_x (H, OH, HO_2), NO_x (NO, NO_2, NO_3, N_2O_5), NO_y (HONO, HNO_3, HNO_4), SO_x (SO_2, SO_3) and SO_y (HSO_3, H_2SO_4) species.

5 RESULTS

Whereas the water partial pressure in the young plume is given by the corresponding emission index and by subsequent dilution, the H_2SO_4 gas phase concentration is assumed to build up in the plume according to the Stockwell and Calvert (1983) mechanism, i.e. reactions (R1) and (R2) followed by

$$SO_3 + H_2O \rightarrow H_2SO_4 \qquad \text{(R3)}$$

The rate limiting step in this mechanism for all conditions of the plume (i.e. $T \leq 700$ K) is the recombination of SO_2 with OH radicals (R1). Only at higher temperatures where the decomposition of the HSO_3 adduct becomes reversible the reaction of $HSO_3 + O_2$ (Reaction R2) becomes rate determining. Therefore, the impact of reaction (R1) on the overall sulfur oxidation changes from kinetic control at low temperatures to thermodynamic control at higher temperatures. Both quantities ($k_1(p,T)$ and $K_{eq}(T)$) have been derived in the quantum chemical/statistical mechanical and dynamical calculations described above.

Since both the rate of reaction (R1) and the adduct concentration $[HSO_3]$ depend on the OH level, sulfur conversion is under all conditions a linear function of the OH concentration. A comparison of the kinetic schemes therefore should be based on comparable assumptions on the OH concentration at the engine exit as well as on the evolution of the OH field in the plume.

In Figure 5 we show the temporal evolution of SO_x and SO_y species as calculated for an OH emission index of 1.35×10^{-5} (Tremmel et al., 1998) for old and new HSO_3 kinetics. As can be seen from this figure the new HSO_3 kinetics produces substantially less S(IV) to S(VI) conversions (less than 1% during the evolution of the plume). It should be noted that using even smaller OH emission indices (i.e. 6×10^{-9}) will of course generate still lower conversions.

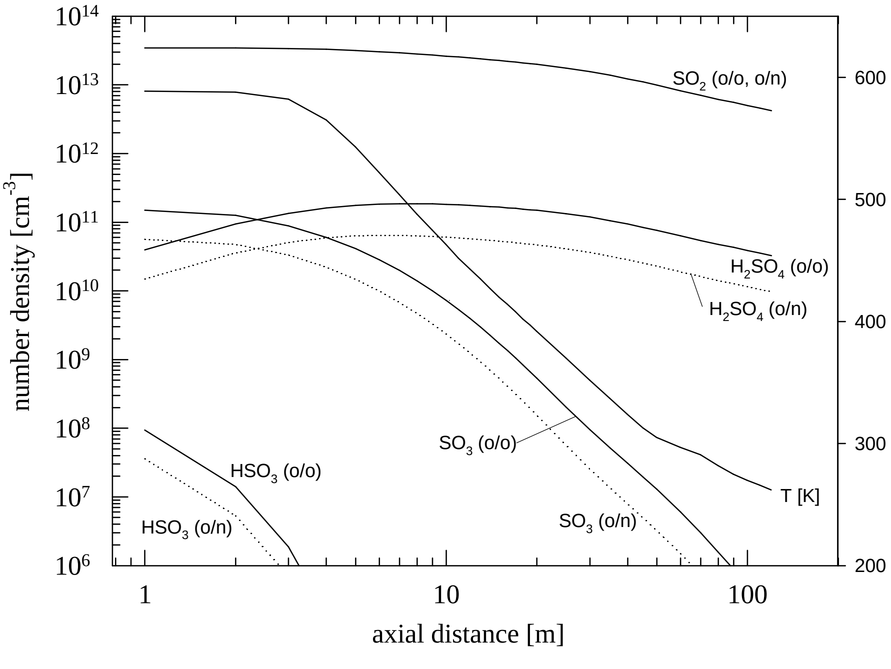

Figure 5. Evolution of SOx species for old (o) and new (n) HSO3 kinetics.

6 CONCLUSIONS

In view of improving the understanding of plume chemistry we have revised the conversion of SO_2 into SO_3 (H_2SO_4) in the jet regime of a B-747 airliner. The gas phase reaction scheme (Gleitsmann and Zellner, 1999) has been updated by the novel rate constants and the efficiency of SO_2 to SO_3/H_2SO_4 conversion from (R1) has been calculated using a chemical-dynamical code. Since the S(IV) to S(VI) conversion in the early jet regime is predicted to be significantly smaller, it is concluded from our work, that the well-known conversion ratio of S(IV) to S(VI) of several % as confirmed by a number of airborn experiments, can only be reproduced assuming sufficient formation of SO_3 or H_2SO_4 already inside the engine and/or the turbine. The plume effect on this ratio is less important.

7 ACKNOWLEDGEMENT

Financial support of this work by the EU-project PARTEMIS (GRD-1999-10819) is greatfully acknowledged.

REFERENCES

Atkinson, R., D.L. Baulch, R.A. Cox, R.F. Hampson, J.A. Kerr, M.J. Rossi, and J. Troe, 1997: Evaluated kinetic and photochemical data for atmospheric chemistry: Supplement VI - IUPAC subcommittee on gas kinetic data evaluation for atmospheric chemistry, *J. Phys. Chem. Ref. Data 26*, 1329-1499

Brown, R.C., M.R. Anderson, R.C. Miake-Lye, C.E. Kolb, A.A. Sorokin, and Y.Y. Buriko, 1996: Aircraft exhaust sulfur emissions, *Geophys. Res. Lett. 23*, 3603-3606.

Dash, S.M. and H.S. Pergament, 1978: A computational model for the jet entrainment in the vincinity of the nozzle boattail (The BOAT code), *NASA Contractors report 3075*.

DeMore, W.B., S.P. Sander, D.M. Golden, R.F. Hampson, M.J. Kurylo, C.J. Howard, A.R. Ravishankara, C.E. Kolb, and M.J. Molina, 1997: Chemical kinetics and photochemical data for use in stratospheric modeling. Evaluation 12., *JPL Publication 97-4*

Fahey, D.W. E.R. Keim, E.L. Woodbridge, R.S. Gao, K.A. Boering, B.C. Daube, S.C. Wofsy, R.P. Lohmann, E.J. Hintsa, A.E. Dessler, C.R. Webster, R.D. May, C.A. Brock, J.C. Wilson, R.C. Miake-Lye, R.C. Brown, J.M. Rodriguez, M. Loewenstein, M.H. Proffitt, R.M. Stimpfle, S.W. Bowen, and K.R. Chan, 1995: In situ observations in aircraft exhaust plumes in the lower stratosphere at midlatitudes, *J. Geophys. Res. 100*, 3065-3074.

Fulle, D., H.F. Hamann, and H. Hippler, 1999: The pressure and temperature dependence of the recombination reaction $HO^{\cdot} + SO_2 + M \rightarrow HOSO_2^{\cdot} + M$, *Phys. Chem. Chem. Phys. 1*, 2695-2702.

Gleitsmann, G. and R. Zellner, 1998: A Modelling Study of the Formation of Cloud Condensation Nuclei in the Jet Regime of Aircraft Plumes, *J. Geophys. Res. 103*, 19543-19555.

Gleitsmann, G. and R. Zellner, 1999: The aerosol dynamics of H_2O-H_2SO_4-HNO_3 mixtures in aircraft wakes. A modeling study, *Phys. Chem. Chem. Phys. 1*, 5503-5509.

Hunter, S.C., 1982: Formation of SO_3 in gas turbines, *T. ASME J. Eng. Power 104*, 44-51.

Kärcher, B., Th. Peter, and R. Ottmann, 1995: Contrail Formation: Homogeneous Nucleation of H_2SO_4/H_2O droplets, *Geophys. Res. Lett. 22*, 1501-1504.

Lukachko, S.P., I.A. Waitz, R.C. Miake-Lye, R.C. Brown, and M.R. Anderson, 1998: Production of sulfate aerosol precursors in the turbine and exhaust nozzle of an aircraft engine, *J. Geophys. Res. 103*, 16159-16174.

Miake-Lye, R.C., B.E. Anderson, W.R. Cofer, H.A. Wallio, G.D. Nowicki, J.O. Ballenthin, D.E. Hunton, W.B. Knighton, T.M. Miller, J.V. Seeley, and A.A. Viggiano, 1998: SO_x oxidation and volatile aerosol in aircraft exhaust plumes depend on fuel sulfur content, *Geophys. Res. Lett. 25*, 1677-1680.

Starik, A.M., A.M. Savel'ev, N.S. Titova, and U. Schumann, 2002: Modeling of sulfur gases and chemiions in aircraft engines, *Aerosp. Sci. Technol. 6*, 63-81.

Stockwell, W.R. and J.G. Calvert, 1983: The mechanism of the HO-SO_2 reaction. *Atmos. Environ. 17*, 2231-2235.

Tremmel, H.G., H. Schlager, P. Konopka, P. Schulte, F. Arnold, M. Klemm, and B. Droste-Franke, 1998: Observation and model calculations of jet aircraft exhaust products at cruise altitude and inferred initial OH emissions, *J. Geophys. Res. 103*, 10803-10816.

Tremmel, H.G: and U. Schumann, 1999: Model simulations of fuel sulfur conversion efficiencies in an aircraft engine: Dependence on reaction rate constants and initial species mixing ratios. *Aerosp. Sci. Technol. 3*, 417-430.

Determination of Soot Mass Fraction, Soot Density and Soot Fractal Character in Flame Exhaust Gases (PAZI)

C. Wahl[*], M. Kapernaum, V. Krüger, P. Rainer, M. Aigner
DLR-Institut für Verbrennungstechnik, Stuttgart Germany

Keywords: Soot mass, soot density, fractal character, SMPS

ABSTRACT: The DLR – Soot Generator was used as a variable and well defined soot source. The particle mean diameter of the log normal size distribution can easily be shifted between 6nm and 250nm. This soot loaded exhaust gas is sucked through a quartz fiber filter via a computer controlled gas sampler. The soot particles are trapped on a quartz fiber filter. This special quartz filter has a sampling efficiency better than 99,9% for particles between 6nm and 250nm. The carbon load on the quartz filter is burned in an oxygen atmosphere. The resulting carbon dioxide concentration is measured with a Fourier Transform IR spectrometer (FTIR). If the gas sampling volume, the gas cell volume and the carbon dioxide concentration is known, a soot mass fraction can easily be calculated. The corresponding size distribution, number concentration and volume concentration are measured by a Scanning Mobility Particle Sizer system (SMPS). Using the soot mass of the filter experiment and the soot volume of the SMPS measurements, a soot density was calculated. This soot density is based on the mobility diameter of the fractal soot particles. The quotient of graphite density and calculated soot density gives the fractal character of the soot.

1 INTRODUCTION

The characterisation of soot nanoparticles by diameter, volume or fractal dimension is ambiguous. Always the corresponding measuring technique must be known, e.g. is it a mobility diameter, an aerodynamic diameter, a geometric diameter and so on (Hinds, 1999).

Modern soot measurement techniques like Laser Induced Incandescence (LII) or Scanning Mobility Particle Sizer (SMPS) give a so called soot volume fraction but no absolute soot mass values. The soot mass fraction given by LII or SMPS are calculated with an assumed soot density. But what is the density of a fractal soot nanoparticle?

2 SOOT SOURCE AND FILTER TEST

For our experiments we used the DLR-Soot Generator (Wahl) as a well defined and stable soot source. The flame soot particles of this generator show a log normal size distribution. The mean diameter of the log normal size distribution can easily be shifted from 6 nm to 250 nm. The number concentration and particle size distribution (PSD) is stable and reproducible.

In a first experiment we checked the trapping efficiency of the quartz fiber filters. The soot generator aerosol was sucked through a fiber filter and the size distribution and number concentration in front and behind the filter was measured with SMPS. The results are shown in the following table:

mean diameter of PSD	trapping efficiency of quarz fiber filter
7.5 nm	99.9 %
36.8 nm	99.99 %
122 nm	99.999 %

---

[*] *Corresponding author:* Claus Wahl, DLR-Institut für Verbrennungstechnik, Pfaffenwaldring 38, 70569 Stuttgart, Germany. Email: claus.wahl@dlr.de

3 FILTER AND SMPS MEASUREMENTS

Due to the excellent trapping efficiency of the fiber filter, it is possible to get the absolute soot mass fraction of the exhaust gas.

Before taking filter soot samples, the quartz fiber filters are heated to 800 °C, in order to burn all organic material on the filter. Then, with a computer controlled gas sampler, a known volume of aerosol was sucked through the filter. In a reaction tube, the volatile organic fraction of the soot loaded filter was burned at 480 K in an oxygen atmosphere. After that procedure the reaction tube was cooled down to room temperature and evacuated again. The remaining black carbon on the filter was burned in a oxygen atmosphere at 800 °C. After cooling down, the resulting CO_2 concentration was measured with a FT-IR spectrometer. The FT-IR system was calibrated with test gases of known CO_2 content. With known exhaust gas sampling volume and known FT-IR gas cell volume, the black carbon mass is calculated via the CO_2 Signal.

The SMPS instrument classifies particles by the so called mobility diameter. Using a sphere model gives the aerosol volume. Our system can work in two measuring ranges, the low flow mode and the high flow mode. If the mean diameter of the measured size distribution is in the mid range of the measuring range, high flow and low flow measurements should give the same volume.

SMPS measurements in low flow mode as well as in high flow mode have been done before and after filter sampling. The mean SMPS soot volume in high flow mode was 3.03E+11 [nm^3/ cm^3]. The mean SMPS soot volume in low flow mode was 3.78E+11 [nm^3/ cm^3].

The gives a soot density of 0.74 g/cm^3 (high flow) and 0.59 g/cm^3 (low flow). The mean soot density of a ethylene flame at 1 bar is d_{MD} ~ 0.66 g/cm^3 . (We name the density d_{MD} ,because it is based on the mobility diameter.)

Assuming the primary soot particles consist of graphite similar structures, the density of the primary particles is ~2.2 g/cm^3 like graphite. Therefore a “soot fractal character” can be calculated by dividing the graphite density through the soot density. For our ethylene soot the determined “fractal character” is 2.2 g/cm^3 / 0.66 g/cm^3 = 3.33 =fc_{MD} (again based on mobility diameter).

4 CONCLUSION

A method to determine soot mass, soot density and soot fractal character is shown. Flames under different conditions, or flames of different fuels will have different soot density and soot fractal character. Whenever soot densities are published, it is absolutely necessary to give the method of determine the particle diameter or volume. Because of the fractal character of the soot agglomerates, only soot densities determined with the same method can be compared.

REFERENCES

Hinds, W. C., Aerosol Technology. John Wiley & Sons, New York 1999

Wahl, C., M. Aigner, V. Krüger, Russgenerator, Vorrichtung und Verfahren zur kontrollierten Erzeugung von Nano- Russpartikeln. Deutsche Patentanmeldung, Amtl. Aktenzeichen 102 43 307.0

Overview of results from the NASA experiment to characterize aircraft volatile aerosol and trace species emissions (EXCAVATE)

B.E. Anderson[*], E. Winstead, C. Hudgins, J. Plant, H.-S. Branhan, and L. Thornhill
NASA Langley Research Center, Hampton VA, USA

H. Boudries, M. Canagaratna, R. Miake-Lye, J. Wormhoudt, and D. Worsnop
Aerodyne Research Incorporated, Billerica, MA, USA

T. Miller, J. Ballenthin, D. Hunton, and A. Viggiano
Air Force Research Laboratory, Hanscom Field, MA, USA

D. Pui and H.-S. Han
University of Minnesota, Minneapolis, MN, USA

D. Blake and M. McEchern
University of California at Irvine, Irvine CA, USA

Keywords: particle formation, particle growth, chemiions, black carbon, aerosol composition

ABSTRACT: EXCAVATE was conducted at NASA Langley Research Center in Hampton Virginia during January, 2002, and obtained detailed measurements of emissions from Langley's T-38 and B-757 aircraft to determine ion densities; the fraction of fuel S converted from S(IV) to S(VI); the concentration and speciation of volatile aerosols and black carbon; and gas-phase concentrations of hydrocarbons in the exhaust of a typical commercial airliner, all as a functions of engine power, fuel composition, and plume age. Our observations indicate that chemiion densities were very high in the exhaust plumes, consistent with values that are presently being used in microphysical models of aerosol formation in exhaust plumes. Both aircraft were found to emit high concentrations of organic aerosols, particularly at low power settings and to produce black carbon concentrations that increased with engine power. Total particle emission indices were typically a factor of 10 higher at 35 meters than at 1 meter behind the engines due to formation of new particles. The concentration of sulfate aerosol was directly dependent upon the fuel sulfur level and increased considerably as sampling took place progressively further downstream from the exhaust plane. For the B757, organic aerosol emissions were very high at engine start and took several minutes to reach much lower, equilibrium values after changes in engine power. This was particularly notable when the engines were reduced from high to low power as might occur during taxi and landing.

1 INTRODUCTION

Aircraft are prolific sources of both primary and secondary aerosol particles [i.e. Anderson et al., 1999]. To assess and predict the impact of these aerosols upon the environment requires a complete understanding of their chemical and microphysical properties and how they are regulated by engine design, temperature and fuel composition, and change as the exhaust plume ages and mixes into the background atmosphere. To gain this information, NASA and European funding agencies have sponsored a number of laboratory and field investigations to characterize and quantify aircraft particulate emissions. Projects such as SUCCESS [Toon et al., 1998], SNIF [Anderson et al., 1998], SONEX [Thompson 1999], POLINAT [Schumann et al., 1998], SULFUR 1-7 [Schumann et al., 2002] have provided a wealth of information regarding aircraft aerosol concentrations and volatility [i.e. Anderson 1998], size distributions [i.e. Brock et al., 2000], and black carbon fraction [Petzold et al., 1999]. These and/or other studies have also examined the impact of fuel sulfur contaminants

---

[*] *Corresponding author:* Bruce Anderson, MS483, NASA Langley Research Center, Hampton, VA, USA; bruce.e.anderson@nasa.gov

upon secondary aerosols formation [i.e., Miake-Lye et al., 1998] or, more challengingly, determined the fraction of fuel sulfur that is oxidized to form sulfuric acid in the near field behind the aircraft [i.e., Schumann et al., 2002]. Other studies have characterized and quantified chemiion species in exhaust plumes because these are suspected to play a significant role in new particle formation [Arnold et al., 1999].

Although these investigations have greatly advanced our understanding of particle production by aircraft, a number of significant questions remain unanswered. For example, how does fuel S oxidation vary as a function of engine power and fuel S content? Does unburned fuel and engine oil contribute to formation of aerosols in engine exhaust plumes? In addition, a majority of the information gathered in these studies are pertinent to upper tropospheric/lower stratospheric aircraft operation. How well can these observations be extrapolated to ground-based operations where engines often operate at non-optimum power and fuel/air ratios?

To address these issues, NASA's Atmospheric Effects of Aviation Project (AEAP) and Ultra-Efficient Engine Technology (UEET) Program sponsored the Experiment to Characterize Aircraft Volatile Aerosol and Trace-Species Emissions (EXCAVATE). A ground-based study conducted in an open-air facility, EXCAVATE had as objectives to determine the concentration of chemiions, volatile aerosols, aerosol precursors, black carbon, and selected gas-phase species within the exhaust plume of a modern commercial turbo-fan engine as a function of engine power, fuel composition, and plume age. The experiment took advantage of recent advances in instrumentation and paid particular attention to determining time-dependent aerosol physical properties and composition as well as chemiion speciation. Significant efforts were made to minimize sample line lengths, characterize probe penetration efficiencies and transmission losses, and evaluate the impact of sampling strategies upon measured parameters. Experimental details and summary results in selected focus areas are provided in the paragraphs below.

2 EXPERIMENT

EXCAVATE sampled emissions from the NASA Langley Boeing 757 (B757) and T-38A Talon. The B757 is powered by a pair of Rolls Royce, RB-211-535E4 Turbofan engines as are ~80% of all B757s in service. These three-shaft, high bypass ratio engines produce 40,100 lbs thrust and have a single-stage wide-chord fan, six-stage IP compressor, six-stage HP compressor, single annular combustor, single-stage HP turbine, single-stage IP turbine and a three-stage LP turbine. Langley's T-38 is powered by a pair of J85-GE-5A turbojet engines that produce 3850 lbs thrust. Both aircraft nominally burn commercial Jet A or military JP-5 fuels.

The engine tests were conducted at Langley's aircraft "run-up" facility, a large concrete pad with a blast fence that deflects engine exhaust upward to prevent damage to neighboring vegetation. Anchors are embedded at numerous places in the pad to provide restraining points for aircraft during high power engine runs and were used to secure the sampling probe test stand and sample/electric lines to prevent them from being blown back by the exhaust blast. During tests, the aircraft were parked in front of the blast fence and chocked in place to keep them stationary during the high power engine runs. The probe test stand (Figure 1) was positioned behind engine so that the tips of the sampling probes mounted upon it were 1 m downsteam and on the centreline of the turbine exhaust plane. For the B757, an additional aerosol-sampling inlet was affixed to the blast fence 25 m downstream of the engine exhaust plane. To obtain aerosol samples at 10 and 35 m, the aircraft was rolled forward 9 m and re-chocked. In the case of the T-38, additional aerosol inlets were mounted on weighted stands positioned 10 and 25 m behind the engine exhaust plane. Gas phase measurements were acquired only at 1 m separation distance.

The primary aerosol-sampling probe used in the experiment was carefully designed to introduce a concentric flow of dilution gas as close behind the nozzle tip as possible. Tests conducted at the University of Minnesota using sulfate aerosols indicate the probe is > 80% efficient for extracting particles > 20 nm in diameter from hot gas flows. Boil-off from a liquid N_2 cylinder was used for dilution gas and the dilution ratio was set to approximately 8:1 by monitoring the ratio of CO_2 mixing ratio in the aerosol sample to that in the exhaust plume. Sample air was piped from the probe ~10 m to the aerosol instrument trailer through a combination of 0.5 inch stainless steel and carbon impregnated conductive tubing. The secondary aerosol sampling inlets were constructed from 0.25 inch Swagelok Tees and stainless tubing, raised to the height of the engine centreline, and connected with 0.5 inch stainless, copper or conductive tubing to 0.5 inch stainless steel ball valves located within the aerosol instrument trailer. The ball valves, in turn, were attached to a common sampling manifold to allow the operator to select sample air from one of the two or three inlets positioned behind the aircraft. The probe used to collect gaseous samples was constructed from standard 2" thick-walled stainless steel pipe and had a tear-drop shaped shield welded to the downstream side to reduce its coefficient of friction and provide protection to wires and tubes connected to sensors mounted near its tip (Figure 2). It was connected with a short length of thin-walled tubing to a sampling manifold located within the test stand that supplied sample air to the Air Force Lab Chemical Ionization (CIMS) and Ion (IMS) Mass Spectrometers and the Aerodyne Tuneable Diode Laser (TDL) Spectrometer and a small CO_2 monitor. The primary aerosol sampling inlet, a Gerdien-tube condenser, a pitot-static tube and a thermocouple mounted were welded on the top and sides of the gas probe, respectively (Figure 2). Along with the TDL, IMS, and CIMS, pressure transducers for the pitot tube, a thermocouple readout, and an electrometer to measure current on the Gerdien Condenser were all placed inside the base of the probe test stand.

Figure 1. Langley B-757 with test stand and probes positioned 1 meter behind engine exhaust plane.

Figure 2. Gas and aerosol inlet probes along with pitot tube and Gerdien Condensor used in 1 and 10 meter sampling behind the B-757.

A list of the measurements that were acquired during EXCAVATE is provided in Table 1. Langley (LaRC) was responsible for measuring the aircraft engine parameters, exhaust CO_2 mixing ratio, total CN concentrations, black carbon, and submicron aerosol size distributions using a Differential Mobility Analyzer (DMA) and Optical Particle Counter (OPC). Aerodyne Research, Inc. made measurements of aerosol composition using their new Aerosol Mass Spectrometer as well as operated the TDL system that determined mixing ratios of CO_2, SO_2, SO_3, and HONO (i.e., Whitefield et al., 2002). The University of Minnesota (UM) provided nucleation mode size distributions for heated and unheated samples using their rapid scanning, nano-Aerosol Size Analyzer (nASA). Air Force Research Lab (AFRL) operated a CIMS and IMS, and a Gerdien tube condenser to measure a variety of species including SO_2, H_2SO_4, HNO_3, total ion densities and ion speciation.

EXCAVATE included a number of sulfur related objectives that required burning fuels of known and varying S concentrations. Although we had originally planned to obtain a low S Jet-A fuel (< 5 ppm) and produce a medium (i.e., 100 ppm) and high S (800 ppm) fuels from it by adding Tetrahydrathiophene (THSP), time and funding constraints forced us to purchase a JP-5 fuel from the local government contractor and to produce a single, higher S content fuel by mixing in THSP sufficient to boost the S level by ~800 ppm. We thus ended with two fuels from a single hydrocarbon matrix containing 1050 and 1820 ppm S for use in the B757 fuel S tests. A third JP-5 fuel obtained from the NASA Langley stock and containing 810 ppm S was used in the T-38 runs and in B-757 experiments to test the sampling system and to fill the role of low S fuel when the supply of 1050 ppm S fuel was depleted.

Exhaust plumes from both the Langley T-38 and B-757 were sampled during EXCAVATE, with the primary interest in sampling the T-38 being to test and perfect our measurement procedures, determine optimum dilution ratios, to evaluate sampling loses, and to obtain information on particle formation and growth as the exhaust plume cooled and dispersed. Thus, the T-38 test matrix included collecting samples at 3 different distances downstream from the engine exhaust plane (1, 10, and 25 m) as the engine was operated at power settings of 50 (idle), 60, 70, 80, 90, and 100% (takeoff) of maximum turbine rpm. Additionally, the 1 m inlet probe was operated at a number of dilution ratios to evaluate the impact of dilution upon particle losses and measured size distributions. Our objectives in sampling the B-757 aircraft additionally included determining the influence of fuel S on particle formation, thus its test matrix included collecting samples 1, 10, 25 and 35 m downstream of the exhaust plane as the engine was operated at engine pressure ratios (~power) of 1.03 (idle), 1.15, 1.30, 1.40, and 1.50 (1.70 is takeoff) and burned fuels containing 810, 1050, and 1820 ppm S.

Table 1: Exhaust Characterization Measurements

Species/Parameter	**Technique**	**Group**
Engine Parameters	Aircraft Systems	LaRC
Fuel Sulfur Content	X-ray Fluorescence	LaRC
Exhaust Parameters (T, P, Velocity)	Pitot tubes, thermocouples	LaRC
Sample and Exhaust CO_2	IR spectrometer	LaRC
Aerosol Size and Volatility (3 to 100 nm)	nASA	UM
Aerosol Size (10 to 1000 nm)	DMA, OPC	LaRC
Black Carbon	PSAP	LaRC
Nonmethane Hydrocarbons	Grab Samples	UCI
SO_2, CO_2, SO_3, H_2O, HONO	TDL	Aerodyne/GRC
Aerosol Composition	Mass Spectrometer	Aerodyne
H_2SO_4, HONO, HNO_3, SO_2	Chemical Ion Mass Spect	AFRL
Ion Density	Gerdien Condenser	AFRL
Ion Composition	Ion Mass Spec	AFRL

3 SUMMARIES OF RESULTS

3.1 Chemiions (AFRL MS Group)

Negative ion mass spectra were obtained for chemiions in the T-38 exhaust plume for engine rpm values of 49.5, 60, 70, 80, 90, and 100% of maximum. An example of the IMS mass spectra is shown in Fig. 3. The results show that the total number of ions increases with engine rpm (with one exception discussed below) and that the mass spectrum moves to lower ion mass. Both observations are a result of the increased temperature and higher exhaust velocity (faster sampling) at higher rpm. At 100% rpm the major ion peak is HSO_4^-, which results from ion-molecule reactions taking place between the combustor and the sampling orifice of the IMS. Some of the ion masses are as yet unassigned to a particular molecular species and may remain unassigned. In earlier work the unidentified masses were declared to be “oxyhydrocarbons,” and this may be the best one can do at the present time.

The “total ion” data, as illustrated in Fig. 3 may be used to estimate the ion concentration (plasma density) at the engine exhaust plane. The ion concentration at the IMS sampling orifice is much lower than at the engine plane because of ion-ion mutual neutralization reactions that take place in the exhaust stream. The ion-ion mutual neutralization reaction rate constant is about 10^{-26} cm^6 s^{-1} at atmospheric pressure and is approximately independent of the ion type because the neutralization is mobility-limited at this pressure. A temperature correction must be estimated. To determine the ion concentration at the engine exhaust plane from the total ion data, one needs (a) the detection efficiency of the IMS, (b) the gas temperature, and (c) the sampling time or velocity of the exhaust gas. Item (a) decreases with temperature because ions are swept into the IMS sampling orifice by the gas in the sampling pipe, and the throughput of gas is temperature dependent. The detection efficiency of the IMS was measured at room temperature in the laboratory at 1 atm pressure and found to be 980 cm^{-3} ion^{-1} s^{-1}. The result of the calculations, effectively working backwards from the total ion signal to the engine exhaust plane, is shown in Fig. 4. An additional upward correction of the exhaust ion concentration may be made at a later date due to the problem of sampling from a high-velocity stream. The result that the ion concentration at 100% maximum rpm is lower than that at 90% is counterintuitive, but (a) the measurements were quite clear, and (b) both AFRL and NASA-LaRC measured a lower temperature at 100% maximum rpm than at 90%.

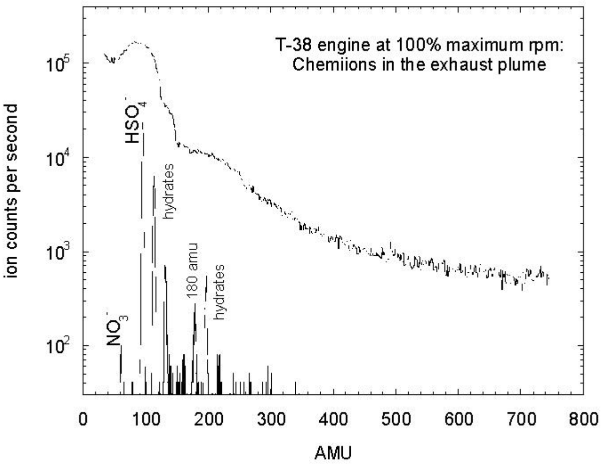

Figure 3. Mass analysis of chemiions in the exhaust of the T-38 jet engine at a point 3.22 m following the engine exhaust plane, at 100% of maximum compressor rpm. The upper line is the total transmitted ion current through the mass spectrometer at zero resolving power.

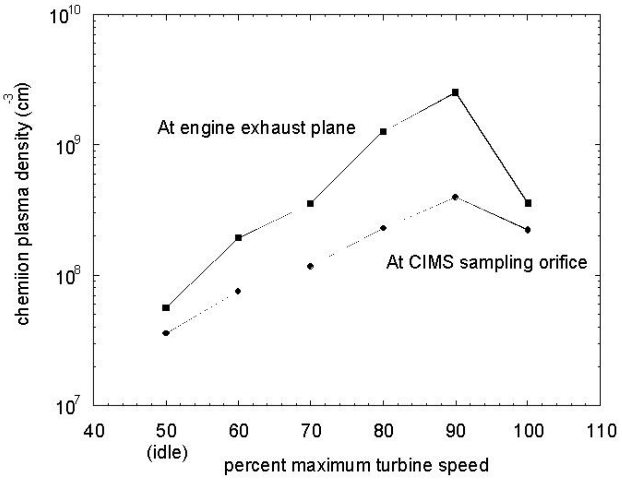

Figure 4. The result of modeling backwards from the total IMS ion signal to obtain the ion concentration at the exhaust plane of the T-38 jet engine. Ion loss in the sampling path is due to ion-ion mutual neutralization.

3.2 HONO (Aerodyne TDL Group)

In the previous NASA/QinetiQ tests (Whitefield et al., 2002), HONO had been measured, both at the combustor exit and, at higher levels, at the engine exit. However, due to substantial etalon fringes, the HONO concentrations measured in those tests had been near the detection limit. Also, because sampling was carried out in a single configuration, it was difficult to rule out the possibility that HONO was being formed from NO and H_2O in the sampling probe.

In the EXCAVATE measurements behind the B757, the detection limit was as low as 100 ppbv in the multipass cell. At high powers, over 2 ppmv of HONO was observed. When converted to emission indices, the B757 HONO results shown in Figure 5 show a clear power dependence, decreasing with decreasing power at the two lower settings but roughly constant at the highest three settings. When the sampling point was moved back to 10m behind the engine, the HONO concentration may have decreased somewhat, though when the total error estimates shown in the figure are taken into account, this decrease is not necessarily significant. In contrast to the B757, which showed much more HONO than observed in the engine exhaust sampled in the 2001 NASA/QinetiQ tests, the T-38 HONO levels were not measurable, meaning they were well below 100 ppbv in the multipass cell. Thus, the EXCAVATE observations contain three points of comparison which suggest HONO formation in the probe is not a serious problem. In the move from sampling at 1m to sampling at 10m, the temperature and composition of the exhaust have changed substantially, but the HONO fraction of exhaust species has not. In both the case of B757 engine power variation and in the change from B757 to T-38 exhaust, the exhaust properties have changed less than the HONO concentration. This is especially true for the comparison between engines: the change in HONO is more than an order of magnitude, while changes in temperature, NO and H_2O are much less than that. At high power, over 2 ppmv of HONO was detected in the B757 exhaust. These values correspond to EI(HONO) values of up to 0.25 (if nominal values apply to this exhaust, this is somewhat less than 5% of the NO).

3.3 Aerosol Physical Properties (Langley and U. Minnesota Aerosol Groups)

In measurements recorded behind the T-38, aerosol number EIs varied from 0.8 to 23 x 10^{-15} kg^{-1} and averaged 6 x 10^{-15} kg^{-1}; aerosol mass EIs ranged from ~8 to 465 mg kg^{-1}, and averaged 111 mg kg^{-1}; black carbon varied from 17 to 400 mg kg^{-1} and averaged 111 mg kg^{-1}; the geometric mean diameter of the number-size distribution varied from 15 to 61 nm, and averaged 23 nm; and the volume mean diameter (VMD) ranged from 31 to 91 nm, and averaged 52 nm. At the 1 m sampling distance where the aerosol should be composed primarily of soot and other nonvolatile species (i.e., metals, PAHs), Number EIs values peaked at ~5 x 10^{15} kg^{-1} at idle, then dropped by >60% and became relatively constant at turbine speeds above 70% of maximum rpm. Conversely, Mass EIs were ~150-200 mg kg^{-1} below 70% power, then increased by a factor of two upon reaching 100% power. This inverse relationship between Number and Mass EIs suggests that the particle size increases with engine power which is borne out by the calculated values for GMD and VMD; these parameters increased from 23 to 30 nm and 48 to 66 nm, respectively, in going from idle to full military power. Black Carbon EIS increased from ~85 mg kg^{-1} at idle to 272 mg kg at 100% power and the ratio of BC to Mass EIs changed from 0.44 to 0.67 across this power range, indicating that, perhaps, a higher fraction of the aerosol emissions were composed of nonvolatile organics at the lower combustor temperatures characteristic of low power conditions. Ten meters downstream from the engine exhaust plane, aerosol Number EIs were typically higher and VMD's lower than at 1 m, suggesting that low volatility species had condensed to form new particles as the plume cooled. Because of their small sizes, these aerosols did not significantly add to the mass loading except at idle where the Mass EIs were twice the value observed at 1 m. This might be related to the longer growth period experienced by the aerosols in the low velocity plume, the propensity of the engine to emit more condensable hydrocarbons at low powers, or it might simply be caused by poor sampling statistics. Samples collected from the 25 m inlet exhibited even higher Number EIs but the trend in Mass EIs could not be delineated because, at that sampling distance, concentrations were too variable across the 60 second scan time of the DMA to yield reliable size distributions.

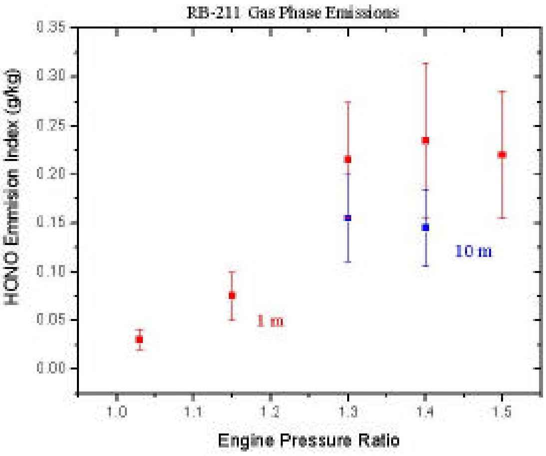

Figure 5. B-757 HONO emissions as measured by a TDL system at 1 and 10 m behind the engine exhaust plane.

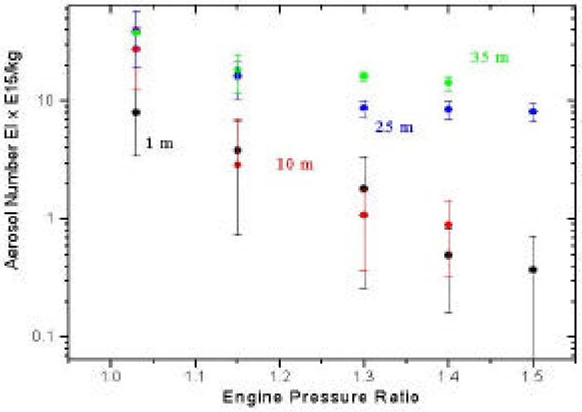

Figure 6. B-757 aerosol number EI for 1820 ppm S fuel as measured at 1, 10, 25 and 35 m behind the engine exhaust plane.

Emissions from the B-757, RB-211 engine were even more variable than those from the T-38. Number EIs ranged 0.01 to 85 x 10^{15} kg-1, and averaged ~9 x 10^{-15} kg^{-1} for the entire data set. Mass EI values ranged from ~10 to >9000 mg kg^{-1} and averaged ~500 mg kg^{-1}; black carbon varied from 0.6 to 218 mg kg^{-1} and averaged 59 mg kg^{-1}; the GMD of the number-size distribution varied from 10 to 101 nm, and averaged 27 nm; and VMD values ranged from 31 to 110 nm, and averaged 52 nm. Although fuel S content played an identifiable role, engine power and sampling distance were the primary factors that governed this variability. For 1820 ppm S fuel and 1 m sampling case, Number EIS dropped from ~8 x 10^{15} to 0.37 x 10^{15} kg^{-1}, or more than a factor of 20, upon increasing power from idle (1.03 EPR) up to 1.5 EPR (Fig. 6). Similarly, for 1820 ppm S and a power setting of 1.4 EPR, Number EIs increased from ~0.4 x 10^{15} to 14.3 x 10^{15} kg^{-1}, or a factor of 38, between 1 and 35 meters downstream of the engine exit plane. Results from the 1050 ppm S fuel runs exhibited similar trends. A large fraction of the particles present at low engine powers were composed of organic material, thus it is likely that the decrease in particle number emissions with increasing EPR is caused by more efficient combustion of low volatility fuel components as the engine exhaust gas temperature increases from ~355^{o}C at idle to ~630^{o}C at 1.5 EPR. The increasing number concentrations with plume age are caused by formation of a nucleation mode within the aerosol size distribution (Figs 7 and 8) and is also consistent with Aerodyne observations of increasing amounts of relatively small-diameter sulfate aerosols within aged plumes. As for mass emissions, except for the idle condition where the engine emitted variable and sometimes significant amounts of organic aerosols depending on the temperature history of the combustor, EIs tended to increase with power. For 1820 ppm S and 1 m sampling distance, Mass EIs increased from 64 to 98 mg kg^{-1} in going from 1.15 to 1.5 EPR. This positive correlation between Mass EIs and EPR appears to be driven by the tendency of the engine to produce greater amounts of black carbon (BC) aerosols at higher temperatures/engine powers. Comparing DMA mass EIs with BC EIs, for 1 m sampling, we deduce that BC generally accounted for < 10% of total aerosol mass emissions at idle but almost 100% for the higher power settings. Mass EIs increased with plume age, however, presumably due to condensation of low-volatility material as the emissions cooled. For 1820 ppm S fuel and an EPR of 1.4, Mass EIs increased from 95 to 247 mg kg-1 between samples collected at 1 and 35 m. The 1050 ppm S fuel exhibited the same, factor of two-to-three increasing trend. These results were supported by AMS observations of increasing organic and sulfate aerosol mass with plume age.

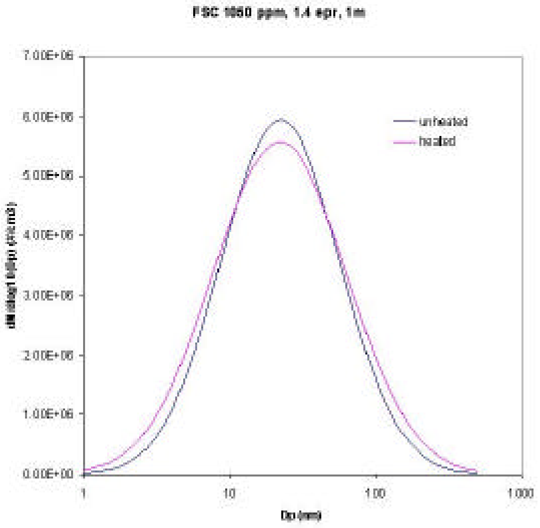

Figure 7. Heated (300^{o}C) and unheated (20^{o}C) B-757 aerosol size distributions recorded at 1 m as the engine burned 1050 ppm S fuel at 1.4 EPR.

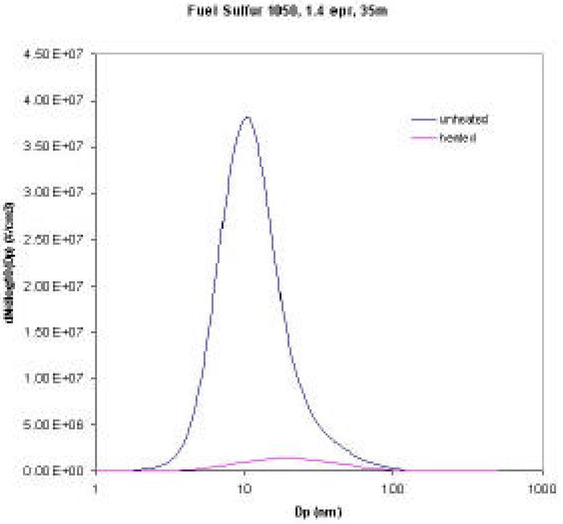

Figure 8. Heated (300^{o}C) and unheated (20^{o}C) B-757 aerosol size distributions recorded at 35 m as the engine burned 1050 ppm S fuel at 1.4 EPR.

3.4 Non refractory PM1.0 Composition (Aerodyne Aerosol Mass Spectroscopy Group)

Excluding sampling periods from shortly after engine starts and power changes when sometimes enormous quantities of organic aerosols were emitted, the RB-211 exhaust plume organic and sulfate mass loadings ranged from 1 - 45 µg m^{-3}, and 0.1 - 7 µg m^{-3}, respectively. Except for measurements made at idle (1.03 EPR), sulfate EIs appeared to be independent of engine power settings, and proportional to the fuel sulfur content. For measurements recorded at 35 m and fuel sulfur contents of 810 ppm, 1050 ppm and 1820 ppm, the average EI of sulfate equaled 0.0025, 0.003 and 0.007 g kg^{-1} of fuel g kg^{-1} of fuel, respectively. The anomalous EIs measured at idle could be due to quantification errors for sulfate due to interference from organics. For organics, the EIs increase with engine power, from 0.018 g kg^{-1} at idle to 0.04 g kg^{-1} of fuel at 1.5 EPR (Boudries et al., this issue, see references). The decrease in EIs as a function of engine power could be explained by better combustion efficiency at high engine power and consequently a reduction in the emissions of unburned fuel and oil. It is also important to note that the EIs of organics as a function of engine power were found to be independent of fuel sulfur content and that the individual organic aerosols exhibited mass signatures more similar to those of turbine engine oil than those of the JP-5 jet fuel.

The relative mass loading of organics and sulfates increased significantly with sampling distance. For instance, at engine power of 1.3 EPR, the organics concentrations increased from 5 to 25 µg m^{-3} and sulfate from 1 to 6 µg m^{-3} between samples collected at 10 and 35 m. This increase could be explained by condensation of gas-phase pollutants on pre-existing aerosols within the aging exhaust plume. Confirming this hypothesis, we found that both the organic and sulfate aerosol size distributions shift to larger sizes when sampled further downstream of the engine exhaust plane, indicating the condensational growth. We also observed distinctly different growth rates for these species, which suggests that they were externally mixed. For example, at 1 m sampling distance, the organics and sulfates exhibited mean aerodynamic diameters of ~30 nm whereas at 35 m, the organic modal diameter had increased to 300 nm and the sulfate to 70 nm. These observations are supported by DMA data that indicate the nucleation mode (30 –70 nm) mass and number concentration was de pendent upon fuel sulfur content.

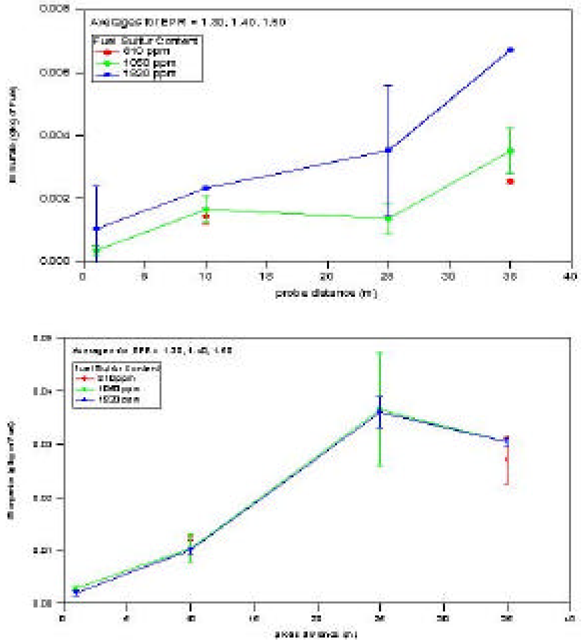

Figure 9. B-757 sulfate and organic aerosol emission indices as functions of sampling distance and fuel S content.

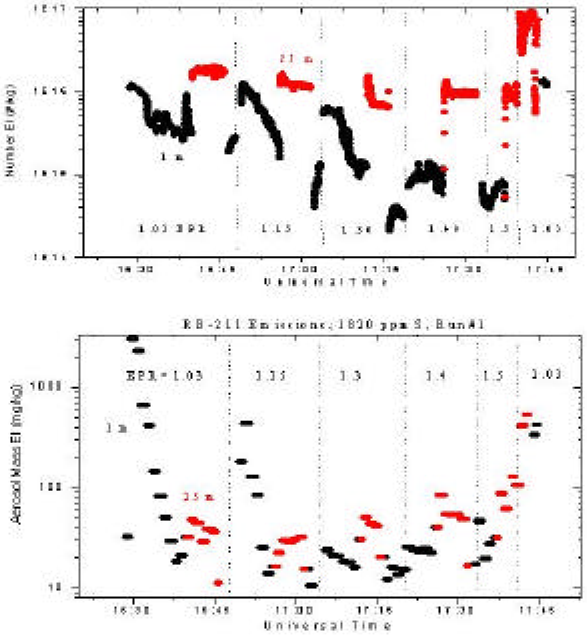

Figure 10. Time series of aerosol number EI (top) and mass EI (bottom) recorded during an engine run that included a cold start followed by a sequence of power changes.

Figure 9 shows the variation of EIs as a function of sampling probe distance measured for all sulfur fuel content. Here the EIs are found to be positively correlated with probe distance. The lowest EIs are measured at 1 m behind the engine and the highest EIs are measured at 35 m behind the engine. For all fuel used, the sulfate emission indices increase with distance suggesting aerosol sulfate growth through gas to particle conversion downstream of the exhaust plumes. This conversion is occurring as the exhaust cools down as a consequence of dilution with ambient air. For sulfate, the EIs are also found to be a function of sulfur fuel content. The lowest EIs are measured for the lowest fuel sulfur content and vice-versa. At 35 m behind the engine, the sulfate EIs increase by a factor of 2.89, while the fuel sulfur content increased by 2.14. Within the uncertainty of our measurement, we can conclude that the EIs are linearly proportional to fuel sulfur content.

3.5 Transient Emissions (Langley and Aerodyne Aerosol Groups)

Emission data acquired at idle and 1.15 EPR were highly variable and depended more on how long the engine had been running and the time since power change than upon the selected test variables of fuel S or plume age. For example, Figure 10 (top) shows a 1-second resolution time-series plot of the RB-211 Number EIS for 1820 ppm S fuel and samples extracted at 1 and 25 m downstream of the engine exhaust plane. The engine had cooled for ~1 hr prior to the beginning of the record. Note that 1 m values are ~10^{16} kg^{-1} at startup then drift downward by a factor of 5 over the 20 minute run at 1.03 EPR. When power is increased to 1.15 EPR, Number EIs jump back up to 10^{16} kg^{-1}, then begins to drift downward as the engine re-equilibrates to the new fuel flow rates and combustor temperatures, reaching ~10^{15} kg^{-1} just before the power is increased to 1.3 EPR Similar jumps in Number EIs occurred after each power change although the subsequent drift was less at the higher EPR settings. Equally dramatic changes were observed in mass emissions (Fig. 10, bottom). For example, at engine start, mass EIs peaked at ~3000 mg kg^{-1}, then decreased to < 100 mg kg^{-1} some 10 minutes later. Although a reduction in number concentrations contributed to this change, it was primarily driven by a shift in the modal diameter from ~100 nm to < 25 nm during this time period. The power increase from 1.03 to 1.15 EPR produced similar enhancements in mass emissions (and GMD) that required 3 to 4 minutes to settle back down to a steady state value(s). Order-of-magnitude transients also occurred when power was reduced from 1.5 EPR to idle. In terms of an explanation, simultaneous aerosol mass spectral data indicate the transient aerosols were composed of organic species that possessed mass signatures similar to those of engine oil. After cold starts and power changes in the low EPR range, it takes a few minutes for the compressor stages to reach thermal equilibrium and establish the very tight component tolerances necessary for optimum engine performance. We speculate that during this thermal adjustment period, a minor amount of engine oil leaks around the seals and produces the observed organic aerosol enhancements. It is significant to note that the enhancements were present in samples collected at 1 m where the exhaust gas temperatures were quite high; this supports the idea that they were composed of relatively non-volatile species such as those present in thermally stable turbine engine lubricating fluid. It is also possible that a fraction of these particles was derived from unburned fuel, as whole air samples collected within the plume shortly after engine start contained significant enhancements in relatively low-molecular weight hydrocarbon species. Unburned fuel is certainly present within the exhaust just before combustor ignition and may take a few minutes to volatilize and be cleared from the downstream sections of the engine.

REFERENCES

Whitefield, P.D., et al., "QinetiQ/NASA Collaborative Programme – Final Report," produced for UK Department of Trade and Industry Under Order/Contract reference F11X1DXX by QinetiQ Ltd, Cody Technology Park, Farnborough, Hampshire GU14 0LX, UK, 2002. Also available as NASA Contractor Report CR-2002-211900.

Anderson, B.E., et al., Airborne observations of aircraft aerosol emissions, 1, Total and non-volatile particle emission indices, *Geophys. Res. Lett., 25,* 1689-1692, 1998.

Anderson, B.E., et al., An assessment of aircraft as a source of particles to the upper troposphere, *Geophys. Res. Lett., 26,* 3069-3072, 1999.

Arnold, F., Detection of massive negative chemiions in the exhaust plume of a jet aircraft in flight, Geophys. Res. Lett., 26, 1577-1580, 1999.

Boudries, H., et al., Aerosol and Gas Chemistry of Commercial Aircraft Emissions Measurements in the NASA EXCAVATE Experiment. This issue.

Brock, C.A., et al., Ultrafine particle size distributions measured in aircraft exhaust plumes, *J. Geophys. Res., 105*, 26,555-26,567, 2000.

Miake-Lye, R., et al., SOx oxidation and volatile aerosol in aircraft exhaust plumes depend on fuel sulfur content, *Geophys. Res. Lett., 25*, 1677-1680, 1998.

Petzold, A., et al., In situ observations and model calculations of black carbon emission by aircraft at cruise altitude, *J. Geophys. Res., 104*, 22,171-22181, 1999.

Schumann, U., et al., Pollution from aircraft emissions in the North Atlantic flight corridor: Overview on the POLINAT projects, *J. Geophys. Res., 15*, 3605-3631, 2000.

Schumann, U. et al., Influence of fuel sulfur on the composition of aircraft exhaust plumes: The experiments SULFUR 1-7, *J. Geophys. Res., 107*, 10.1029/2001JD000813, 2002.

Thompson, A., et al., Introduction to special section: Subsonic Assessment Ozone and Nitrogen Oxide Experiment (SONEX) and Pollution from Aircraft Emissions in the North Atlantic Flight corridor (POLINAT 2), *J. Geophys. Res., 105*, 3595-3603, 2000.

Toon, O.B. and R.C. Miake-Lye, Subsonic Aircraft Contrail and Cloud Effects Special Study (SUCCESS), *Geophys. Res. Lett., 25*, 1109-112, 1998.

SAE E-31 Committee on Aircraft Exhaust Emission Measurements and an Aerospace Information Report on the Measurement of Non-volatile Particle Emissions

R.C. Miake-Lye*
Aerodyne Research, Inc., Billerica, Massachusetts, USA

V. Zaccardi
Jacobs/Sverdrup, Arnold Air Force Base, Tullahoma, Tennessee, USA

Keywords: particle emissions, SAE, Aerospace Information Report, CAEP

ABSTRACT: The SAE E-31 committee has specified measurement techniques and protocols for aviation emission measurements for many existing regulations and is currently focused on writing an Aerospace Information Report (AIR) on the measurement of non-volatile particle emissions. This AIR is an initial step in developing an Aerospace Recommended Practice (ARP) as have been previously written by E-31 for gaseous emissions (ARP1256) and smoke number (ARP1179). These two ARPs have been incorporated in regulation by the USEPA and ICAO (Annex 16) and are widely used and referenced by the engine measurement community. The motivation for preparing the present AIR on non-volatile particles and its scope and content are described.

1 INTRODUCTION

Agencies responsible for regulating and certifying aviation operations have begun to examine methods for measuring particle emissions from aircraft engines. There is general consensus that the regulations regarding the emission of visible smoke for aircraft engines, which have been in place for decades, do not address and are not relevant to the measurement of particles responsible for health effects and environmental impacts. Working Group 3 of the ICAO Committee on Aviation Environmental Protection (CAEP) has asked the SAE E-31 committee for technical assistance in developing appropriate particulate characterization techniques for routine certification of aircraft turbine engines. The SAE E-31 committee has specified measurement techniques and protocols for aviation emission measurements for many existing regulations and the committee has accepted these requests for the specification of small particle emissions measurement. It is the intent of the E-31 committee to make use of both committee expertise and outside technical advice to develop a set of recommendations that will form the basis for an Aerospace Information Report (AIR). This AIR will be subject to evaluation and review by the regulatory agencies, industry, and the engineering community that performs aviation emissions measurements.

2 E-31 HISTORICAL CONTEXT

SAE (Society of Automotive Engineers) International is an international technical organization serving the transportation industry, including automobiles, heavy duty vehicles, and aerospace. The E-31 Committee was chartered within the aerospace arm of SAE in 1968 “to establish standard methods and instrumentation for all types of exhaust emissions, other than normal atmospheric constituents, from aircraft engines ...”. The initial impetus for E-31 was to provide guidance on measuring pollutants from airplanes that were contributing to environmental problems in and around airports. The first activities were to develop Aerospace Recommended Practices (ARPs) for visible smoke (ARP1179, Aircraft Gas Turbine Engine Exhaust Smoke Measurement, 1970) and for

---

* *Corresponding author:* Miake-Lye, Richard C., Aerodyne Research, Inc., Billerica, Massachusetts, 01821-3976 USA. Email: rick@aerodyne.com

gaseous emissions (ARP1256, Procedure for the Continuous Sampling and Measurement of Gaseous Emissions from Aircraft Turbine Engines, 1971). These ARPs were adopted by regulatory agencies in the USA and internationally via ICAO to prescribe how engine emissions are quantified.

E-31 has updated these two measurement procedure documents over the years as the techniques have improved and been refined. An additional ARP (ARP1533, Procedure for the Calculation of Basic Emission Parameters for Aircraft Turbine Engines) on analyzing the data measured using ARP1256 was developed and released in 1986. In 1990 the E-31 charter was revised to both broaden the scope of measurement and focus the emphasis of its activities specifically to measurement only. The broadening of scope was several fold: to include on-wing engines and auxiliary power units, to explicitly task the committee to continually review and update the ARPs, and to acknowledge the function of the committee in exchanging information and generating discussion on advances in measurement technology. At the same time, it was made clear that E-31 should remain separate from the policy issues of setting emissions level goals or requirements, and that even strategies for minimizing or controlling emissions are outside the purview of the committee, per se. The 1990 charter revision included the following language: “to include aircraft power plants and combustion systems ….. review and maintain standards ……. provide a forum for discussions and the introduction of new ideas….. E-31 will not address engine emissions levels nor control strategies to meet air quality standards”.

As part of the broadening of scope, E-31 published ARP4418 in 1995 which addressed the measurement of emissions in cabin bleed air, which is the air obtained from the gas turbine’s compressor system and used to pressurize and ventilate the passenger cabin. More recently, the committee has begun to consider complete revision of the measurement procedures due to significant and on-going improvements in measurement technology. The first revisions will be directed at the emissions of particles, partly because the original requirement was to reduce visible smoke and that need has been largely superseded and partly because the environmental and human health issues associated with particles have become much better understood in the intervening years. It is this particle measurement issue that is the topic of the Aerospace Information Report currently being written and reviewed by E-31.

The E-31 committee is primarily composed of technical measurement specialists. A wide range of the aircraft turbine engine community is represented including engine manufacturers, direct users of installed engines (notably commercial airframe and military users), and governmental regulatory agencies and laboratories. The committee membership is international, with strong European involvement representing industry and government labs. The US is well represented both by industry and government, including regulatory agencies (EPA and FAA), NASA, and the Department of Defense. Due to cross memberships, good connections are established and maintained with ICAO Working Group 3 and with ASME Committee on Stationary Gas Turbine Engines. Table 1 summarizes the composition of the committee.

Table 1. E-31 Committee Composition

Composition in Category		US Government	
Engine Manufacturer	4	Air Force	4
Air Frame Manufacturer	1	Navy	1
Industry	3	Army	1
Academia	2	Depart. of Trans.	1
European	5	EPA	2
ICAO WG-3	Chair	FAA	2
ASME Stationary Eng.	Chair	NASA	2

3 AIR ON NON-VOLATILE PARTICLES

The E-31 Committee has had a long interest in particle emissions, starting with its first ARP on smoke. As new measurement technology has become available, E-31 has invited speakers to present work using advanced techniques. Both improved means of measuring visible obscuration and related techniques for measuring more detailed particle emission parameters have been reviewed by E-31. With this background and driven by requests from ICAO Working Group 3, the US FAA, and US EPA, a Particle Subcommittee was formed to address the need for a standard for measuring particles beyond the existing Smoke Number ARP.

Unlike in the late 1960's when regulations were being formulated and the measurement requirements were perhaps more clearly defined, the subcommittee is faced with suggesting best measurement practice in the absence of specific regulatory requirements. In order to move forward without having a concrete regulatory framework, the subcommittee chose to create a preliminary document to define the problem and outline an approach to addressing it. Thus, in April 2002, the subcommittee released a "Position Paper" which outlined E-31's view of the particle measurement issue and the steps needed to develop, eventually, an Aerospace Recommended Practice on particle measurement.

The Position Paper discusses particle emissions from aircraft engines and the present status of Smoke Number, as has been outlined above. Current controls on all emissions and ARP 1179 for Smoke Number is presented and contrasted with what is needed to understand human health effects and environmental consequences. The need for advanced techniques, such have been developed for a variety of emissions requirements, are discussed and contrasted for their application to aviation emissions in general terms. The point is also made, however, that advanced measurement techniques can be applied to measure specific particle emission parameters, but regulations must specify which parameters are to be measured. And, further, the regulations must be specific enough that the measurement requirements are unambiguous.

The status of particle environmental effects is in a state of rapid flux. The Position Paper acknowledges that both primary particles formed within the engine and condensable gases emitted from the engine can both contribute to the condensed phase particles eventually deposited in the environment. However, the measurement issue that will be addressed at this point will be the measurement of non-volatile particles at the exit plane of the engine. The chemical and surface properties of the emitted particles and the possibility of newly formed volatile particles condensing outside of the engine are specifically excluded from the present measurement technique identification. These latter issues are important and the subcommittee intends to address them in due course if driven by regulation.

Based on the particle emission issue defined in this way, the Position Paper established the intent of the E-31 Particle Subcommittee to write an Aerospace Information Report on the measurement of non-volatile particle emissions. This will allow the most promising techniques for application to aviation engines to be discussed and presented to engine measurement community. Based on the AIR, the measurement community and regulatory agencies can provide feedback on the appropriateness and relevance of the various techniques to the evolving regulatory and technological requirements. Based on this feed back, the AIR can be enhanced and refined to become a recommended practice and a measurement standard as an ARP.

The AIR is currently under review. It begins with a definition of its scope to be non-volatile particles. Then particle measurement techniques are reviewed, first for measuring particle mass, followed by measurement of particle number density and size distributions. For both measurement classes several techniques that have been successfully applied to aviation engine measurement are presented. Other measurement techniques that may be promising for this application are also briefly described. Finally, a discussion of probes is presented, since the probes can significantly affect the particles that are introduced into the measurement instrument. Both sampling losses and perturbations to the particles being sampled are important concerns in the design of sampling systems.

4 DEVELOPMENT OF A RECOMMENDED PRACTICE

The AIR is being written and reviewed as the committee's experts' and advisors' knowledge is assimilated and the report is expected to be completed in the current year. This AIR will be subject to evaluation and review by regulatory agencies, industry, and the engine measurement community. Based on the experience gained and on improvements in measurement practice, the AIR will then be used over the course of several years to develop a set of measurement specifications contained in an ARP on particle measurements. ARPs are the official statement of the SAE on how emissions measurements should be performed and, as such, have historically provided methodologies acceptable to the regulatory agencies both in the US and internationally. This ARP will then be available for use by regulatory agencies and engine measurement engineers as an authoritative reference point for reliable measurement of aviation particle emissions.

REFERENCES

SAE E-31, 1990: ARP1256, Procedure for the Continuous Sampling and Measurement of Gaseous Emissions from Aircraft Turbine Engines, Society of Automotive Engineers, Rev. B.

SAE E-31, 1997: ARP 1179, Aircraft gas turbine exhaust measurements, Society of Automotive Engineers, Rev. C.

SAE E-31, 2002: Position Paper on Particle Matter Measurements, Society of Automotive Engineers, 2002.

Particle Emissions from Aircraft Engines - An Overview of the European Project PartEmis

A. Petzold [*], M. Fiebig , L. Fritzsche, C. Stein , U. Schumann
DLR, Institute of Atmospheric Physics, Oberpfaffenhofen, Germany

C.W. Wilson , C.D. Hurley
QinetiQ, Farnborough, UK

F. Arnold , E. Katragkou
Max Planck Institute for Nuclear Physics, Heidelberg, Germany

U. Baltensperger, M. Gysel , S. Nyeki
Paul Scherrer Institute, Villigen, Switzerland

R. Hitzenberger, H. Giebl
University of Vienna, Vienna, Austria

K. J. Hughes
University of Leeds, Leeds, UK

R. Kurtenbach, P. Wiesen
University of Wuppertal, Wuppertal, Germany

P. Madden
Rolls Royce plc, UK

H. Puxbaum , S. Vrchoticky
Technical University of Vienna, Vienna, Austria

C. Wahl
DLR, Institute for Combustion Technology, Cologne, Germany

Keywords: particle emissions, combustion aerosol, PartEmis

ABSTRACT: An overview of the goals and achievements of the European PartEmis project (Measurement and prediction of emissions of aerosols and gaseous precursors from gas turbine engines) is presented. PartEmis is focussed on the characterisation and quantification of exhaust emissions from a gas turbine engine. The engine was composed of a combustor and a unit to simulate a 3-shaft turbine section (so-called Hot End Simulator; HES). A comprehensive suite of aerosol, gas and chemi-ion measurements were conducted under different, i) combustor and HES operating conditions, ii) fuel sulphur concentrations. Measured aerosol properties were mass and number concentration, size distribution, mixing state, thermal stability of internally mixed particles, hygroscopicity, cloud condensation nuclei (CCN) activation potential, and chemical composition. Furthermore, chemi-ions, non-methane volatile organic compounds (NMVOCs) and OH were monitored. The combustor operation conditions corresponded to modern and older engine gas path temperatures at cruise altitude, with fuel sulphur contents (FSC) of 50, 410, and 1270 g kg^{-1}. The combustor behaves like a typical aircraft engine combustor with respect to thermodynamic data and main emissions, which suggests that the PartEmis database may be applicable to contemporary aircraft engines.

---

[*] *Corresponding author:* Andreas Petzold, DLR Institute of Atmospheric Physics, Oberpfaffenhofen, 82234 Wessling, Germany. Email: andreas.petzold@dlr.de

1 INTRODUCTION

The role of aviation-related particle emissions in the upper troposphere and lowermost stratosphere is a matter of concern, particularly with respect to a possible effect on the composition of upper tropospheric aerosol and the life cycle of cirrus clouds (Boucher, 1999; Schumann and Ström, 2001). Despite recent considerable progress in the characterisation of the aerosol particles emitted from jet engines (e.g., Anderson et al., 1998; Brock et al., 2000; Hagen et al., 2001; Petzold and Schröder, 1998; Petzold et al., 1999; Schumann et al., 2002), microphysical and chemical properties as well as the influence of engine operating conditions still remain poorly characterised with respect to particulate emissions. However, this kind of data set forms a basic pre-requisite for modelling approaches which investigate the role of aviation aerosols and their effect on the environment.

In the framework of the European project PartEmis ("Measurement and prediction of emissions of aerosols and gaseous precursors from gas turbine engines"), the influence of operation conditions and fuel sulphur content (FSC) on the microphysical and chemical properties of particles emitted from a jet engine simulator was investigated. For these purposes, an engine simulator which met the ICAO (International Civil Aviation Organisation) engine emissions smoke standard was operated on a test rig at the QinetiQ test site at Pyestock, UK. This engine simulator consisted of a real jet engine combustor and a so-called Hot End Simulator (HES) which simulates the pressure and temperature profiles found in a jet engine turbine section. In a first experiment, the emission properties of the combustor were studied. These data were then used as boundary conditions for a second experiment which focused on the emission properties of the combustor-HES combination. The aerosol microphysical and chemical properties investigated in this study covered number, size, and mass concentration of primary combustion aerosol particles which form in the combustion process and secondary volatile particles which form outside the combustor in the cooling plume. Furthermore, the volatile fraction of internally mixed combustion particles, particle hygroscopicity, and cloud condensation nuclei (CCN) activation potential were studied. In addition, the emission of chemi-ions, non-methane volatile organic compounds (NMVOCs) and OH was monitored. A detailed description of the PartEmis experiments is given by Wilson et al. (2003).

2 METHODS

A tubo-annular, transpiration cooled combustor was chosen for tests on QinetiQ's High Pressure Combustion Rig. Air was delivered from a four-stage compressor and heater unit. A back-pressurising valve located downstream of the combustor maintained the correct pressure in the system. The standard test-rig instrumentation covered 41 control parameters, such as temperature, pressure, fuel and air flow rates, as well as CO, CO_2, total hydrocarbons (HC), NO_X, and smoke number. Two engine operating conditions were simulated to represent the thermodynamic conditions found in the turbine stages of legacy referred to here as "old" and modern aircraft cruise conditions at 35,000 feet (~ 11,700 m). This will ensure that the conversion of fuel sulphur to oxidised sulphur species is replicated. These old and modern combustor operating conditions were also chosen to meet the ICAO smoke emission level. Fuel sulphur content (FSC) levels covered the range from low sulphur fuel (50 $\mu g\ g^{-1}$) to the contemporary average (410 $\mu g\ g^{-1}$) and to a maximum of about three times this average (1270 $\mu g\ g^{-1}$) defined here as Low, Mid and High (L, M, H) FSC, respectively. The sulphur content was varied by adding known quantities of benzenethiol (C_6H_5SH) to the low FSC fuel. The operation conditions are summarised in Table 1.

The employed aerosol measurement methods consisted of various size-selective methods, aerosol absorption photometers, thermodenuder methods, a Cloud Condensation Nucleus Counter (Hitzenberger et al., 2003), an extensive set of chemical analytical methods (Petzold et al., 2003), mass spectrometry methods for the detection of sulphur-containing species, and laser-induced fluorescence for OH measurements. A summary of deployed methods is given in Table 2.

The black carbon (BC) mass concentration and the aerosol absorption coefficient in the diluted sample gas were measured using a Particle Soot Absorption Photometer (PSAP; Radiance Research Inc, Seattle, USA). The specific absorption cross section at $\lambda = 0.55\ \mu m$, $\sigma_{abs} = 6.7\ m^2\ g^{-1}$ was used for conversion of light absorption to BC mass. The number concentrations were measured in the size intervals D = 4 - 7 nm, 7 - 9 nm, 9 - 20 nm, and 20 - 250 nm with parallel-operated

Condensation Particle Counters (Condensation Particle Size Analyser, CPSA) which were set to different lower instrument cut-off diameters. Particles of size $D > 9$ nm which are detected in CPSA channels 3 and 4, are in the following referred to as N_{10}. Particle size distributions were measured with a commercial Scanning Mobility Particle Sizer (SMPS; TSI Model 3071) and a Volatility-Tandem Differential Mobility Analyser (V-TDMA) in the size range $D > 13$ nm.

Table 1. Combustor operating conditions during the 2001 Combustor and 2002 HES campaigns.

Combustor Parameters	Combustor Campaign		HES Campaign	
	Old	Modern	Old	Modern
T combustor inlet, K	566	766	566	760
T combustor outlet, K	1125	1448	1125	1360
P combustor inlet, 10^5 Pa	7.05	8.2	7.05	8.2
Air mass flow, kg s^{-1}	2.12	2.12	1.90	2.05
Fuel flow, kg s^{-1}	0.032	0.042	0.030	0.035
Air fuel ratio	66	50.3	66	58

The aerosol mixing state and the volatile fraction of the combustion aerosol were determined using thermal denuder methods which differentiate particles according to their thermal stability. Setting the thermal denuder temperatures to 390 K and 573-625 K, respectively, distinguishes volatile (vaporises at 390 K) sulphuric-acid like material from semivolatile (vaporises between 390 and 573 K), and refractory black-carbon like material. The thermal treatment of almost monodisperse particle size fractions which were pre-selected by a DMA provides information whether the aerosol is internally or externally mixed. The ratio of diameters after and before thermal treatment yields the particle shrinkage factor D^3 / D_0^3 . This factor describes the particle volume reduction by the thermal treatment, i.e., the volatile volume fraction of internally mixed particles is $1 - D^3 / D_0^3$.

The hygroscopic particle growth factor under subsaturated conditions was measured with a Hygroscopicity Tandem DMA . The obtained growth factor describes the particle growth by water uptake from the gas phase at a selected relative humidity. This growth factor indicates the presence of a coating of particles by a hygroscopic substance as, e.g., sulphuric acid. The fraction of particles which become activated as cloud condensation nuclei (CCN) were measured at a super-saturation of 0.7% with respect to liquid water using a Cloud Condensation Nuclei Counter (Giebl et al., 2002). This property becomes important as soon as a possible effect of aircraft engine emissions on atmospheric clouds is studied.

Aerosol samples were collected with filter stack samplers and low pressure Berner impactors for total aerosol and size-resolved chemical mass analysis. The chemical composition of the carbonaceous fraction of the exhaust particles was determined using multi-step combustion methods. Total carbon (TC) was determined by a combustion technique involving combustion in a vertical furnace and detection of CO_2 with a commercial NDIR (non dispersive Infrared spectrometer) unit. Aliquots of a collected filter sample were burnt in the ceramic tube of a combustion furnace with an excess of oxygen at a temperature of 1000 °C. Elemental carbon (EC) was determined by the “Cachier” method, i.e., another aliquot of the filter sample was treated for 2h at 320°C in an oxygen atmosphere to remove organic carbon compounds and then analysed with the same TC analysis method. The remaining carbon was attributed to elemental carbon (EC). Thermograms of the collected carbonaceous material were measured with a thermo-optical evolved gas analysis method (Schmid et al., 2001). To determine anions, e.g., SO_4^{2-}, as well as cations, two Dionex isocratic systems with electrochemical suppression were used.

In addition, the aerosol was sampled on quartz tubes containing glass wool. The aerosol loaded quartz tubes were analysed by 5 min thermodesorption in a Helium atmosphere at 130°C and 350°C, respectively. The desorbed $C_2 – C_{12}$ non-methane hydrocarbons (NMHC) were analysed with a gas chromatograph (Hewlett Packard). NMHCs were monitored using a compact GC instrument (Airmovoc 2010) with an enrichment system (cryotrap) and FID detector. C_2-C_{10} aliphatic and aromatic NMHCs were measured with a time resolution of 10 min and with detection limits in the pptv range. Selected partially oxidised hydrocarbons (OHCs) such as aldehydes and organic acids were collected by using special sampling cartridges and measured off-line using HPLC with a photo-array detector. The OHCs were measured with a time resolution of 4 min and with detection limits in the ppbv range.

Gaseous sulphuric acid was measured using a CIMS (Chemical Ionisation Mass Spectrometer) apparatus equipped with an Ion Trap Mass Spectrometer (ITMS). The ITMS allows CID (Collision-Induced-Dissociation) investigations of mass selected ions to be performed which in turn allows much better species identification than can be offered by a conventional mass spectrometer. In order to avoid sampling line losses a relatively short sampling line (150 cm) without dilution and with a temperature exceeding 150°C was used.

OH laser induced fluorescence (LIF) measurements were performed in the exhaust duct of the HES. The experiment comprised a Nd/YAG pumped dye laser set up to generate light at λ = 281.913nm in order to excite the $Q_1(1)$ transition of OH $A^2\Sigma(\nu'=1) \leftarrow X^2\Pi(\nu''=0)$, chosen as it is one of the strongest transitions at the temperature expected at the observation point. Fluorescence was detected perpendicular to the path of the laser from the $\nu'=0 \rightarrow \nu''=0$ transition around 309 nm via a lens and a customised interference filter. In order to maximise the signal to noise ratio by discriminating against Raman scatter expected from N_2 and H_2O, an interference filter was centred at 308.75 nm with a band pass of 4.96 nm (FWHM). A gated CCD camera cooled to -30°C was used to collect the signal, allowing signal accumulation over long times in order to enhance sensitivity.

Table 2. Available equipment and parameters.

Parameter	Technique
Volatile condensation particles (number, size)	Condensation Particle Size Analyser (CPSA), Differential Mobility Analyser (DMA) connected to a Thermodenuder
Non-volatile carbonaceous particles (number, size)	Condensation Particle Counter (CPC), Scanning Mobility Particle Sizer (SMPS), DMA connected to a Thermodenuder Volatility Tandem-DMA
Surface density	Diffusion Charger
Aerosol absorption coefficient b_{abs},	Aerosol Absorption Photometer
Smoke Number SN	Smoke number method
Water uptake at RH ≤ 100%	Hygroscopicity Tandem-DMA
Cloud condensation nuclei activation	Thermal gradient CCN counter
Chemical composition	Berner low pressure impactor (BLPI) samples; filter stack samples; analysis via gravimetry (total mass), multi-step combustion method (organic/elemental carbon), evolved gas analysis (volatility of carbonaceous compounds) gas chromatography (aliphatic, constituents), ion chromatography (major ions)
CO, CO_2, HC, NO_x, O_2, H_2	Standard test rig instrumentation
HONO, HNO_3;	Chemical ionisation mass spectrometry
SO_2, SO_3, H_2SO_4;	Paul Ion Trap Mass Spectrometry (PITMAS)
Chemi-ions	
SO_2	
Gaseous hydrocarbon species	Quasi-on-line gas chromatography (GC); Sampling and off-line analysis
Partially oxidised hydrocarbons	DNPH method
OH	Laser-induced fluorescence (LIF)

Since the full set of applied instruments was connected to separate sampling lines according to specific instrument requirements, the precise determination of the dilution factors was a crucial task. After exit from the traversing probe, the sample was cooled to ~ 150°C using a water-jacket, and delivered to the undiluted and diluted sample lines. The undiluted line was insulated along its entire length in order to avoid wall losses of combustion products, while sample in the diluted line naturally attained room temperature (~ 25°C) after dilution. Dilution with filtered air was necessary for the majority of instruments to reduce concentrations to a measurable level. The sample dilution factor was determined from CO_2 mixing ratios measured in the supplied dilution air, diluted sample, and undiluted sample, as well as from temperature and pressure sensors throughout the sample delivery system. Although stable gaseous species such as CO_2 and water vapour are unaffected by intrusive sampling, aerosols may be lost due to diffusion and sedimentation to the surfaces of the sampling system.

3 RESULTS

3.1 *Microphysical Properties*

The aerosol emitted from the Combustor is composed of primary particles forming inside the combustor and of volatile condensation particles nucleating in the cooling exhaust gas from gaseous precursors. The aerosol size distribution in the diluted exhaust gas of the combustor is shown in Fig. 1 for conditions with and without condensation particle formation. While the mode of combustion aerosol particles dominates the size range D > 15 nm with a maximum at 40 nm, another mode of nanoparticles is present in all cases in the size range D = 7 – 20 nm. Condensation particle formation, is occurring only at high FSC conditions and contributes to the size range D = 4 –7 nm.

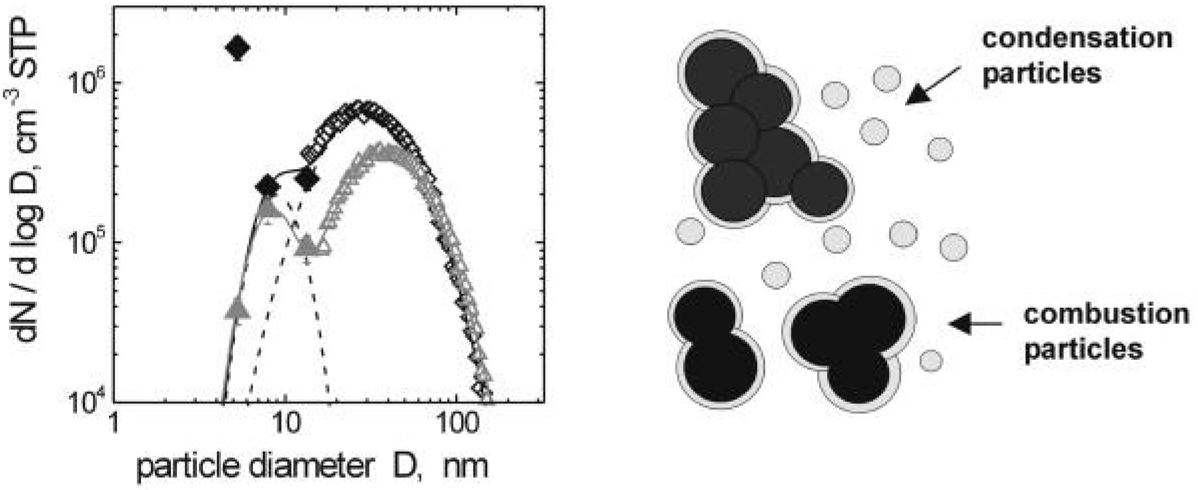

Figure 1. Left: size distribution of combustion aerosol with (◆) and without condensation particle formation (7). Right: External aerosol mixture composed of volatile condensation particles (.) and coated nonvolatile combustion particles (,).

The emission properties with respect to the primary aerosol are shown in terms of BC mass (EI_{BC}), TC mass (EI_{TC}), and number (EI_{N10}), emissions per kg of consumed fuel in Fig. 2. The number emission index EI_{N10} refers to particles with diameters D ≥ 10 nm. In Fig. 2, also the count median diameter (CMD) of the exhaust aerosol size distribution is shown. Plotted are corresponding values for the combustor emissions and emissions from the HES low pressure stage. In the first place, it has to be mentioned that all the results are consistent. At old cruise conditions, an increasing number emission at constant black carbon mass emission is balanced by a decreasing particle size. It should be noted that these results originate from different measurement techniques.

When operated at old engine conditions with low combustor inlet temperature T_C, EI_{BC} varies from 0.051 to 0.081 g kg^{-1}. Operated at modern engine conditions with the higher inlet temperature, EI_{BC} ranges from 0.028 to 0.044 g kg^{-1} which is a factor of 2 lower. Similar relations hold for the other properties. However, the amount of emitted particulate matter is within the range permitted by the ICAO rules in all cases. Mean CMD values are 37 – 41 nm for old engine and 40 – 44 nm for modern engine conditions. The geometric standard deviation of the size distribution is 1.67 (1.6 – 1.8) for both operation conditions (Petzold et al., 2003). The combustor operating conditions were found to have a weak influence on the size, number and mass of emitted particles. The influence of the different HES pressure stages is demonstrated in Fig. 3. Except for a step-like increase from the combustor experiments to the HES experiments which is most likely due to slightly different operating conditions, the HES has no influence on the emission properties of the Combustor-HES combination with respect to combustion aerosol particles. Increasing the FSC slightly increased the total number of emitted particles. Particles smaller than 10 nm contribute less than 10% of the total exhaust aerosol in the low and medium FSC cases. At high FSC levels the formation of volatile condensation particles with diameters $D < 10$ nm was observed. Particles of size $D \geq 30$ nm were almost entirely internally mixed. Smaller particles ($D < 20$ nm) exhibited volume fractions of 10-15% and semivolatile 4-10% for volatile and semi-volatile material, while the volatile fraction decreased to < 5% for $D \geq 50$ nm particles (Petzold et al., 2003).

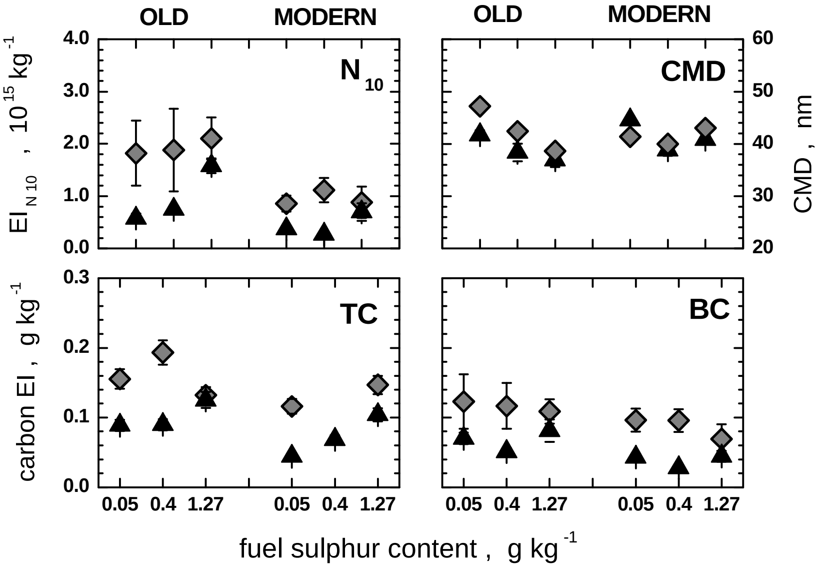

Figure 2. Emission indices in terms of number (N_{10}), total carbon mass (TC), black carbon mass (BC) and count median diameter (CMD) of the combustion aerosol for the Combustor exit (7) and the Hot End Simulator low pressure stage (Λ); values are given for old and modern operation conditions as a function of the fuel sulphur content.

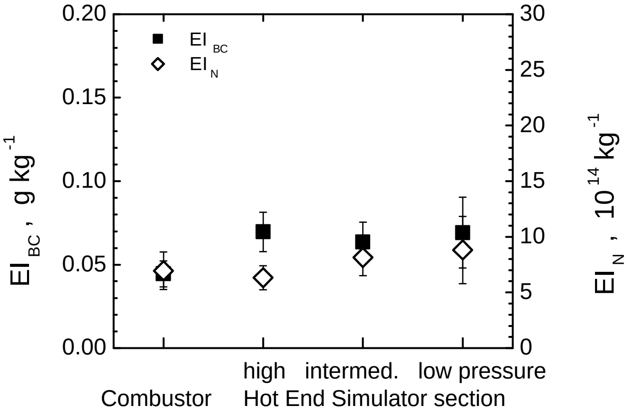

Figure 3. Effect of the Hot End Simulator on the emission properties of the Combustor-HES combination operated at modern conditions.

3.2 *Chemical Properties*

Primary particles emitted from the combustor are predominantly composed of carbonaceous material (> 95%) and of water-soluble inorganic components. The carbonaceous material is composed of organic compounds and of elemental or black carbon. The organic compounds may be volatile or semi-volatile, i.e., they oxidise at temperatures as low as 400 K. Fig. 4 shows the thermal stability of an exhaust aerosol sampled during operation with low FSC fuel at modern conditions. From an aerosol loaded glass wool sample more than 180 different NMHCs were desorbed under an Helium atmosphere. Only 0.4 wt% of the NMHCs were desorbed at $T \leq 400$ K, whereas 99.6 wt% were desorbed at T = 400-620 K. This is in good agreement with the result of the thermogram in Fig. 4. Elemental (EC) or black carbon (BC), respectively, is chemically almost inert at low and moderate temperatures and thermally stable up to temperatures of about 700 K.

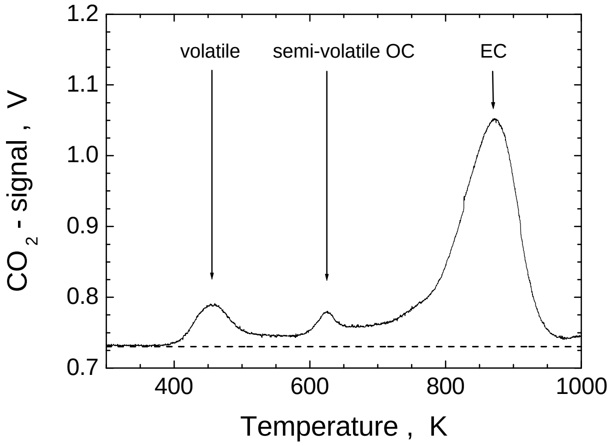

Figure 4: Evolving CO_2 as a function of the sample heating temperature for a Combustor aerosol sample; volatile OC oxidises at 450 K, semi-volatile OC at 600 K, and elemental carbon above 700 K.

During combustion, the sulphur contained in the fuel is oxidised to SO_2 which is then partially converted to S(VI) in the hot exhaust gas. The efficiency of conversion from S(IV) to S(VI) is described by the conversion efficiency ε calculated as $\varepsilon = S(VI)/S_T$ where S_T is the total fuel sulphur. In the combustor campaign the S(VI) increased with increasing FSC. The efficiency of conversion in the combustor campaign ranged between 0.9±0.5 % and 1.3±0.7 %. In the HES campaign S(VI) increased with increasing FSC, fuel flow, and from the high-pressure to the low-pressure HES stage. For FSC=1270 ppm the conversion efficiency was 2.3±1.2 % at the low pressure stage for the modern cruise condition and 1.4±0.7 % for the old cruise. The higher ε observed for the modern cruise conditions suggests that modern engines have a larger e compared to old ones.

Chemical composition information was obtained from Berner low pressure impactor samples which were taken at a sample line temperature of 150°C. At these conditions most of the sulphuric acid will remain in the gas phase, while only a small fraction is more strongly bound to or chemisorbed at the particle surface and will be observed in particulate matter samples. The chemical analysis results indicate, that the mass distribution of the carbonaceous matter matches the volume distribution of the aerosol, while the mass distribution of chemisorbed sulphate follows the surface distribution of the aerosol. This observation indicates that the sulphate is chemisorbed at the particle surface. The chemisorbed fraction of sulphuric acid corresponds to a coverage of max. 0.1 monolayer in the high FSC case. This fraction of converted S(VI) corresponds to less than 0.1% of total S(IV), present in the fuel. More than 90% of the S(VI) remains in the gas phase at a gas temperature of about 150°C. The overall partitioning of sulphur-containing species is: 97% SO_2 , $\leq$ 2.7% gaseous H_2SO_4, < 0.3% chemisorbed.

3.3 *Particle hygroscopic properties*

Particle hygroscopic properties were measured at ambient conditions using a Hygroscopicity Tandem Differential Mobility Analyser (H-TDMA) system (Gysel et al., 2003). The instrument measures the hygroscopic growth factor (g) of particles with initial dry sizes D_o = 30, 50 and 100 nm over the range RH ~ 70 – 95% where g(RH) = D(RH)/D_o. Growth factors were found to increase with increasing FSC at fixed particle size (e.g. D_o = 50 nm; g(95%) = 1.01 and 1.16 for FSC = low and high, respectively), and to decreased with increasing particle size at fixed FSC (e.g. mid FSC; g(95%) = 1.14, 1.10 and 1.03 for D_o = 30, 50 and 100 nm, respectively). The results suggest an increasing amount of sulphuric acid adsorbed on combustion particles from the gas phase with increasing FSC.

Cloud condensation nuclei (CCN) were measured in the diluted line using a static thermal diffusion type CCN counter (Giebl et al., 2002). Particles are exposed to controlled supersaturations of water vapour, which enables some of the particles to become activated and grow to large (> 10 µm) droplets. During PartEmis, the supersaturation was set to ~ 0.7 %. The fraction of CCN in the aerosol (relative to the concentration of particles > 10nm) increased with increasing FSC, but even for low FSC the fraction of CCN (at 0.755 % supersaturation) was higher than the fraction of particles with diameters larger than 0.280 µm, i.e. the size at which wettable insoluble particles are activated according to the Kelvin effect. At high FSC, the fraction of CCN increased by about a factor 5.5 for old and 12 for modern conditions but was still lower by a factor ~ 15 for those particles with D > 0.03 µm, i.e. the dry size of sulphuric acid particles which are activated according to Köhler theory. Further details are given by Hitzenberger et al. (2003).

3.4 *Gaseous Hydrocarbon Emission*

More than 100 different non-methane volatile organic compounds (NMVOCs), such as non-methane hydrocarbons (NMHCs) and selected partially oxidised hydrocarbons (OHCs) emitted from the jet engine combustor and the hot end simulator (HES) were identified and quantified. These species accounted for up to 91 wt % of the total hydrocarbons (THCs). The NMHC emission indices of 5 - 15 mg kg^{-1} in total are comparable with the AEROTRACE study. Both studies show up to 1000 times lower emission indices in comparison with emissions from vehicular traffic. The influence of the operation conditions on NMHC emissions of the combustor and HES was investigated for the identified NMHCs. From the six conditions which were investigated (2 operation conditions, 3 HES pressure stages), most compounds showed a decrease of NMHC emissions with increasing combustion temperature at the same pressure stage. This is in agreement with results from the combustor exit measurements and with the results of the AEROTRACE study. Emission indices at HES pressure stages high (HP)-, intermediate (IP)- and low pressure (LP) for fixed FSC and combustor operation conditions were also investigated. Most compounds showed a decrease of NMHC emissions with decreasing pressure in the HES at similar combustor operation conditions and fixed FSC. The decrease of the pressure in the HES corresponds to an increase of the residence time in a turbine and indicates a decrease of NMHC emissions along the different turbine sections.

3.5 *Emission of ions and charged soot particles*

The ions measured during the HES campaign are product ions formed from primary ions via ion molecule reactions involving either few reaction-steps with massive neutral molecules or numerous reaction-steps with relatively small neutral molecules. Their lifetimes with respect to ion-ion recombination are around 9 ms after the high pressure turbine section. The ion emission index E_i is up to 4.5×10^{16} ions per kg fuel burnt. It seems that ion-induced nucleation can explain at least partly the observed volatile aerosols. Electrically charged small positive and negative soot particles (CSP) have also been detected during both PartEmis campaigns. Charged soot particles were found to have diameters around 6 nm and a total concentration of up to 4.5×10^7 cm^{-3} (positive and negative) corresponding to a total emission index of $E_{CSP} = 2.3\times10^{15}$ CSP per kg fuel burnt.

3.6 *OH measurements*

At high laser energies, observed OH fluorescence was dominated by a photolytic source of OH. At low laser energies, OH in the exhaust duct was successfully detected, although there was still a component present from photolysis. Calibration experiments provide a method to assign the observed OH LIF signals an absolute concentration, and from an estimate or measurement of the errors for each parameter, an overall estimate of the error in the assigned OH concentration was made. From these calibration experiments very low values of less than 1 ppbv were calculated for the OH concentration in the exhaust gas after exiting the HES. Previous experiments using a combined Raman scattering/LIF technique to look in the exhaust gases 50 cm behind a jet engine exit failed to detect any OH LIF signal, and therefore could only infer an upper limit for OH of 80 ppbv based on the measured detection limit of their apparatus.

4 SUMMARY AND CONCLUSIONS

4.1 *Combustion aerosol*

- The combustor behaves like a typical aircraft engine combustor with respect to thermodynamic data and main emissions. It may thus be expected that the PartEmis database can be applied as a first order approximation to contemporary aircraft engines.
- The BC concentration is nearly independent of FSC level.
- The number size distribution of primary particles in the diameter range $10 < D < 550$ nm is almost uninfluenced by the FSC level or combustor conditions. But at high FSC levels the formation of volatile condensation particles with diameters $D < 10$ nm was observed.
- The average density of the combustion aerosol is 0.95 – 1.0 g of total carbon cm^{-3}, referring to a sphere of equivalent diameter; the specific surface area is 80 – 100 m^2 (g total carbon)$^{-1}$.
- The volatile volume fraction of particles > 50 nm increases from 2 % for low FSC to approx. 5% for high FSC. The volatile volume fraction of particles < 30 nm is ≤ 15%.
- Volatility measurements indicate an internally mixed aerosol for particles with $D > 15$ nm; condensation particles are < 15 nm.

4.2 *Ultrafine particles*

- Formation of condensation particles in the Combustor tests for high FSC at old and modern conditions; “formation strength” ≤ 7 condensation particles / combustion particle;
- Formation of condensation particles in the HES tests for high FSC/modern conditions/low pressure section only; “formation strength” ≤ 14 condensation particles / combustion particle;
- Ultrafine carbonaceous particles of size 7 nm < D < 20 nm are observed independently of the fuel sulphur content; a volatility analysis indicates that these particles are nonvolatile and may be composed of carbonaceous compounds.

4.3 *Sulphate-containing species, chemi-ions and OH*

- S(VI) was measured in the form of sulphuric acid. Increased FSC resulted in higher S(VI) concentrations. The measured conversion efficiency for fuel sulphur to S(IV) at the combustor exit varied from 0.35 - 1.4% and was independent of the investigated combustor operation conditions and FSC levels.
- 10 - 30% of sulphate is chemisorbed on primary particles; the coverage of primary particles is below 0.1 monolayers of sulphuric acid.
- Sulphur partitioning: 97% SO_2 , ≤ 2.7% gaseous H_2SO_4, < 0.3% chemisorbed.
- Positive and negative gaseous ions were detected for the first time in the exhaust of a combustor, with mass numbers up to 1500. The total ion emission index at the HES hp stage was as high as 5.4×10^{17} positive and negative ions per kg fuel burnt. Large ions with mass numbers exceeding 4500 were contributed about 10% to the total ion number concentration.
- OH concentration in the exhaust gas after exiting the HES is < 1 ppbv.

4.4 *Hygroscopic growth and CCN activation*

- Small differences in particle hygroscopicity are observed between old and modern cruise conditions.
- Strong effect of the fuel sulphur content is observed, particle hygroscopicity increases distinctly with increasing FSC.
- No significant effect of the HES at low and mid FSC level is observed; higher particle hygroscopicity downstream the HES are observed at high FSC compared to the combustor exit.
- CCN activation of combustion particles increases with increasing FSC as a result of larger particle hygroscopicity; additional effects of adsorbed organic matter cannot be excluded.

- CCN activation is about twice as efficient for modern as for old cruise conditions.

4.5 *Gaseous organic fraction:*

- More than 100 different NMVOCs (aliphatic and aromatic hydrocarbons, carbonyls and acids) were identified and quantified, they accounted for 91 wt % of the total detected compounds.
- A decrease in NMHC emissions from old to modern conditions at fixed HES pressure stage and fuel sulphur content (FSC) was found.
- A decrease of NMHC emissions with decreasing pressure in the HES at fixed combustor operation conditions and FSC was observed.
- No clear influence on the NMHC emissions with changing FSC at the same combustor operation condition was observed.
- High EI's for organic acids are found. Perhaps organic compounds fixed at the sampling line walls are oxidised by the hot exhaust gases. Or the acids are fixed at the surface of the soot particles, which are also trapped in the sampling cartridges.

4.6 *Emission properties*

- Emission properties regarding combustion aerosol mass, number and size are determined by the combustor; the influence of the Hot End Simulator is weak.
- The processing of exhaust gas and particles during the transfer through the Hot End Simulator increases the particle hygroscopicity and formation strength of condensation particles; both effects are related to gaseous sulphuric acid.

The experimental overview of the EU PartEmis project presents the first comprehensive aerosol and gas measurements to be conducted on a jet engine combustor test-rig. Specific aspects of these measurements are presented elsewhere (Gysel et al.; Hitzenberger et al.; Petzold et al.; 2003). The database will be used for further analyses as well as for plume modelling by other PartEmis groups.

5 ACKNOWLEDGEMENT

The PartEmis project was funded by the European Commission under contract no. G4RD-CT-2000-00207. The authors are very grateful to the test rig operation crew at QinetiQ for their very strong support during the experiments.

REFERENCES

Anderson, B.E., et al., 1998: Airborne observations of aircraft aerosol emissions, I, Total nonvolatile particle emission indices, *Geophys. Res. Lett., 25*, 1689-1692.

Boucher O. , 1999: Influence of air traffic on cirrus occurrence, *Nature*, 397, 30-31.

Brock, C.A., et al. , 2000: Ultrafine particle size distributions measured in aircraft exhaust plumes, *J. Geophys. Res.*, *105*, 26555-26567.

Giebl, H., A. Berner, G. Reischl, H. Puxbaum, A. Kasper-Giebl, and R. Hitzenberger, 2002: CCN activation of oxalic and malonic acid test aerosols with the University of Vienna cloud condensation nuclei counter. *J. Aerosol Sci. 33*, 1623-1634.

Gysel, M., S.Nyeki, E. Weingartner, U. Baltensperger, H. Giebl, R. Hitzenberger, A. Petzold, and C.W. Wilson, 2003: Properties of jet engine combustor particles during the PartEmis experiment. Hygroscopicity at subsaturated conditions, *Geophys. Res. Lett.*, *30***,** 1566, doi:10.1029/2003GL016896.

Hagen, D.E., P.D. Whitefield, J.D. Paladino, and O. Schmid, 2001: Comparative study of jet engine combustion emissions and engine operating conditions, in Schumann, U. and Amanatidis G. (Eds.), *Aviation, aerosols, contrails and cirrus clouds*, Air pollution research report 74, pp 106-110, European Commission, Brussels.

Hitzenberger, R., H. Giebl, A. Petzold, M. Gysel, S. Nyeki, E. Weingartner, U. Baltensperger, C.W. Wilson, 2003: Properties of jet engine combustor particles during the PartEmis experiment. Hygroscopic properties at supersaturated conditions, *Geophys. Res. Lett.*, *30***,** 1779, doi:10.1029/2003GL017294.

Petzold, A., and F.P. Schröder, 1998: Jet engine exhaust aerosol characterization, *Aerosol Sci. Technol., 28*, 62-76.

Petzold, A., A. Döpelheuer, C.A. Brock, and F.P. Schröder, 1999: In situ observations and model calculations of black carbon emission by aircraft at cruise altitude, *J. Geophys. Res.*, *104*, 22171-22181.

Petzold, A., C. Stein, S. Nyeki, M. Gysel, E. Weingartner, U. Baltensperger, H. Giebl, R. Hitzenberger, A. Döpelheuer, S. Vrchoticky, H. Puxbaum, M. Johnson, C.D. Hurley, R. Marsh, and C.W. Wilson, 2003: Properties of jet engine combustor particles during the PartEmis experiment. Microphysical and chemical properties. *Geophys. Res. Lett.*, 30**,** 1719, doi:10.1029/2003GL017283.

Schmid, H., et al. , 2001: Results of the "carbon conference" international aerosol carbon round robin test stage I, *Atmos. Environ.*, *35*, 2111–2121.

Schumann, U., et al. , 2002: Influence of fuels sulphur on the composition of aircraft exhaust plumes: The experiments SULFUR 1-7, *J. Geophys. Res.*, *107* (10.1029/2001JD000813), AAC 2-1 – AAC 2-27.

Schumann, U. and Ström, J. , 2001: Aviation impact on atmospheric composition and climate, in *European research in the stratosphere 1996 – 2000*, European Commission, EUR 19867, Brussels.

Wilson, C.W., et al. , 2003: Measurement and Prediction of Emissions of Aerosols and Gaseous Precursors from Gas Turbine Engines (PartEmis): An Overview, *Aerosp. Sci. Technol.*, in press.

Emission of Non-Methane Volatile Organic Compounds (NMVOCs) from a Jet Engine Combustor and a Hot End Simulator (HES) During the PartEmis Project

R. Kurtenbach*, J. C. Lörzer, A. Niedojadlo, M. Petrea, P. Wiesen
University of Wuppertal, Wuppertal, Germany

M. Kapernaum, C. Wahl
DLR, Institute for Combustion Technology, Stuttgart, Germany

Keywords: NMVOC emissions, combustion NMVOC, PartEmis

ABSTRACT: During the PartEmis measurement campaigns at QinetiQ, Pyestock in January 2001 and in March 2002 the emissions of non-methane volatile organic compounds (NMVOCs) from a jet engine combustor and a hot end simulator (HES) were measured. In addition, CO_2 measurements were also performed for determining emission indices (EIs).The C_2-C_{10} aliphatic and aromatic hydrocarbons were monitored using a compact online gas chromatograph (GC) (Airmovoc 2010) with enrichment system and FID detector. The non-methane hydrocarbons (NMHCs) were measured with a time resolution of 10 min and detection limits in the pptV range. Selected partially oxidised hydrocarbons (OHC) such as aldehydes were collected by using special sampling cartridges and measured off-line using HPLC with a photo-array detector. The OHCs were measured with a time resolution of 4 min and detection limits in the ppbV range. A fully automated online GC system (Chromato-sud) with TCD detector was used to monitor CO_2. Measurement cycle and detection limit of this system were 5 min and 10 ppmV, respectively. More than 100 different NMVOCs were identified and quantified and accounted for up to 91 wt % of the total NMVOCs emitted. Sample line effects on the measured data were investigated and were found to be statistically not significant. Generally, the NMVOC emission indices for the combustor and HES measurements from this study and the data from previous studies showed a high variability within two orders of magnitude. In addition, the present studies on aircraft emissions show up to 1000 times lower NMVOC emission indices in comparable with the emissions from vehicular traffic. During the PartEmis campaigns the influence of combustor power, pressure in the different stage of the HES and different fuel sulphur content (FSC) on the emission of the species studied was also investigated. No clear impact of the FSC on the NMHC emissions was observed. A decrease in NMHC emissions with increasing combustor power was found and are comparable with the data from the AEROTRACE (1996) study and the study by Spicer et al. (1994). A decrease of NMHC emissions along the different turbine sections (HES) was observed indicating that chemistry is on-going in the turbine.

1 INTRODUCTION

Although only a few percent of the fossil fuel is currently being burnt by air traffic (Brasseur et al., 1998), most of the combustion emission are being deposited in the very sensible altitude regions of the atmosphere; i.e. the upper troposphere and lower stratosphere, where the compounds may have long life times and where background concentration are usually low. Since only a very limited number of engines have been investigated under realistic flight conditions up to now (Fahey et al., 1995a; 1995b, Schumann, 1997, Slemr et al., 1998, Schumann et al., 2002). Ozone around the tropopause originates partly from the stratosphere and is partly produced photochemically from NMVOC and NO_x as precursors (Ehhalt et al., 1992). The NO_x emission from air traffic is supposed to have caused increased ozone concentrations around the tropopause (Penner et al., 1999). The

---

* *Corresponding author:* Ralf Kurtenbach, University of Wuppertal, Wuppertal, 42110 Wuppertal, Germany. Email: kurtenba@uni-wuppertal.de

impact of the NMVOC emission from air traffic is generally considered to be small (Haymann and Markiewircz, 1996). However, these studies are based on a few measurements of individual NMVOCs (Spicer et al., 1994, Slemr et al., 1998). In addition, in-flight studies and modelling (Kärcher et al., 1998, Schumann et al., 2002) have shown the potential importance of unburnt, NMVOCs on the formation of condensation particles in the exhaust of an aircraft engine. One objective of the extensive measurement programme within the PartEmis was to perform measurements for individual NMVOCs from a serious of combustor and hot end simulator (HES) tests. Detailed information on the PartEmis experiments is given by Petzold et al. (2003).

2 METHODS

The C_2-C_{10} aliphatic and aromatic non-methane hydrocarbons (NMHCs) were monitored using a compact online gas chromatograph (GC) (Airmovoc 2010) with enrichment system (cryotrap) and FID detector. The system has been described in more detail elsewhere (Gomes and Benter, 2003).

The smallest combustor operation interval for some test point during the campaigns was about 10 min. However, the measurement procedure for the C_2-C_{10} aliphatic and aromatic NMHCs only allowed a time resolution of at least 20 min. Therefore, two similar GCs were operated with a time shift of about 10 min, which enabled the measurement at each test point. The GC instruments including the sampling system were calibrated with a certified standard mixture from the UK National Physical Laboratory (NPL-UK) containing 30 different C_2-C_9 NMHCs in nitrogen. The GC system reached an accuracy of 10-20% for aliphatic and 15% for aromatic NMHCs and a precision of 15%-20% for aliphatic and 10% for aromatic NMHCs. The detection limits for all NMHCs were in the pptV range.

Selected partially oxidised hydrocarbons (OHCs) such as aldehydes and ketones were collected by using special sampling cartridges coated with 2,4-dinitrophenylhydrazine. The 2,4-dinitrophenylhydrazine forms with the reactive carbonyls a stable hydrazone compound. The hydrazones were eluted out of the cartridge with acetonitrile and separated in a high performance liquid chromatograph (HPLC) with diode array detector (DAD). The compounds were identified via retention time and absorption spectra. The OHCs were measured with a time resolution of 4 min and detection limits in the ppbV range.

A fully automated online GC system with TCD detector (Chromato-sud) was used to monitor CO_2. Measurement cycle and detection limit of this system were 5 min and 10 ppmV, respectively. The sample time and sample volume were 0.1 min and 1 ml, respectively. The system has been described in more detail elsewhere (Becker et al., 1999). In order to increase the sampling time, offline measurements were also performed. The exhaust gas was sampled into 4 litre stainless steel canisters. Sample flow and sample time were 600 ml/min and 9–14 min, respectively. After sampling, the stainless steel canisters were analysed with the online GC-TCD system. Calibration of the GC-TCD system including the sampling system was performed using certified CO_2 gas mixtures (Messer-Griesheim). The GC-TCD system had an accuracy of 5% and a precision of 2%.

The undiluted exhaust gases were transferred from the combustor and HES to the GC sampling system through a heated sampling line system set up by QinetiQ. The sampling system used during the PartEmis campaigns is schematically shown in Fig. 1.

Sampling line losses in the undiluted line without and with exhaust were investigated for the NMHCs. The certified NMHC gas mixture from the NPL-UK was added to the sampling line system at the inlet air valve with a flow rate of 2 *l*/min (see Fig. 1) and the difference between calculated (exhaust gas value + gas mixture value = calculated value) and measured concentration values at the end of the sampling line was determined. For OHC’s no sampling line effects were investigated, because no stable gaseous mixtures of the OHCs were available.

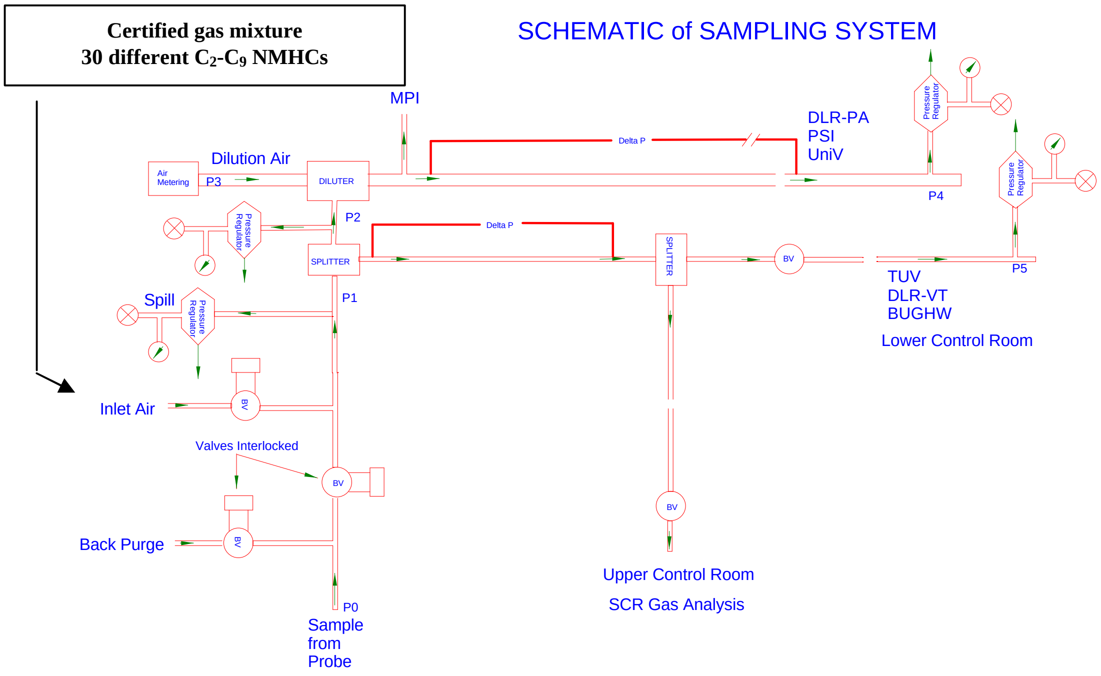

Figure 1:Schematic diagram of the sampling line system at QinetiQ.

3 RESULTS

More than 100 different non-methane volatile organic compounds (NMVOCs), such as non-methane hydrocarbons (NMHCs) and selected partially oxidised hydrocarbons (OHCs) emitted from the jet engine combustor and the hot end simulator (HES) were identified and quantified. These species accounted for up to 91 wt % of the total NMVOCs, which were measured using a total NMVOC analyser from QinetiQ.

3.1 *Sampling line effects*

Fig. 2 shows the results of the calibration gas measurements with and without sampling line system from QinetiQ. The results of the measurements without using the sampling system are normalized to 100%. With the exception of iso/1-butene (+ 563 %), the difference between expected and measured value for the NMHCs are in the range of 5 ± 10 % and in comparison with the accuracy of the GC system and, there for, statistically not significant. In addition, the measurements with exhaust gas show the same results.

3.2 *NMVOC emission indices of the combustor for cruise power condition*

For the calculation of the NMVOC emission indices (EIs) (mg/ kg fuel burnt) the measured CO_2 data with identical sample intervals were used. Table 1 shows the calculated min, max, and median value of the NMVOC EIs for cruise power conditions of the PartEmis study in comparison with other studies. Table 1 shows, that from the measured compounds in the PartEmis project, only a limited number can be compared with the other studies. From the PartEmis study only ethylene/ethane, ethane, benzene, m-p-xylene, methylglyoxal and hexanal show emission indices >1 mg/kg fuel burnt, all other compounds show much lower emission indices. In comparison with the other studies only ethane, propene, propane, iso-butane, cis-2-butene, benzene, m-/p-xylene, o-xylene, acetaldehyde and methylglyoxal are in the same measurement range. Generally, the NMVOC emission indices for the combustor and HES measurements from this study and the data from previous studies showed a high variability within the range of 0–82 mg/kg fuel burnt. In addition, the present studies on aircraft emissions show up to 1000 times lower emission indices in comparison with emissions from vehicular traffic (Gomes and Benter, 2003).

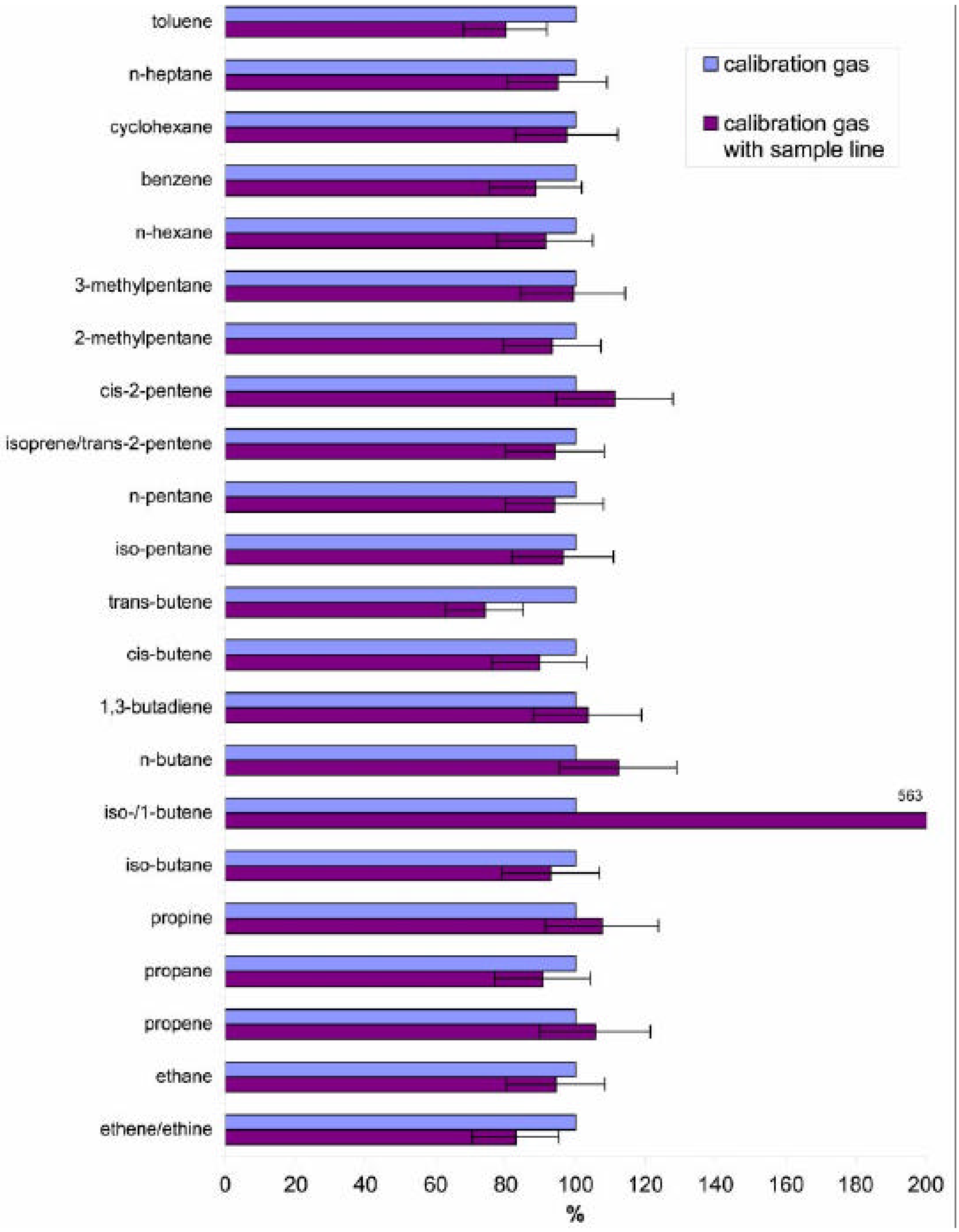

Figure 2. Comparison of the NMHC measurements with and without using the sampling line system of QinetiQ. The results without using the sampling line system are normalised to 100%.

From the median emission values, listed in table 1 the percent distribution of the NMVOCs classes, aromatic NMHCs, aliphatic NMHCs and OHCs were calculated and are shown in Fig. 3. A median contribution of 12% aromatic NMHCs, 47% aliphatic NMHCs and 41% OHCs was found. Among the class of aromatic NMHCs, benzene (0.38 mg/kg), among aliphatic NMHCs, ethane (2.22 mg/kg) and among OHCs, hexanal (1.89 mg/kg) showed the largest emission index. In addition, a total NMVOC EI of 10.4 mg/ kg fuel burnt was calculated.

Table 1. Calculated NMVOC emission indices (mg/ kg fuel burnt) of the PartEmis study for cruise power condition in comparison with other studies.

Compound	**PARTEMIS Study**	**AEROTRACE 1996**	**Slemr et al. 1998**	**Spicer et al. 1994**
	Range (Median)	Range (Median)	Range (Median)	Range (Median)
ethyne, ethene	0.02 – 8.79 (0.63)	-	38.3 – 130.9 (93.8)	173.5
ethane	0.70 – 4.13 (2.22)	-	-	1.46 – 2.23 (1.85)
propene	0.01 – 0.62 (0.19)	0.03 – 0.96 (0.34)	4.22 – 21.3 (11.1)	0.34 – 17.5 (8.91)
propane	0.01 – 0.34 (0.09)	0.81 – 3.90 (2.33)	-	0.36 – 0.44 (0.40)
propyne	0.00 – 0.44 (0.32)	-	0.37 – 1.99 (1.27)	-
iso-butane	0.00 - 0.24 (0.02)	0.18 – 3.00 (1.67)	-	-
1-butene, iso-butene	0.22 – 0.47 (0.28)	9.10 – 17.2 (11.8)	1.66 – 10.6 (3.91)	-
1,3-butadiene, n-butane	0.10 – 0.55 (0.35)	6.20 – 6.80 (6.60)	0.66 – 3.51 (2.30)	11.63
trans-2-butene	0.00 – 0.18 (0.06)	-	-	-
cis-2-butene	0.02 – 0.46 (0.09)	-	-	0.34 – 2.08 (1.21)
iso-pentane	0.00 – 0.63 (0.08)	-	-	-
acetone	0.00 – 0.27 (0.07)	-	-	7.51 – 11.5 (9.50)
n-pentane	0.01 – 0.04 (0.02)	-	-	-
isoprene, trans-2-pentene	0.00 – 0.05 (0.02)	-	0.34 – 1.78 (0.90)	-
cis-2-pentene	0.00 – 0.08 (0.02)	-	0.15 – 0.55 (0.16)	-
2,3-dimethylbutane	0.00 – 0.12 (0.04)	-	-	-
cyclopentane,2-methylpentane	0.04 – 0.43 (0.18)	-	-	-
3-methylpentane	0.00 – 0.56 (0.08)	-	-	-
n-hexane	0.00 – 0.03 (0.01)	-	-	-
benzene	0.29 – 1.70 (0.38)	0.27 – 5.10 (1.78)	3.39 – 12.0 (9.60)	0.63 – 18.9 (9.78)
cyclohexane	0.00 – 0.06 (0.04)	-	-	-
iso-octane	0.00 – 0.04 (0.00)	-	-	-
n-heptane	0.01 – 0.92 (0.04)	-	-	-
2,3,4-trimethylpentane	0.01 – 0.10 (0.06)	-	-	-
2-, 3-methylheptane	0.01 – 0.23 (0.06)	-	-	-
toluene	0.02 – 0.21 (0.12)	0.34 – 1.20 (0.58)	0.70 – 2.98 (2.20)	0.32 – 4.27 (2.30)
ethylbenzene	0.09 – 0.21 (0.16)	-	-	0.79
m-, p-xylene	0.01 – 1.68 (0.17)	0.02 – 1.60 (0.31)	-	3.15
o-xylene	0.03 – 0.56 (0.26)	0.02 – 0.43 (0.07)	-	1.18
mesitylene	0.06 – 0.67 (0.18)	-	-	-
formaldehyde	0.16 – 0.61 (0.42)	0.88 – 1.45 (0.97)	-	56.1 – 106.9 (81.5)
acetaldehyde	0.10 – 0.56 (0.17)	0.54 – 1.35 (0.93)	-	1.60 – 33.3 (17.5)
propanal	0.00 – 0.35 (0.04)	-	-	0.46 – 6.77 (3.62)
butanal	0.00 (0.00)	-	-	1.06 – 6.76 (3.91)
acrolein	0.01 – 0.76 (0.60)	1.11 – 5.14 (2.28)	-	19.41
methacrolein	0.00 – 0.85 (0.40)	-	-	-
glyoxal	0.20 – 0.80 (0.34)	-	-	2.89
methylglyoxal	0.07 – 2.12 (0.24)	0.50 - 1.18 (0.98)	-	-
benzaldehyde	0.00 – 0.60 (0.13)	-	-	3.15
hexanal	1.19 – 2.85 (1.89)	-	-	-

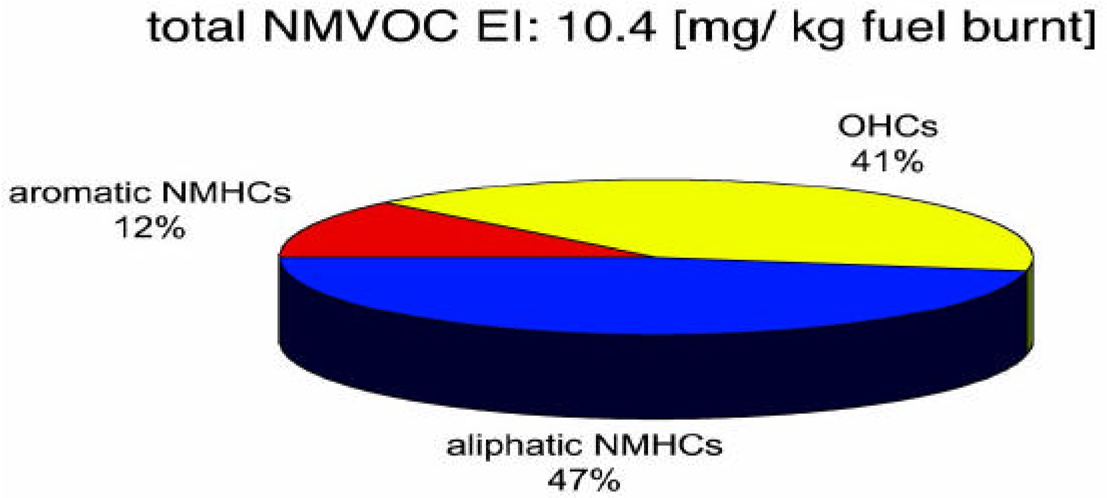

Figure 3. Median distribution of the NMVOC classes (mg/kg fuel burnt).

3.3 *Influence of the fuel sulphur content (FSC), on the NMHC emission of the combustor.*

From the measured emission indices emission ratios X; $X = EI_{\text{low FSC}} / EI_{\text{high FSC}}$ for each NMHC at different combustor power settings (old and modern cruise) were calculated. 54 ± 20 % of the NMHCs showed an emission ratio $X > 1$ on average. No clear impact of the FSC variation on the NMHC emission was observed.

3.4 *Influence of power setting, old – and modern cruise on NMHC emission of the combustor and HES.*

From the emission indices at different engine power settings, old cruise and modern cruise at fixed FSC and pressure stage an emission ratio X; $X = EI_{\text{old cruise}} / EI_{\text{modern cruise}}$ for each NMHC was calculated. Most NMHCs showed an emission ratio of $X > 1$ on average. This indicates a decrease of NMHC emissions with increasing combustor power. This is in agreement with results of the previous European AEROTRACE study (1996) and the study by Spicer et al. (1994).

3.5 *Influence of the pressure stage, high (HP)-, intermedium (IP)- and low pressure (LP) on the NMHC emission in the HES.*

In addition, from the emission indices at different pressure stage; high (HP)-, intermedium (IP)- and low pressure (LP) at fixed FSC and combustor power an emission ratio X; $X = EI_{HP} / EI_{IP}$ and $X = EI_{IP} / EI_{LP}$ for each NMHC were calculated. Most NMHCs showed an emission ratio of $X > 1$. This indicates a decrease of NMHC emissions with decreasing pressure in the HES. The decrease of the pressure in the HES is comparable which the increase of the resident time in a turbine and indicates a decrease of NMHC emission along the different turbine sections, which shows that chemistry is on-going in the turbine.

4 SUMMARY AND CONCLUSIONS

- More than 100 different NMVOCs (aliphatic and aromatic hydrocarbons and carbonyls) were identified and quantified: these species accounted for up to 91 wt % of the total NMVOC emission.
- Sampling line effects on the measured data were investigated for the NMHCs and were found to be statistically not significant.
- Generally, the NMVOC emission indices for the combustor and HES measurements from this study and the data from previous studies showed a high variability within the range of 0–82 mg/kg fuel burnt.

- The PartEmis and the previous studies on aircraft emissions show up to 1000 times lower NMVOC emission indices in comparable with the emissions from vehicular traffic.
- No clear impact of the FSC on the NMHC emissions was observed.
- A decrease in NMHC emissions with increasing combustor power was found and this result is comparable with the data from AEROTRACE study (1996) and the study by Spicer et al. (1994).
- A decrease of NMHC emissions along the different turbine sections (HES) was observed indicating that chemistry is on-going in the turbine.

REFERENCES

Becker, K. H., J. C. Lörzer, R. Kurtenbach, P. Wiesen, T. Jensen and T. J. Wallington, 1999: Nitrous oxide (N_2O) emissions from vehicles. *Environ. Sci. and Technol.*, 33, 4134-4139.

Brasseur, G. P., R. A. Cox, D. Hauglustaine, I. Isaksen, J. Lelieveld, D. H. Lister, R. Sausen, U. Schumann, A. Wahner and P. Wiesen, 1998: European scientific assessment on the atmospheric effects of aircraft emissions. *Atmos. Environ.*, 32, No. 13, 2329-2418.

Ehhalt, D. H., F. Rohrer and A. Wahner, 1992: Sources and distribution of NOx in the upper troposphere at northern mid-latitudes. *J. Geophys. Res.*, 97, 3725-3738.

Fahey, D. W., E. R. Keim, K. A. Boering, C. A. Brock, J. C. Wilson, H. H. Jonsson, S. Anthony, T. F. Hanisco, P. O. Wennberg, R. C. Miake-Lye, R. J. Salawitch, N. Louisnard, E. L. Woodbridge, R. S. Gao, S. G. Donnelly, R. C. Wamsley, L. A. Del Negro, S. Solomon, B. C. Daube, S. C. Wofsy, C. R. Webster, R. D. May, K. K. Kelly, M. Loewenstein, J. R. Podolske and K. R. Chan, 1995a: Emission measurements of the Concorde supersonic aircraft in the lower stratosphere, *Science*, 270, 70-74.

Fahey, D. W., E. R. Keim, E. L. Woodbridge, R. S. Gao, K. A. Boering, B. C. Daube, S. C. Wofsy, R. P. Lohmann, E. J. Hintsa, A. E. Dessler, C. R. Webster, R. D. May, C. A. Brock, J. C. Wilson, R. C. Miake-Lye, C. A. Brown, J. M. Rodriguez, M. Loewenstein, M. H. Proffitt, R. M., Stimpfle, S. W. Bowen and K. R. Chan, 1995b: In situ observations in aircraft exhaust plumes in the lower stratosphere at mid-latitudes. *J. Geophys. Res.*, 100, 3065-3074.

Gomes, A. and Th. Benter, 2003: Impact of road traffic emissions on the ozone formation in Germany. *Report no. 61, University of Wuppertal, Germany, ISSN 1436-2198.*

Hayman, G.D. and M. Markiewicz, 1996: Chemical modeling of the aircraft exhaust plume, in "Pollutions from Aircraft Emissions in the North Atlantic Flight Corridor (POLINAT)", U. Schumann ed, *Air Pollution Research Report 58 (EUR 16978 EN), European Comission.*

Kärcher, B., F. Yu, F. P. Schröder and R. P. Turco, 1998: Ultrafine aerosol particles in aircraft plumes: Analysis of growth mechanisms. *Geophys. Res. Lett.*, 25, 2793-2796.

Penner, J., D. H. Lister, D. J. Griggs, D. J. Dokken and M. McFarland (eds.), 1999: Aviation and the global atmosphere: a special report of IPCC working groups I and III, Cambridge University Press, *ISBN 0-521-66404-79.*

Petzold, A., M. Fiebig, L. Fritzsche., C. Stein, U. Schumann, C. W. Wilson, C. D. Hurley, F. Arnold, E. Katragkou, U. Baltensperger, M. Gysel, S. Nyeki, R. Hitzenberger, H. Giehl, K. J. Hughes, R. Kurtenbach, P. Wiesen, P. Madden, H. Puxbaum, S. Vrchoticky and C. Wahl, 2003: Particle emissions from aircraft engines – An overview of the European project PartEmis, this issue.

Slemr, F., H. Giehl, J. Slemr, R. Busen, P. Schulte and P. Haschberger, 1998: In-flight measurement of aircraft non-methane hydrocarbon emission indices. *Geophys. Res. Lett.*, 25, no 3, 321-324.

Spicer, C. W., M. W. Holdren, R. M. Riggin and T. F. Lyon, 1994: Chemical composition and photochemical reactivity of exhaust from aircraft turbine engines. *Annales Geophysicae*, 12, 944-955.

Schumann, U., 1997: The impact of nitrogen oxides emissions from aircraft upon the atmosphere at flight altitudes – Results from AERONOX project., *Atmos. Environ.*, 31, No. 12, 1723-1733.

Schumann, U., F. Arnold, R. Busen, J. Curtius, B. Kärcher, A. Kiendler, A. Petzold, H. Schlager, F. P. Schröder and K. H. Wohlfrom, 2002: Influence of fuel sulphur on the composition of aircraft exhaust plumes: The experiments SULFUR 1-7, *J. Geophys. Res.*, *107* (10.1029/2001JD000813), AAC 2-1 – AAC 2-27.

Modeling of Soot Precursor Formation in Laminar Premixed Flames with C1-, C2- and C6-Fuels

E. Goos[*], M. Braun-Unkhoff, N. Slavinskaya, P. Frank
Institut für Verbrennungstechnik, Deutsches Zentrum für Luft- und Raumfahrt (DLR), Stuttgart, Germany

Keywords: Fuel break-up kinetics, Polyaromatic hydrocarbons, Soot precursor, Soot volume fraction

ABSTRACT: In the present study models for formation and growth of polycyclic aromatic hydrocarbons (PAH) which are the base of particle formation by coagulation of the PAHs leading to soot, are compared with experimental species profiles in laminar premixed flames running with different fuels. The detailed modeling of the concentration profiles of these soot precursors was carried out by comparing two comprehensive gas phase reaction models. The experimental flame data stem from literature values for the fuels methane, ethene and benzene. Additionally, for recent experimental results from the investigation of sooting laminar ethene and propene flames, soot volume fraction profiles have been simulated by using a soot model, which combines a gas phase mechanism and a model for particle inception, coagulation, surface growth and oxidation. The aim of the present investigations is to establish a comprehensive PAH model for soot precursor kinetics which can be reduced in a sufficient manner to allow implementation into a CFD-code for modeling soot formation and oxidation in turbulent combustion processes.

1 INTRODUCTION

Aromatics and polycyclic aromatic hydrocarbons (PAH) are of particular concern in combustion processes because of their potentially adverse health effects. They are formed in the combustion of hydrocarbon fuels (e.g. kerosene) and have been identified as key precursors of soot. A soot model which is able to consider the fuel specifity for the prediction of the dynamics of particle formation and oxidation during the combustion process has to rely on a comprehensive gas phase fuel break-up and PAH formation reaction mechanism. Former investigations of flame and shock tube experiments, especially at high pressures, have shown the importance of PAH growth submodels on soot particle inception and on calculated soot volume fractions (Frenklach and Wang (1994), Böhm et al. (2003)). As in nearly all current soot models particle inception is described exclusively by coagulation of different large mass PAH, the influence of different PAH on the onset and the amount of soot has to be investigated systematically. Modeling studies (Hu et al. (2000)) reveal that only a few PAH species have to be considered for the simulation of the inception regime. A still open question is whether for different fuels the same major pathways of PAH formation and growth are found during combustion or whether the route to particle inception is not predictable with the same comprehensive gas phase reaction model. Therefore the investigation of PAH routes in laboratory flames is regarded as a tool for getting more insight into this problem.

However, for high pressure conditions, due to the very thin reaction zone, it is not possible to measure PAH profiles within and close to the very thin reaction zone. Therefore, PAH profiles measured in recent experiments with laminar premixed flames at atmospheric pressure have been used as data base for simulation. In these slightly sooting flames of aliphatic (methane, ethane, (Melton et al. (1998), Harris et al. (1998)) and aromatic hydrocarbons (benzene (Tregrossi et al. (1999)), a large variety of PAH (besides aliphatic compounds) has been measured by gas chromatography in combination with mass spectrometry ranging from two- to five-fused aromatic rings.

---

[*] *Corresponding author:* Elke Goos, Deutsches Zentrum für Luft- und Raumfahrt (DLR), Pfaffenwaldring 38-40, 70569 Stuttgart, Germany. Email: Elke.Goos@dlr.de

For comparing calculations, a recent comprehensive gas phase mechanism from literature (Appel et al. (2000)) and a gas phase mechanism established by the authors were used. The DLR mechanism which has been used with two modifications contains detailed chemistry for PAH growth including combinative growth steps of aromatic species and reactions to form species with up to 30 carbon atoms. Measured and predicted PAH profiles were compared to identify main routes for PAH growth. The different reaction pathways for the formation of PAH, the dominant species for soot precursor formation, were examined numerically to obtain a deeper understanding of the soot inception process.

2 GAS PHASE AND SOOT MODEL

At present, detailed modeling of soot formation and destruction is executed by using different, relatively large gas phase reaction mechanisms coupled with a mechanistic soot model that will be described later.

2.1 *Gas phase reaction mechanisms*

To describe the growth of polyaromatic species, the reaction mechanism given by Wang and Frenklach (1997) which comprises the reactions of aromatic species up to pyrene was updated with reactions of combinative growth steps of aromatic species as proposed by Böhm and Jander (1999) as well as reactions to form species with up to 30 carbon atoms (Richter et al. (1999)). Also, results of shock tube experiments for reactions of cyclopentadiene (Roy et al. (1998)) and the propargyl radical (Scherer et al. (2000)) and investigations focusing on the mono-aromatic species were taken into account: like decomposition of toluene and phenyl (Braun-Unkhoff et al. (1988)), benzyl (Braun-Unkhoff et al. (1990)) and phenylacetylene (Herzler et al. (1992)), and oxidation of phenyl (Frank et al. (1994)). In particular, the branching ratio of reactions with aromatic species turned out to be of importance with respect to formation of soot precursors. For example, the recombination of propargyl radicals leads essentially to the formation of benzene and not to phenyl and H-atoms; furthermore, propargyl radicals can react with benzyl, which is produced by pyrolysis of benzene, leading to indene.

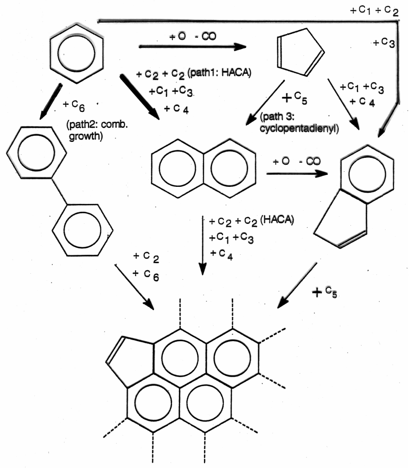

Figure 1: Principal reaction scheme for initial PAH formation

Figure 1 depicts the principal starting routes of the PAH growth submodel which contains about 45 species and 350 elementary reaction steps. Dominant routes are for example the hydrogen-abstraction-carbon-addition (HACA) path 1, the combinative growth path 2 which leads to the formation of biphenyl by the reaction of benzene and phenyl, and the cyclopentadienyl recombination (path 3) both producing naphthalene, and additional routes to form indene which then can grow by further reactions with cyclopentadienyl. The experimental data base for the rate constants in the PAH mechanism is extremely poor, and most of the data have to be estimated from the comparison with similar reactions of smaller aromatics. Additionally, the thermodynamic data of the polyaromatic species is important for calculating the reverse rate constant, but often the needed thermodynamic data is not available or calculated with big errors.

The complete updated mechanism with a total of more than 600 reactions and 170 species was used to describe in detail the evolution of the gaseous species up to the entry of the particle inception model. Most of the gas phase reactions are treated as reversible with rate coefficients for the reverse reactions evaluated from the respective equilibrium constant. Only a few reaction steps, representing preferentially isomerization reactions, are considered with separate rate coefficient expressions for forward and reverse direction. The DLR new# mechanism contains the same PAH growth submodel as the DLR old# mechanism. In the new# version, the detailed C1- C3 chemistry is replaced through the fitted rate coefficients from the GRI-mechanism (GRI 3.0 (1998)).

For comparison, a recently published reaction mechanism from Appel et al. (2000) was used which has been applied and validated under a variety of experimental conditions. This model comprises a relatively small PAH growth mechanism with 45 species, up to pyrene ($C_{16}H_{10}$), and about 190 elementary reactions.

2.2 *Soot model*

After calculating the concentration profiles with different reaction mechanisms, the same soot model is used for calculating PAH growth, particle inception, coagulation of particles, condensation, surface growth and soot particle oxidation. It is based on a model from Frenklach and Wang (1994) using the method of moments for solving the differential equation system. The particle inception is described by PAH coagulation. All large PAHs species (starting with $C_{16}H_{10}$) which are formed in the PAH growth model were assumed to collide giving rise to nucleus. Consequently, the sum of all calculated concentration profiles of species with 16 carbon atoms or more were used as inputs to the actual soot model. In addition to the original program, the pressure dependence of the coagulation of soot particles has been implemented into Smoluchowsky‘s equation (Hu et al. (2000)). Further growth of the particles results from surface mass growth with PAHs and other aliphatic gas phase species e.g. C_2H_2 and H_2. An essential quantity for the surface mass growth is the steric parameter α, which accounts for the fraction of surface sites available for corresponding reactions and which is a function of temperature and particle age, respectively. In the soot model used for this study, gas phase chemistry and soot dynamics are decoupled. Thus the conservation equations of soot on the gas phase are not taken into account. Neglecting these effects can lead to a slight overprediction of soot under the given conditions.

3 RESULTS

For comparison with the calculated data, experimental literature values from premixed flames with fuels like methane (Melton et al. (1998)), ethene (Harris et al. (1988)) and benzene (Tregrossi et al. (1999)) were used. The calculation of the concentration versus height profiles has been executed with the 1-dimensional PREMIX-code of the CHEMKIN-package (Kee et al. (1985)). As an example for the prediction of the combined gas phase and soot model, recent soot volume fraction profiles measured by Geigle et al. (2002) in ethene and propene flames were used.

3.1 *Aliphatic hydrocarbons*

The comparison between model calculation and experimental data in Figure 2 shows that acetylene, the most important gaseous component for PAH and surface growth, is reproduced well by the reaction model for the benzene / air flame under slightly sooting conditions (Fig. 2a) and for the strongly sooting ethylene / oxygen / argon flame (Fig. 2b). It is also to be seen from Fig. 2a that the prediction with DLR#new where the C_1-and C_2-kinetics is based on the GRI-mechanism gives definitely too low concentration values. Figure 2 also shows that the profiles of other aliphatic hydrocarbons such as ethene (Fig. 2a) and diacetylene (Fig. 2b) are predicted sufficiently well.

3.2 *Aromatics*

Measured concentration profiles of different aromatics ranging from one- to four-membered rings, some of them with a side chain, are compared with model predictions in Figures 3-5 which correspond to the three flame investigations. The names of the PAHs were assigned in the graphs to the usual symbols (Table 1).

Table 1: Chemical notation of the used aromatics

Name	Structure	Mass (a.m.u.)	Graph	Name	Structure	Mass (a.m.u.)	Graph
Benzene	C_6H_6	78	A1	Naphthalene	$C_{10}H_8$	128	A2
Phenylacetylene	$C_6H_5C_2H$	102	$A1C_2H$	Acenaphthalene	$C_{12}H_8$	152	A2R5
Styrene	$C_6H_5C_2H_3$	104	$A1C_2H_3$	Phenanthrene	$C_{14}H_{10}$	178	A3
Biphenyl	C_6H_5-C_6H_5	154	P2	Pyrene	$C_{16}H_{10}$	202	A4

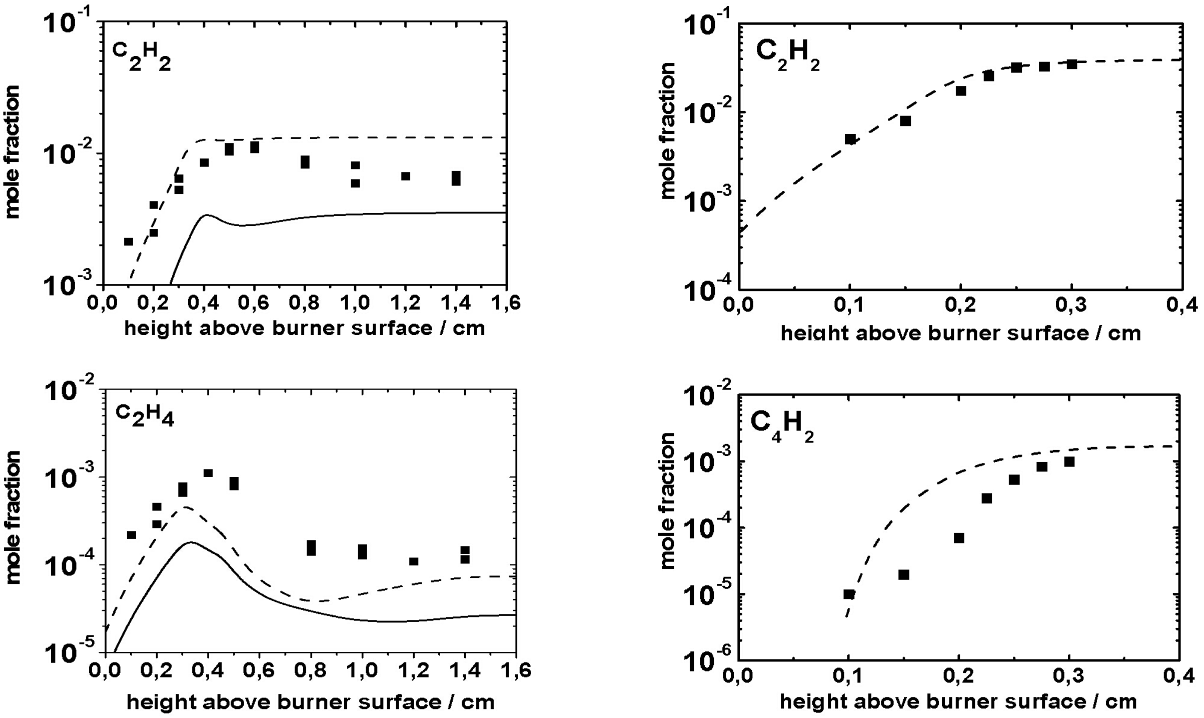

Figure 2: Comparison between model prediction and experiment for smaller aliphatic hydrocarbons in premixed laminar atmospheric flames. Experiment: ¦ , model: dashed line (DLR#old), full line (DLR#new). Fig. 2a (left side): benzene / air with C / O = 0.72 (Tregrossi et al.(1999)). Fig. 2b (right side): ethene / oxygen / argon with C / O = 0.92 (Harris et al. (1988)).

3.2.1 *A1-aromatics*

Benzene profiles are well reproduced by the DLR model for the benzene / air (Fig. 5) and ethene / oxygen / argon flames (Fig. 4). The mechanism from Appel et al. is too slow for the benzene decomposition and therefore higher values at larger flame heights are predicted. In the methane / oxygen-flame (Fig. 3), benzene concentration is overpredicted by about one order of magnitude by the DLR mechanism and something less by the Appel mechanism. Biphenyl which is formed via path 2 of the reaction scheme displaced in Fig. 1 has been measured only in the benzene flame. The prediction by all models reproduces the shape of the profile well, but the Appel mechanism overpredicts the concentration values by up to one order of magnitude.

For the predictions of concentration profiles for the premixed laminar ethene flame (Fig. 4), the calculations were done only with the DLR base model (DLR#old). The model predictions match the profiles for C_2H_2 (see Fig. 2a) and benzene (Fig. 4) properly and therefore the profile of $A1C_2H$ as well, because $A1C_2H$ is formed by the reaction of C_6H_5 with C_2H_2. In the methane flame (Fig. 3), the initial rise of $A1C_2H$ concentration fits well, but the concentration level at larger flame heights is overpredicted by both models by factors of 2-4. Styrene is expected to play only a minor role for soot precursor formation because it is formed only via a side route reaction sequence. The model fails to simulate the measured profile of $A1C_2H_3$ (Fig. 4) sufficiently, but it has to be pointed out that the mechanism is optimized with respect to acetylene addition reactions.

3.2.2 *A2–aromatics*

Naphthalene, which is generally considered to play a central role for the growth of the PAHs (see Fig. 1), is best reproduced by the Appel model in the methane flame (Fig. 3) and by DLR#old in the benzene flame (Fig. 5). Also, the values for acenaphthalene which has been measured only in the benzene flame at similar concentrations like naphthalene, are reproduced by the DLR#old model.

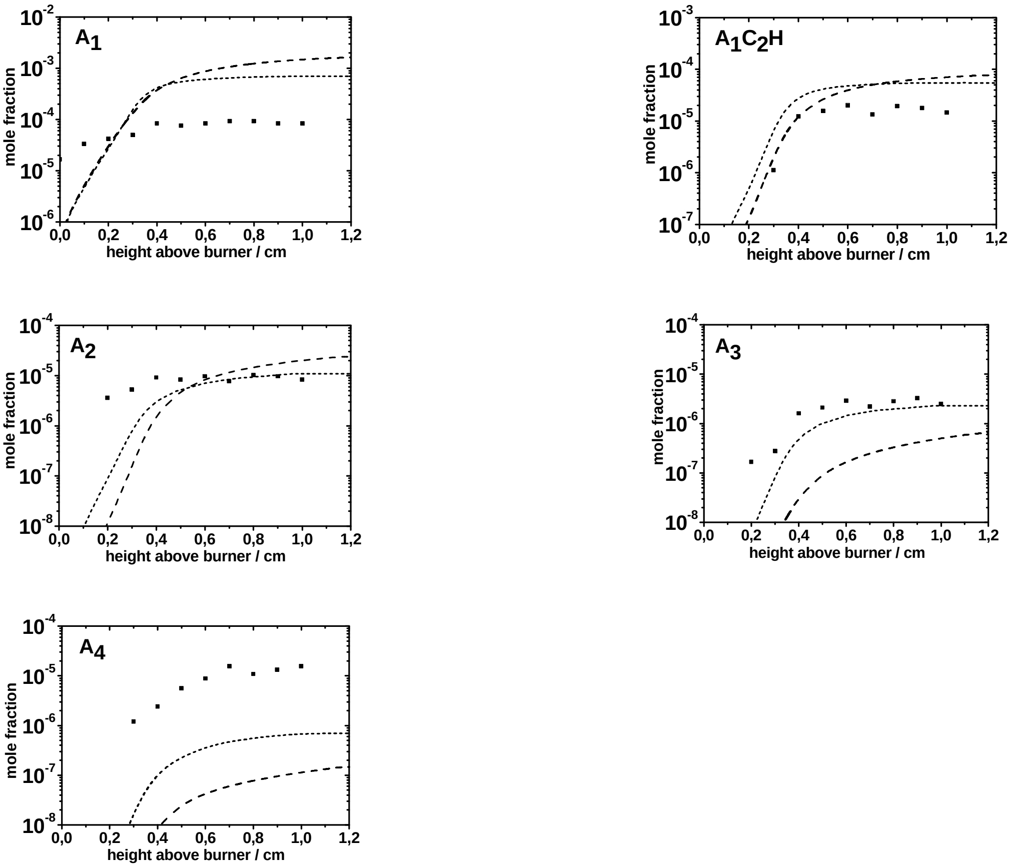

Figure 3: Comparison between model prediction and experimental data for aromatic species in a premixed laminar atmospheric flame with methane / oxygen / argon at C / O = 0.60 (Melton et al. (1998)). Experiment: ¦ , model: dashed line (DLR#old), short dashed line (Appel et al. (2000)).

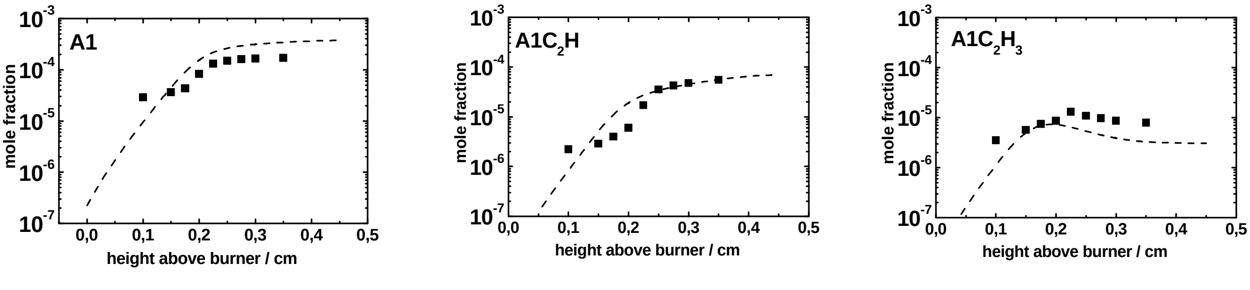

Figure 4: Comparison between model prediction and experimental data for aromatic species in a premixed laminar atmospheric flame with ethene / oxygen / argon at C / O = 0.92 (Harris et al. (1988)). Experiment: ¦ , model: dashed line (DLR#old).

3.2.3 *A3-A4-aromatics*

In the methane flame, phenanthrene is reproduced sufficiently well by the Appel model (Fig. 3) whereas both versions of the DLR model are far above or below the measured data points. In the benzene flame (Fig. 5), all models fail to reproduce the shape of the measured phenanthrene profile, but the quasi constant concentration level at larger heights is at least fit by the DLR#old model. It is not possible to fit the pyrene profiles in both flames. In the methane flame, (Fig. 3) pyrene is underpredicted by Appel and DLR#old by more than one order of magnitude, whereas in the benzene flame (Fig. 5), in the post reaction zone regime, Appel and DLR#new overpredict the experimental data by about two orders of magnitude. DLR#old overpredicts to a lesser extent the post flame data points. As mentioned before, the experimental data base for the rate constants in the PAH mechanism is extremely poor and most of the data have to be estimated from the comparison with similar reactions of smaller cyclic hydrocarbons. Additionally, the thermodynamic data of the polyaromatic species is important for calculating the reverse rate constant, but in the most cases the required thermodynamic data are not available or were deduced from calculations exhibiting enormous error bars. Therefore it is not surprisingly that the prediction of the concentration profiles for larger aromatic species is not satisfactory.

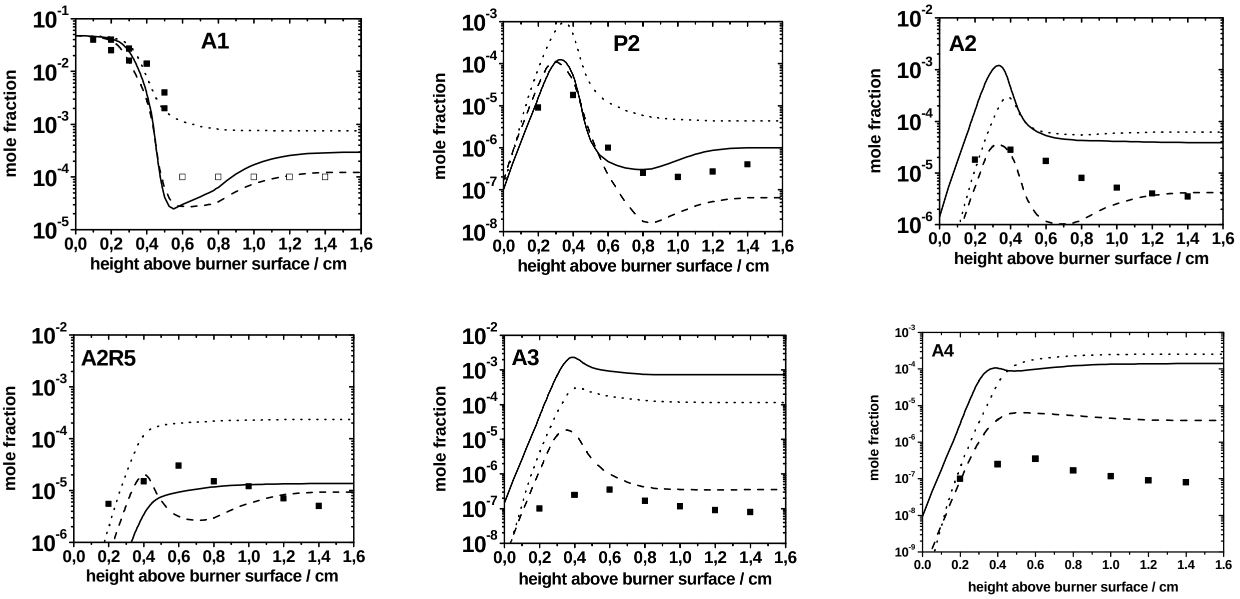

Figure 5: Comparison between model prediction and experimental data for aromatic species in a premixed laminar atmospheric flame with benzene / air at C / O = 0.72 (Tregrossi et al. (1999)). Experiment: ¦ , model: dashed line (DLR#old), full line (DLR#new), dotted line (Appel et al. (2000)).

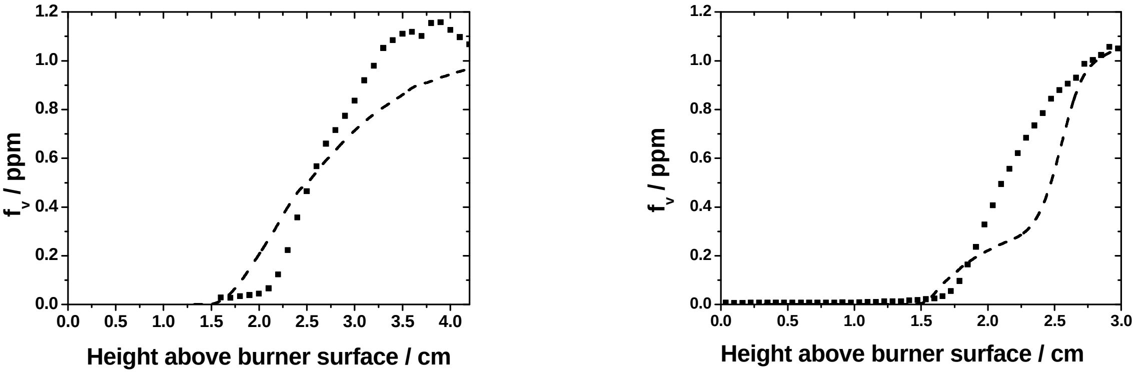

Figure 6: Comparison between model prediction and experimental data of soot volume fraction, fV (ppm), in a premixed laminar atmospheric flame (Geigle et al. (2002)) with ethene / air at C / O = 0.83 (left side) and propene / air at C / O = 0.74 (right side). Experiment: ¦ , model: dashed line (DLR#old + soot module).

3.3 *Soot volume fraction*

Figure 6 shows measured soot volume fractions f_v for rich premixed ethene / air- and propene / air-flames at atmospheric pressure. The temperature profile has been determined by using shifted CARS (Schneider-Kühnle (2003)) with a high spatial resolution, especially close to the burner surface. This provides for a much higher reliability in the simulation of the reaction zone kinetics and therefore for the applied soot model, too. For comparison, Figure 6 presents also model prediction for f_v using the same reaction mechanism for simulation of soot production in the C_2H_4 and C_3H_6 flame. Reasonable agreement with the experimental data is found.

4 CONCLUSIONS

Different gas phase reaction mechanisms were used as base for the prediction of concentration profiles of soot precursors. One mechanism has been published recently by Appel et al. (2000). The others, DLR#old and DLR#new, which contains a modified version for C1-C2-chemistry, have been developed by the authors and were updated by incorporating recent chemical kinetic data for C5 and C6 species. The model predictions were compared with experimental data from laminar premixed flames using different fuels.

The modeling study showed that for different fuels both reaction mechanisms reproduce the measured profiles for C2- to C4-species well, thus indicating that the fuel break-up kinetics is simulated satisfactory. For aromatic A1-to A4-species, which are most important for the formation and growth of soot precursors, the PAH reaction mechanisms show particularly significant differences in the prediction of individual PAHs. The Appel mechanism exhibits smaller deviations from the measured data in the post reaction zone of the methane flame for different PAH levels than the DLR model. This is not surprising because the C1-C3-chemistry in the Appel mechanism is based on the methane GRI 3.0 mechanism. Evidently, the growth of the smaller hydrocarbons to the first ring aromatics reflects the fuel specifity better. On the other hand, the DLR#old model gives values definitely closer to the measured data for the fuels ethene and benzene which is caused by the more detailed kinetic model for the formation of the first ring aromatics. Furthermore, it was shown that the PAH prediction (DLR#new) with benzene as fuel becomes definitely worse for modifying the initial C1-C2- submodel by using a standard methane model (GRI 3.0).

It has been also demonstrated that the model, combined with the particle formation module, is able to simulate the main features of soot production in laminar premixed flames for different fuels, namely ethene and propene.

The results of the present work suggest investigating in more detail the formation routes to higher mass aromatics like pyrene. Such experiments could be done by using tools like single pulse shock tubes or high temperature flow reactors with high temporal resolution. These devices have the advantage of well defined initial conditions, and they allow conducting experiments at much higher pressures. Thus, the experimental data base could be enlarged considerably and may lead to a better understanding of the formation and growth of polycyclic aromatic hydrocarbons as main soot precursors.

REFERENCES

Appel, J., H. Bockhorn, and M. Frenklach, 2000: Combust. Flame 121, 122-136.

Böhm, H. and H. Jander, 1999: Phys. Chem. Chem. Phys. 1, 3775.

Böhm, H., M. Braun-Unkhoff, and P. Frank, 2003: Progress in Computational Fluid Dynamics 3, 145-150 .

Braun-Unkhoff, M., P. Frank, and Th. Just, 1988: Proc. Combust. Inst. 22, 1059-1061.

Braun-Unkhoff, M., P. Frank, and Th. Just, 1990: Ber. Bunsenges. Phys. Chem. 94, 1417-1425.

Frenklach, M. and H. Wang, 1994: Detailed Mechanism and Modeling of Soot Particle Formation.In: Soot Formation in Combustion, Mechanisms and Models, [Ed. H. Bockhorn], Springer-Verlag Berlin, Springer Series in Chemical Physics 59 (1994), pp. 165-190.

Geigle, K.P., V. Krüger, and Y. Schneider-Kühnle, 2002: DLR Stuttgart, private communication.

GRI 3.0, American Gas Research Institute, see http://www.me.berkeley.edu/gri_mech/ (1998).

Harris, S.J., A.M. Weiner, and R.J. Blint, 1988: Combust. Flame 72, 91-109.

Herzler, J. and P. Frank, Ber. Bunsenges. 1992: Phys. Chem. 96, 1333 –1338.

Hu, D., M. Braun-Unkhoff, and P. Frank, 2000: Z. Phys. Chem. 214 (4), 473-491.

Kee, R.J., J.F. Grcar, M.D. Smooke, and J.A.Miller, 1985: “PREMIX”, Sandia National Laboratories, Livermore,CA, Report: SAND85 8240.

Melton, T.R., A.M. Vincitore, and S.M. Senkan, 1998: Proc. Combust.Inst. 121, 1631– 1637.

Richter, H, W.J. Grieco, and J.B. Howard, 1999: Combust. Flame 119, 1-20.

Roy, K., C. Horn, P. Frank, V. Slutsky, and Th. Just, 1998: Proc. Combust. Inst. 27, 329-336.

Scherer, S., Th. Just, and P. Frank, 2000: Proc. Combust. Inst. 28, 1511-1518.

Schneider-Kühnle, Y., 2003: Experimentelle Untersuchungen russender Hochdruckflammen mit laserdiagnostischen Messmethoden. PhD Thesis, DLR Stuttgart, in preparation.

Tregrossi, A., A. Ciajolo, and R. Barbella, 1999: Combust. Flame 117, 553-561.

Wang, H. and M. Frenklach, 1997: Combust. Flame 110, 173-221.

Modelling of Volatile Particles during PARTEMIS

X. Vancassel, P. Mirabel[*]
Centre de Géochimie de la Surface, Université Louis Pasteur, Strasbourg, France

A. Sorokin
Central Institute for Aviation Motors, Moscow, Russia

Keywords: nucleation, aerosol, aircraft emissions, modelling

ABSTRACT: A microphysical model has been used in order to study volatile particles formation in the sampling system of the PartEmis European experiment. The fraction ε of the fuel sulphur S(IV) converted into S(VI) has been indirectly deduced from comparisons between model results and measurements. ε has been found to be in the range 2.5 % to 6 %, depending on the combustor settings and on the microphysical approach used. Different processes have been investigated, comprising soot particles activation and possible growth. Growth factors of monodisperse particles transported in the line and then exposed to high relative humidity (95 %) have been calculated and compared with experimental results. Results show interesting trends of increasing growth factors with decreasing size.

1 INTRODUCTION

Volatile particles formed in aircraft exhaust plumes may play an important role on the atmosphere chemical composition, radiation processes and cloud coverage (IPCC, 1999). The understanding of the potential impacts of aircraft generated aerosol still requires a better knowledge of the mechanisms of particle precursors formation and of ultrafine volatile particles generation. Numerous papers, involving in-situ measurements (e.g. Schröder et al., 1998) and also modelling studies have emphasized the role of sulphur, chemi-ion and organic compounds on aircrafts plume microphysical processes (e.g. Kärcher et al., 1998; Yu et al., 1999). However, the effect of engine operating conditions on the formation of these particles is not yet well understood. There is evidence that the number of volatile particles increases with increasing levels of sulphur in the fuel, but the conversion rate ε at which the original sulphur IV is transformed to S(VI) i.e. SO_3 and H_2SO_4 remains highly discussed as a wide range of values has already been suggested (Schumann et al., 2002).

An extensive set of gaseous species and aerosol measurements have been conducted on a jet engine combustor test rig, in the frame of the EU project PartEmis. One of the goals of PartEmis was to gain more information about the rate of sulphur conversion. For this, gaseous S(VI) (SO_3+H_2SO_4) has been measured by chemical ionization mass spectrometry (Katragkou et al., subm.). Liquid aerosol particles measurements were achieved by operating a multi-channel Condensation Particle Size Analyzer (CPSA). Only the concentrations of particles in the size range 4-7 nm, have shown a dependency on the Fuel Sulfur Content (FSC) used during the test campaign (Petzold et al., 2003). Furthermore, the hygroscopic properties of particles with dry diameters > 30 nm were measured with a Hygroscopicity Tandem Differential Mobility Analyzer (H-TDMA). To support these experiments, several modelling studies have been undertaken and in this article, we present modelling studies of the formation of volatile particles and of the hygroscopic properties of soot particles. The calculations have been performed with a microphysical comprehensive model.

---

[*] *Corresponding author*: Philippe Mirabel, Centre de Géochimie de la Surface, Université Louis Pasteur, 1 rue Blessig, 67084, Strasbourg, France. Email: mirabel@illite.u-strasbg.fr

2 EXPERIMENTAL SETUP AND SAMPLING SYSTEM

A brief description of the combustor and test-rig used during PartEmis, is given below, and further details can be found in Wilson et al. (2003). The exhaust was sampled close to a combustor exit by a probe (4 mm inner diameter), laterally moved to eleven traverse positions (position 6 was central). This allowed the lateral distribution of gaseous precursors and particles to be measured. After exiting the probe, the sample temperature was rapidly quenched to minimise post sampling reactions, by a water cooling system, bringing its temperature to about 420 K avoiding any condensation of water and unburnt hydrocarbons in particular. The exhaust was then split and delivered to a diluted and to an undiluted sampling line which supplied each participant with the desired fraction of the sample. The diluted line, which concerns this study, was not insulated (contrarily to the undiluted line sample) and the sample naturally attained room temperature (~ 20°C) after dilution by a factor of about 60-65. Dilution was achieved by means of a capillary tube with particulate free air at ambient conditions (293 K, 1052 hPa). The last part of the sampling line had an inner diameter of 21.12 mm and the total transit time was approximately 0.9 s from the tip of the probe to the measurement devices. Two settings were used, in order to reproduce "old" and "modern" cruise conditions and three different fuel sulphur contents FSC = 50, 410 and 1270 ppm have been tested. As the extraction probe was very close to the exit smile, the temperature of the exhaust gases in the first part of the sampling line remained high (above 430 K) until the dilution point was reached. Therefore, no condensation was expected in this part of the sampling line. On the contrary, the dilution of the sample with air at ambient temperature cooled it down very rapidly (more than 100°C in less than 10 ms), leading to a local supersaturation of the condensing vapors. Therefore, particle formation was expected to take place only in the sampling line, just after the mixing of the sample with the cold diluting air. Indeed, volatile particles were detected at the end of the sampling line, in the 4-7 nm size range but only for the high fuel sulphur case (FSC = 1270 ppm). The model calculations made confirm that only for theses high FSC volatile particles are expected to be analysed with this experimental set up.

3 MODEL DESCRIPTION

Classical homogeneous heteromolecular nucleation theory, generally invoked to explain the formation of volatile particles seems unable to properly describe their formation in aircraft plumes because of the use of a steady state approach leading to time lag effects in a fast changing system (e.g. Taleb et al. 1997). Indeed, in a plume, the temperature cools down very rapidly due to the entrainment of very cold ambient air in the wake. As a consequence, we have used a "kinetic" microphysical approach, similar to the one used by Yu and Turco (1997) (see also Yu and Turco, 2001). The model, based on coagulation processes in the sulphuric acid-water binary mixture (Sorokin et al., 2001) takes into account both charged (ions or charged clusters) and neutral species (molecules or clusters), the presence of charges having a stabilizing effect on clusters and enhances growth and coagulation. Contrarily to the classical nucleation theory which assumes that particles result from collisions between clusters and single molecules (or hydrates), the kinetic approach includes in addition cluster-cluster collisions. Given the very strong binding energy between sulphuric acid and water molecules, the formation of hydrates is expected in the vapor phase (e.g. Heist and Reiss, 1974). The initial distribution of sulphuric acid hydrates has been calculated following Wilemski and Wyslouzil self consistent assumptions (Wilemski and Wyslouzil, 1995). The subsequent growth due to coagulation of these clusters and condensation (condensation has been treated as a special case of coagulation) has led to the formation of stable particles, classified into "size-bins" according to their acid content. In addition to volatile particles, the presence of soot particles in the exhaust has been considered. A log normal distribution has been proposed from measurements results, depending on the probe position. The emission index was typical for common aircraft engines (PEI=10^{14} to 10^{15} /kg fuel) and the mean size was around 37-40 nm, for old and modern cruise respectively. The interactions between soot particles and gaseous species (water and sulphuric acid) as well as their interaction with volatile particles have been included in the model. Another key parameter for volatile particles modelling is the Chemi-Ion emission index at the combustor exit. A value of the CI emission index of $5.3.10^{17}$ /kg has been proposed by the

Max Planck Institut (MPI) of Heidelberg. We mainly used this value as a reference one although we have performed a sensitivity analysis of the CI effects on volatile particles growth. The system of intrusive sampling used to carry out measurements during the Partemis campaign has required the integration of peculiar processes to describe the evolution of species in the exhaust plume. The possible interaction between aerosols (volatile particles and soot) or gaseous species with the flow pipe walls has been taken into consideration. Concerning soot adsorption on the surfaces of the sampling line, we have followed the work by Hurley (1996) who provided the ratio N_{soot}/N^0_{soot} of leaving to entering soot number densities in a tube. It is interesting to note that the losses were found independent of the particle number density and size. For stainless steel, the losses have been calculated according to the following semi-empirical equation:

$$\frac{N_{soot}}{N^0_{soot}} = \exp\left(-\left(1.05\times10^{-4}V + 2.27\times10^{-4}\right)\frac{L}{dV}\right) \qquad (1)$$

where V is the sample mean velocity, L the pipe length and d its diameter. Equation 1 has been used for the series of pipes of different sections with varying flow rate, which constitute the PartEmis sampling line geometry. Concerning volatile particles, wall losses have been neglected from the tip of the probe to the diluter, as the sample was heated at 423 K to prevent condensation. But after dilution, the estimated material losses due to wall effects, enhanced by the turbulent behaviour of the flow (Reynolds number Re>30000), was estimated following for instance the work of Brockmann et al. (1982). The volatile particles number density evolution in the tube can be calculated using the first order equation :

$$\frac{\partial N(r,t)}{\partial t} = -\frac{4k_T(r,T)}{d}N(r,t) \qquad (2)$$

where N(r,t) is the number density of volatile particles of radius r at time t after the diluter, k_T is the mass transfer coefficient determined according to Friedlander (1977) (see for example Brockmann et al., 1982)

$$k_T = 0.042Vf^{1/2}Sc^{-2/3} \qquad (3)$$

where f is the friction factor, Sc the Schmidt number which estimates the ratio between the viscosity of air and the particle diffusivity.

4 RESULTS AND DISCUSSION

4.1 *Volatile particles*

One of the main uncertainties to calculate the losses is the value to be affected to the sticking coefficient, i.e to determine a collision efficiency (CE) between particles or clusters colliding on the tube walls. Several values of CE have been used, from 50 % to 100 % (maximum possible value) as this parameter remains poorly known. Actually, even for condensation and particles collisions, theoretical studies as well as experiments have led to quite different values of accommodation coefficient (Van Dingenen and Raes, 1991; Clement et al., 1996). Figure 1 which gives the results of the simulations for high FSC, shows the sulphur conversion factor required for the model to provide a good agreement with measured volatile particles concentration in the size range from 4 to 7 nm. The different curves correspond to different values for the assumed CE and sulphur conversion factor ε. For the maximum possible value CE = 100 %, the sulphur conversion factor reaches a mean value of about 5.2 % for old and 5.7 % for modern cruise conditions. However, if the CE is reduced to 50 % (still a rather high value), ε mean values translate to 2.5 % and 2.8 % respectively. These last values provide very reasonable agreement both with the measured concentration of volatile particles and ε values deduced by the MPI group, although most of these results have been determined in the wake, and not at the combustor exit (e.g Curtius et al., 2002). Note that results for the first and last positions of the probe, close to the combustor wall have not been presented here, as the air fuel ratio (AFR) in these cases was much higher than the average value (approximately twice the average AFR). It should also been noted that even for a sulphur conversion > 5 % no volatile particles are expected to be seen at the end of the sampling line from our results, for the low and medium sulphur case which has been confirmed by observations. The sulphur conversion ε and the collision efficiency on walls are not the only parameters which have an influence on particles growth. Chemi-ion concentrations, which were measured during PartEmis, may play also a major role. As already noted, we have used an emission index of $5.3.10^{17}$ /kg at the combustor exit but a variation of a factor ten in this concentration has only a limited influence on the results presented in Figure 1.

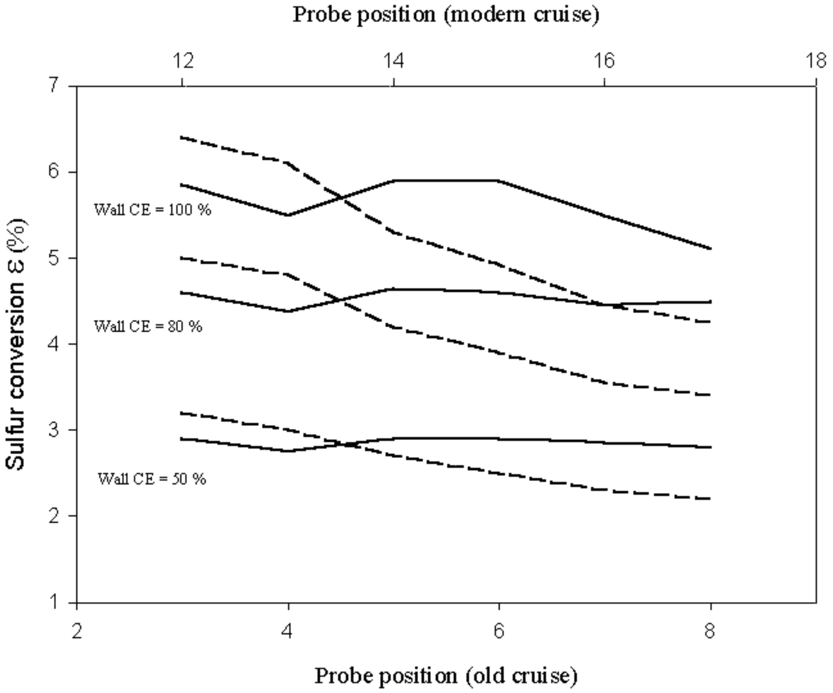

Figure 1. Required SC to fit DLR volatile particles measurements as a function of the probe position. Case of high FSC (1270 ppm). Old cruise conditions: position 3 to 8. Modern cruise conditions: position 12 to17. dashed lines: old cruise (bottom axis). Full lines: modern cruise (top axis)

4.2 *Hygroscopic properties of soot particles*

Soot particles have been taken into account in our calculations and we have studied the ability of the model to reproduce soot particles growth measurements, as they have been carried out by Gysel et al. (2003). Actually, studies of soot hygroscopicity are of main importance as soot activation is a key process for their subsequent growth and transformation into contrails. To summarize briefly these experiments, a monodisperse fraction of particles has been sampled, at the end of the sampling line, and then exposed to a rather high relative humidity (up to 95 %). Although soot activation has recently been observed to occur even with sulphur free kerosene (O. Popovicheva, pers. comm.), Gysel et al. (2003) have shown a clear dependence between the fuel sulphur content and the growth factor defined as the ratio between the wet and the dry (initial) diameter of soot particles, calculated once they have been exposed to high humidity conditions. As volatile and soot particles undergo scavenging processes, soot particles have gained a sulphuric acid-water coating as they have been transported in the sampling line. We have then checked if the model results could match experimental results, concerning both the measured growth factor and the estimated sulphuric acid weight fraction of the layer. The growth factor is characterized by a slight increase close to the diluter when the sample is mixed with the diluting air whose humidity is higher. Then the liquid coating evaporates slightly as both water and sulphuric acid molecules are lost on the walls or are depleted due to nucleation and condensation processes. At the end of the sampling line, when the sample enters the H-TDMA the sudden increase of relative humidity, up to 95 % brings about a sudden growth of soot particles. As noted by Gysel et al. (2003), the smaller the particles, the larger the growth factors are and no significant difference was detected between old and modern conditions (especially if error bars are included). These observations were confirmed by our modelling study since the calculated growth factors are 1.14, 1.11 and 1.07 respectively for particles having initial diameters of 30, 40 and 50 nm before extraction. These values are close to those calculated for other probe positions and have been obtained using a wall CE of 50 % and a sulphur conversion corresponding to the one required to fit volatile particles concentration to the measurements carried out by the DLR (ε = 2.5 %-2.8 %).

Table 1 gives a comparison between calculated and measured growth factors and acid volume fractions of the surface layer, for the high FSC case (FSC=1270 ppm). One notes a good agreement for the general trends, i.e. increase of both growth factors and acid volume fractions with decreasing size. However, the values may be quite different, especially for the acid volume fraction.

Table 1. Experimental (Gysel et al., 2003) and model results (this work). Comparison of soot particles growth factor and sulphuric acid volume fraction for modern cruise operating conditions at high FSC (1270 ppm). The growth factor is calculated as the ratio between the particles diameters considered just before they enter the condensation chamber and after they reach equilibrium in it.

Dry diameter	Calculated growth factor	Measured growth factor	Calculated acid volume fraction	Estimated acid volume fraction
nm			%	%
30	1.14	1.23	14.0	21.0
50	1.11	1.16	9.6	9.5
100	1.07	1.07	8.4	3.0

5 CONCLUSIONS

A modelling study of volatile particle formation has been presented in the frame of the PartEmis project, in order to study the role of sulphuric acid on particles formation and growth. A sulphur conversion factor ε has been indirectly deduced from the comparison between experimental results and model calculations. Taking into account the absence of accurate monitoring of water vapour along the line, and the lack of line transmission information, average values in the ranges 2.5 % - 5.7 % have been calculated, depending on the collision efficiency of particles and clusters on the walls. The last value of ε cited (5.7 %) represents an upper limit since it has been deduced for the maximum collision efficiency between particles and sampling line walls. The soot growth factor study has pointed out similar trends between measured and calculated values. In particular, the growth factor increased as the soot particle size decreased (Gysel et al., 2003). The role of sulphuric acid remains very important, although the binary system may not be completely able to predict accurately particles concentration, especially in a complex system such as a sampling line. Our modelling study did not include the possible contribution of organics on the growth process. However, previous studies have shown that this role appears to be important only for low FSC (of the order of 100 ppm or less). Another source of uncertainty is the possible presence of ammonia (which was not monitored) in the diluting air, as ammonia is known to lead to ternary nucleation with the sulphuric acid-water mixture. If ammonia was indeed present, nucleation would have been enhanced and the value of ε needed in the model would have been reduced. Again, this confirms that the ε values given in this work should be considered as upper limits.

6 ACKNOWLEDGEMENTS

Support of this work by the European Community through contract G4RD-CT-2000-00207 (PartEmis) and by the INTAS project OPEN 2000-460, as well as fruitful discussions with the PartEmis participants are gratefully acknowledged.

REFERENCES

Brockmann, J.E., P.H. McMurry, and B.Y.H. Liu, 1982: On simultaneous coagulation and diffusional loss of free molecule aerosols in turbulent pipe flow. *Aeros. Sci. Tech.* 1, 163-178.

Clement, C.F., M. Kulmala, and T. Vesala, 1996: Theoretical considerations on sticking probabilities. *J. Aeros. Sci.* 27, 869-882.

Curtius J., F. Arnold and P. Schulte, 2002: Sulfuric acid measurements in the exhaust plume of a jet aircraft in flight: Implications for the sulphuric acid formation efficiency. *Geophys. Res. Let.* 29, doi: 10.1029/2001GL013813.

Friedlander, S. K.: 1977, Smoke, Dust and Haze, Eds Wiley, New York.

Gysel, M., S. Nyeki,, E. Weingartner, U. Baltensperger, H. Giebl, R. Hintzenberger, A. Petzold, and C.W. Wilson, 2003: Properties of jet engine combustor particles during the PartEmis experiment. Hygroscopicity at subsaturated conditions. *Geophys. Res. Let.* 30, 1566, doi: 10.1029/2003GL016896.

Heist, R.H, and H. Reiss, 1974: Hydrates in supersaturated binary sulfuric acid-water vapor. *J. Chem. Phys.* 61, 573-581.

Hurley, C.D., 1996: Measurements of particulates from an engine combustor. AEROTRACE proceedings, Impact of Aircraft Emissions upon the Atmosphere, Paris. Vol. 1, 113.

Intergovernmental Panel on Climate Change (IPCC), 1999: Aviation and the Global Atmosphere. Cambridge Univ. Press, New-York.

Kärcher, B., F. Yu, F.P. Schröder and R.P. Turco, 1998: Ultrafine aerosol particles in aircraft plumes: Analysis of growth mechanisms. *Geophys. Res. Let.* 25, 2793-2796.

Katragkou, E., S. Wilhelm, F. Arnold, and C. Wilson, 2003: Sulfur (VI) in the simulated internal flow of an aircraft turbine engine: first measurements. Submitted to *Geophys. Res. Let.*

Petzold, A., C. Stein, S. Nyeki, M. Gysel, E. Weingartner, U. Baltensperger, H. Giebl, R. Hitzenberger, A. Dopelheuer, S. Vrchoticky, H. Puxbaum, M. Johnson, C.D. Hurley, R. Marsh, C.W. Wilson, 2003: Properties of jet engine combustion particles during the PartEmis experiment: Microphysics and Chemistry. *Geophys. Res. Let.* 30, doi: 10.1029/2003GL017283.

Schröder, F., B. Kärcher, A. Petzold, R. Baumann, R. Busen, C. Hoell, and U. Schumann, 1998: Ultrafine aerosol particles in aircraft plumes: in situ observations. *Geophys. Res. Let.* 25, 2789-2792.

Schumann, U., F. Arnold, R. Busen, J. Curtius, B. Kärcher, A. Kiendler, A. Petzold, H. Schlager, F. Schröder, and K.-H. Wohlfrom, 2002: Influence of fuel sulfur on the composition of aircraft exhaust plumes: The experiments SULFUR 1-7. *J. Geophys. Res.* 107, doi: 10.1029/2001JD000813.

Sorokin, A., X. Vancassel and P. Mirabel, 2001: On volatile particle formation in aircraft exhaust plumes. *Phys. Chem. Earth (C).* 26, 557-561.

Taleb, D. E., R. McGraw, and P. Mirabel, 1997: Time lag effects on the binary homogeneous nucleation of aerosols in the wake of an aircraft. *J. Geophys. Res.* 102, 12885-12890.

Van Dingenen, R., and F.Raes, 1991: Determination of the condensation accommodation coefficient of sulphuric acid on water-sulphuric acid aerosol. *Aero. Sci. Tech.* 15, 93-106.

Wilemski, G., and B.E. Wyslouzil, 1995: Binary nucleation kinetics. I. Self consistent size distribution. *J. Chem. Phys.* 103, 1127-1136.

Wilson, C.W., A. Petzold, F. Arnold et al., 2003: Measurement and prediction of emissions of aerosols and gaseous precursors from gas turbine engines (PartEmis): An experimental overview. Submitted to *Aerosp. Sci. Technol.*

Yu, F., and R.P. Turco, 1997: The role of ions in the formation and evolution of particles in aircraft plumes. *Geophys. Res. Let.* 24, 1927-1930.

Yu, F., R.P. Turco, and B. Karcher, 1999: The possible role of organics in the formation and evolution of ultrafine aircraft particles. *J. Geophys. Res.* 104, 4079-4087.

Yu, F., and R.P. Turco, 2001: From molecular clusters to nanoparticles: Role of ambient ionization in tropospheric aerosol formation. *J. Geophys. Res.* 106, 4797-481.

Dispersion and Growing of Ice Particles in a Turbulent Exhaust Plume

F. Garnier*[1,2], C. Ferreira Gago[1], A.-L. Brasseur[1]
[1]*Office National d'Etudes et de Recherches Aérospatiales –O.N.E.R.A - France*
[2]*Université de Marne-la-Vallée,– L.E.T.E.M - France*

R. Paoli, B. Cuenot
CERFACS/CFD - France

Keywords: Wake vortices, Numerical simulation, Exhaust jet, Turbulence, Contrails, Two-phase flows

ABSTRACT: Contrails may have an impact on cloudiness and may affect the Earth's radiative budget balance. In order to better understand their formation, preliminary study on the dispersion of gas and particles (soot and ice) in the exhaust jet and on their modification by wake processing has been performed. This work is focused on the 3D numerical simulation of dynamics and microphysics in a near-field of an aircraft wake. Large Eddy Simulations have been carried out at realistic flight Reynolds number to evaluate the effects of turbulent mixing and wake vortex dynamics on gas and particle mixing.

1 INTRODUCTION

Aircraft exhaust contains products resulting from combustion in gas or solid phase. Ice particles that mainly nucleate on exhaust soot and volatile aerosols can lead to the formation of contrails which may have an impact on cloudiness and may affect the Earth's radiative budget balance. In order to better understand the formation of contrails, fundamental studies on the dispersion of gaseous and particles (soot and ice particles) in the near field of an aircraft wake and their modification by plume processing are necessary.

In this article a condensed survey is given on unsteady numerical simulations of the plume processes that were in part already described in previous publications. A detailed description of the different numerical approaches is given in the works of Ferreira Gago *et al.* (2002), Paoli *et al.* (2002) and Paoli *et al.* (2003).

The numerical simulations of the flow are based on the use of 3D temporal DNS/LES of the compressible Navier-Stokes equations. In the LES approach, these equations are filtered in order to reduce the number of scales to be solved. Among the various subgrid scale viscosity and heat flux models used in the LES works, the compressible version of the hybrid Smagorisky model (linear combination of the Smagorinsky and the similarity model) and the Structure Function model displayed the best performances, especially when dealing with the turbulent stresses and the turbulent heat flux (Ferreira Gago et al., 2003; Métais and Lesieur, 1992). The LES equations are solved by using a sixth-order compact scheme in space and the time marching scheme is a three-order Runge-Kutta algorithm.

In the present work we have focused on the simulation of contrail formation and early-stage evolution in the near field of an aircraft wake (i.e. up to a few seconds from the emission time).

Eulerian two-fluid models of particle-laden flow are based on a volume averaging approach, describing macroscopic properties (phase volume fractions, average solute mass fractions and velocities…) of a two-phase mixture. This work uses the alternative Lagrangian particle tracking approach. It seems more suited to the future modeling needs of microscopic phenomena occurring in the exhaust jet and vortex wake of an aircraft (activation of soot, ice crystal condensation and

---

[*] *Corresponding author:* Garnier, ONERA - DMPH/EAG - 29 avenue de la Division Leclerc - BP 72 - 92320 Chatillon - FRANCE. Email: f.garnier@onera.fr

coagulation of volatile aerosols). Due to the small size of the soot-ice particles (from tens of nanometers to a few microns), their relaxation time is negligible compared to the characteristic times to the filtered variables. This allows them to be treated as a tracer. In addition due to the high number density (about 2.5 10^{11} m^{-3}, Karcher *et al.*, 1996), we can carry only packets of particles where each one containing a large number (10^{+6}) physical particles. In the coupling terms which are involved in the LES equations, we only consider the mass exchange, i.e. vapor condensation on the soot particles (so the thermal coupling will be neglected).

2 AIRCRAFT PLUME DYNAMICS

2.1 *Jet/vortex interaction*

In the near field of the aircraft wake, the exhaust jets of the engine are entrained into the counter-rotating wingtip vortices. The entrainment process and the associated turbulent mixing are complex and it is convenient to identify two overlapping regimes (Garnier *et al.*, 1997): the jet and interaction regimes. The first one is that of usual co-flowing jets and it scales with the jet diameter. Later, the interaction of exhaust jet and the wake vortex characterizes the second regime. The convection and shearing processes associated with the tangential velocity field of the trailing vortex strongly affect the exhaust jet dispersion. In the present numerical study, these two regimes are modeled sequentially. The axial length of the domain of 6 nozzle radii corresponds to twice the wave length of the maximum growth rate of the first azimuthal instability of a spatially evolving jet (Michalke and Herman, 1982). An instable nozzle outlet velocity profile is prescribed. When the jet simulation has reached an age that corresponds to a downstream distance of 0.5 wingspans, the cross section of the domain is enlarged and a Lamb-Oseen vortex is superimposed on the flow field at a distance of 14 vortex core radii from the jet center.

An experiment detailed in Brunet *et al* (1999), delivers a database that can be used for improving the numerical simulations. The wake of a generic model corresponding to a rectangular plan form NACA0012 equipped with two heated jets is investigated. The experimental results comprise mean and fluctuating velocity fields (measured with a LDV system) and mean temperature field (measured with thermocouples). Unsteady aspects of the flow are also described by means of hot wire measurements. The experimental results show that the flow does not affect the engine jet behaviour until a downstream distance of 0.5 wing spans. For modern large transport aircraft, the characteristic size of the jet regime is of the order of 1-50 diameters of the nozzle exit, while the deflection regime, scaled to the wingspan, extends downstream of the aircraft to a distance of about 0.5-10 wingspans.

Thereafter numerical results are compared with the experimental database, and an example of the results is shown in Figure 1 where the downstream variations of temperature T peak values are represented. The temperature evolution throughout the near field of the wake as obtained from numerical predictions is in agreement with the experimental results.

2.2 *Gaseous exhaust mixing*

In order to illustrate the entrainment and mixing processes of the gas exhaust, we examine the contours of axial vorticity and species concentration (defined as a passive scalar concentration) as shown in Figure 2. The turbulence induced by the exhaust jet is wrapped around the wing-tip vortex. This interaction results in the generation of small scale motions close to the vortex core and rearranges to coherent secondary vorticity structures (but now ring shaped) of opposite signs. The region very close to the core retains its positive axial vorticity contours, but they are no concentric anymore. At this stage, one can see that the gaseous exhaust dispersion is mainly controlled by these new organized structures.

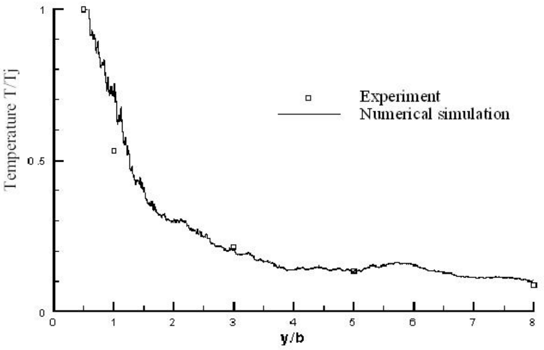

Figure 1. Downstream evolution of the dimensionless temperature T/Tj, where Tj is the nozzle exit temperature. Comparison with experimental data.

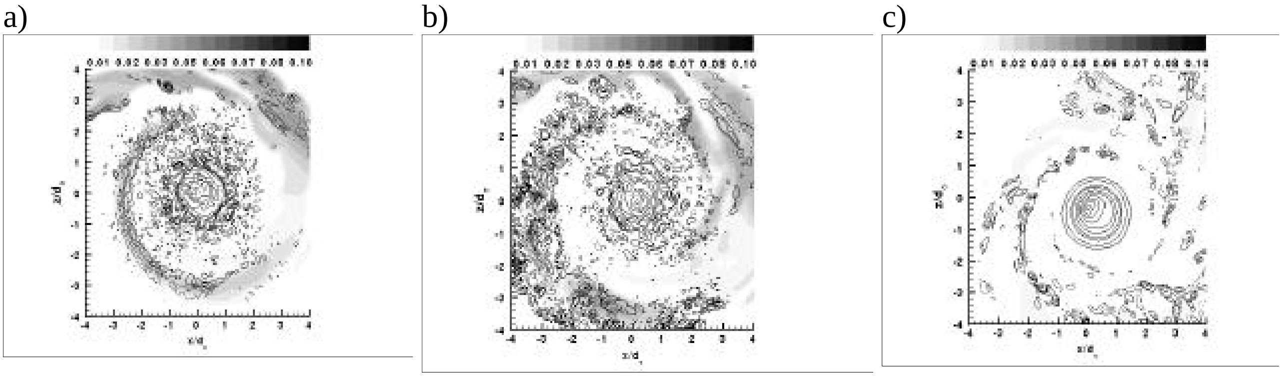

Figure 2. Numerical axial component of vorticity Ω_y in a meridional cross plane. Contour range from –1 to 4 in steps of 0.2 for levels between –1 and 1, and in steps of 0.5 for levels between 1 and 4. Exhaust gas concentration is represented by gray flood contours. (a) *y/b*=6.5, (b) *y/*b=9.2, (c) *y/b*=13.1.

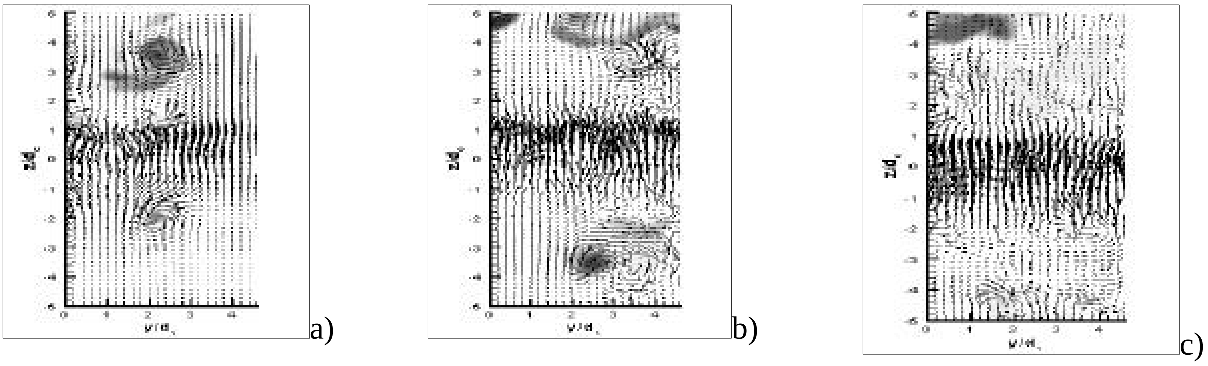

Figure 3. Velocity vector fields in (y,z) plane, at x = 0. Exhaust gas concentration is represented by gray flood contours. (a) *y/b*=6.5, (b) *y/*b=9.2, (c) *y/b*=13.1.

It is also noticed in Figure 3 where velocity vectors are superimposed on the species distribution. Entrainment process results in the trapping of the gas exhaust into the large scale secondary vortices (see Figures 3a and 3b). The species concentration provides a reliable signature of where the helical instability occurs outside the vortex core. Finally, the resulting species field distribution shows no aircraft exhaust products inside the primary vortex core as observed in Figures 2c and 3c.

3 CONTRAIL FORMATION

This paragraph describes the results of the simulation of ice formation in the near field of an aircraft.

A simple micro-physics model for ice growth has been used to couple ice and vapor phases. LES have been carried out at a realistic flight Reynolds number to evaluate the effects of turbulent mixing and wake vortex dynamics on ice growth characteristics and vapor thermodynamic properties.

In the first simulation, the micro-physics ice growth model is switched off. The aim is to obtain a reference mixing case at high Reynolds numbers typical of aircraft wake configurations. It was also useful to analyse the spatial distribution of supersaturated particles and identify the regions where ice formation is most likely to occur.

All particles are initially (at t = 0.16 s) placed below the saturation curve $p_s(T)$ because they are still concentrated inside the hot jet region. Due to the mixing with cold air, particles cool, until some of them become supersaturated (crossing of p_s curve at t = 0.56 s). The spatial distribution of supersaturated particles is given in Figure 4, together with a plane cut of water vapor content at two times during the jet phase. The figure shows that air first saturates around the particles, placed at the edges of the jet where the temperature is fallen and there is sufficient vapor to condense.

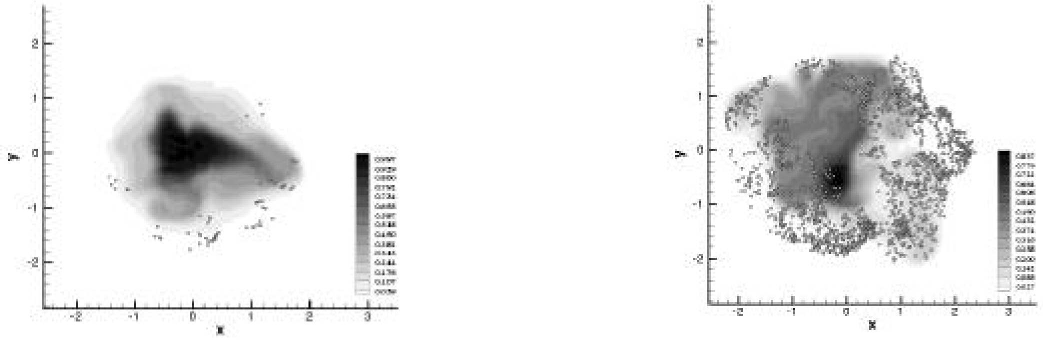

Figure 4. Passive particle case (jet phase). Plane cut of vapor content and distribution of supersaturated particles ; left, t = 0.56 s ; right, t = 0.7 s.

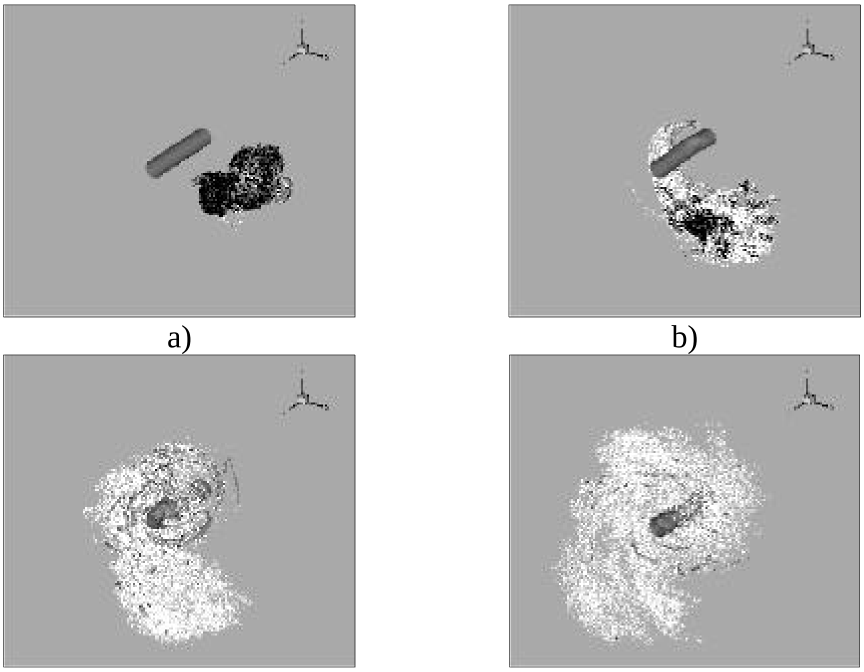
a) b)

c) d)

Figure 5. Passive particle distribution during the jet/vortex interaction phase. Dry soot particles are represented in black, iced supersaturated particles in white. Total vorticity iso-surface identifies the vortex core and the secondary vortical structures due to the interaction with the jet ; a) t = 0.7s ; b) t = 1s ; c) t = 1.5 s ; d) t = 2 s.

The dynamics of the interaction phase are dominated by formation of three-dimensional structures of azimuthal vorticity associated to the entrainment of the jet inside the vortex field. These structures progressively decay (t = 2 s, see Figure 5(d)), corresponding to complete entrainment of the exhaust jet. This mechanism of entrainment enhances mixing with external air : therefore, exhaust cooling and vapor condensation are favored by the presence of vortex. Figure 5 shows that at t = 2 s all particles are supersaturated and contrail can form everywhere in the wake.

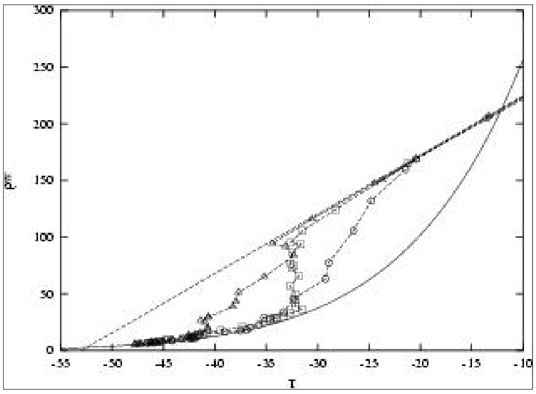

Figure 6. Trajectories of three sample particles in a T - p_w plane.

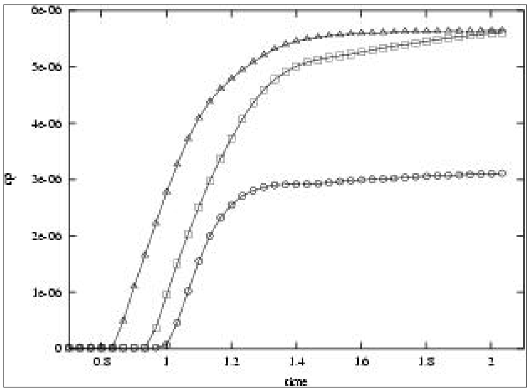

Figure 7. Time evolution of three sample particles radius.

In the second simulations set, the ice growth model is activated. The aim of this calculation is to analyse the early-stage evolution of the contrail and how it influences mixing and the thermodynamic properties of the vapor. Figure 6 displays the trajectories of three sample ice interaction phase when ice/vapor-pressure plane (results are reported only during the interaction phase when ice/vapor coupling is significative). The figure shows that condensation causes large deviations from the mixing line because of vapor removal and the consequent decrease in water partial pressure p_w. In addition, all the particles finally collapse on the saturation curve, $p_s(T)$, which indicates the thermodynamic equilibrium between vapor and ice phases. This is confirmed in Figure 7 by the evolution of ice-particle radii which attain plateau values between 3 and 6 µm.

4 CONCLUSION

This work is focused on the simulation of contrails and early stage evolution in the near-field of an aircraft wake. A numerical simulation of the interaction between an engine jet and a wake vortex has been performed.

To illustrate the entrainment and mixing processes of the exhaust gas, the examination of axial vorticity contours showed that the turbulence induced by the exhaust jet is wrapped around the wing-tip vortex. Results show that the dynamics of the interaction phase are dominated by formation of three-dimensional coherent structures associated to the entrainment of the jet inside the vortex field The evolution of this interaction (i.e. generation of small scale motions close to the vortex core and rearrangement to coherent secondary structures) mainly controls the gaseous exhaust dispersion.

To study the formation of contrail, a simple micro-physics model for ice growth has been used to couple ice and vapor phases. LES have been carried out at a realistic flight Reynolds number to evaluate the effects of turbulent mixing and wake vortex dynamics on ice growth characteristics and vapor thermodynamic properties.

Two simulation sets are made:

- The first simulation is carried out when the micro-physics model is switched off in order to obtain a reference mixing case at high Reynolds numbers, typical of aircraft wake configurations. This analysis provided the spatial distribution of supersaturated particles and it identified the regions where ice formation is most likely to occur. Furthermore, results show that the exhaust cooling and vapor condensation are favored by the presence of vortex.

- The second numerical simulation is performed accounted for ice growth process in order to analyse the early-stage evolution of the contrail and its influence on the mixing and the thermodynamic properties of the vapor. Results show that condensation causes large deviations from the mixing line because of vapor removal and the consequent decrease in water partial pressure. In addition, all the particles finally collapse on the saturation curve and their radii reach plateau values between 3 and 6 µm.

REFERENCES

S. Brunet, L. Jacquin, P. Geoffroy, 1999 : Experiment on heated jet/wake vortex interaction, *ONERA RTY 15/2496 DAFE/Y*.

C. Ferreira Gago, F. Garnier and F. Uthéza, 2003 : Direct testing of subgrid scale models in large eddy simulation of a non-isothermal turbulent jet, *International Journal for Numerical Methods in Fluids (in press)*.

C. Ferreira Gago, F. Garnier and F. Uthéza, 2002 : Numerical investigation of turbulent mixing in a jet/vortex interaction, *AIAA Journal.*,40, 276-284.

F. Garnier, C. Baudouin, N. Louinard, 1997 : Engine Emission alteration in the nearfield of an aircraft, *Atmospheric Environment*, 31, 1767-1781.

B. Karcher, T. Peter, U. Biermannand U. Schumann, 1996 : The initial composition of jet condensation trails, *Journal of Atmospheric Science*, 53, 3066-3083.

O. Metais and M. Lesieur, 1992 : Spectral large-eddy simulation of isotropic and stably stratified turbulence, *Journal of Fluid Mechanics*, 239, 157-194.

A. Michalke and G. Hermann, 1982 : On the inviscid instability of a circular jet with external flow, *Journal of Fluid Mechanics*, 114, 343-359.

R. Paoli, F. Laporte, B. cuenot, T.J. Poinsot, 2003 : Dynamics and mixing in a simple configuration of jet/vortex interaction. *Physics of Fluids*, 15, 1843-1860

R. Paoli, J. Hélie, T.J. Poinsot, S. Ghosal, 2002 : Contrail formation in aircraft wakes using large-eddy simulations, *Center for Turbulence Research, proceedings of summer Program*.

The Effect of Plume Processes on Aircraft Impact

I.C. Plumb[*], L.K. Randeniya, P.F. Vohralik
CSIRO Telecommunications and Industrial Physics, Lindfield, NSW, Australia

S.L. Baughcum
Boeing Company, Seattle, WA 98124, USA

Keywords: Aircraft emissions, Plume chemistry, NOx, NOy, HOx

ABSTRACT: In the present study, we investigate the chemistry of expanding aircraft exhaust plumes for a range of conditions (latitude, altitude, season, plume expansion rate, time of day of emissions, aircraft type, composition of emissions and background air mass). The effect of plume chemistry on 2-D global model calculations of the impact of subsonic aircraft emissions on ozone is discussed.

1 INTRODUCTION

Plume processes are inherently sub-grid scale in multi-dimensional global models, so they need to be studied using off-line models with dimensions of the order of plume dimensions and the effects of plume processes parameterized for inclusion in multi-dimensional models. Several studies have been made of plume processes (Danilin et al., 1994; Meijer et al., 1997; Petry et al., 1998; Moulik and Milford, 1999; Karol et al., 2000; Kraabol and Stordal, 2000; Kraabol et al., 2000b) and different parameterizations have been developed. Kraabol et al. (2002) obtained reductions of 15-18% in calculated ozone changes at cruise altitude due to subsonic aircraft emissions in a 3-D model study when plume processes were included. Meijer et al. (1997) reported similar percent reductions in ozone changes due to aircraft when they included plume processes in their 3-D model study. That study, however, did not include O_3 effective emissions. When these were included, ozone change reductions due to inclusion of plume processes decreased to 0-5% in January and -5% to 10% in July (Meijer, 2001). There is thus considerable uncertainty in the importance of plume processes for aircraft assessment studies.

In the present study, a Gaussian plume model was developed and used to study the chemistry of expanding aircraft plumes for a wide range of conditions. The plume model is described briefly in Section 2. Plume processes were described in terms of two different parameterizations: emission conversion factors and relative emission changes. These parameterizations are defined in Section 3. Section 4 describes some of the results obtained using this model, with particular emphasis on the effect of composition of the background atmosphere on plume composition. These studies allow insight to be gained on the processes which are important for determining the conversion of NOx to NOy in the plume and on the production of ozone. Section 5 describes results obtained when results of these plume studies were incorporated into the CSIRO 2-D chemical transport model, using both of the parameterizations described in Section 3.

2 PLUME MODEL

The plume model used in the present studies is based on the Gaussian plume model of Melo et al. (1978). The plume is represented as a set of expanding concentric elliptical annuli, with dimensions based on analytical solutions of the diffusion equation for a Gaussian profile (Konopka, 1995). Diffusion coefficients are from Durbeck and Gerz (1995). The vortex and dispersion phases of the aircraft plume are modelled for times up to approximately 24 hours after emission. The tropospheric

---

[*] *Corresponding author:* Ian Plumb, CSIRO Telecommunications and Industrial Physics, Lindfield, NSW 2070, Australia. Email: Ian.Plumb@csiro.au

chemistry reaction scheme contains 110 species and approximately 400 reactions with rate coefficients from Sander et al. (2000) and Atkinson et al. (1999).

2.1 *Composition of background atmosphere*

Conversion of aircraft exhaust products is dependent on the composition of the background atmosphere. Sensitivity of the results to the background atmosphere was studied using atmospheric compositions from the SONEX campaign. A base case reference atmosphere consisting of the background case in Table 2 of Jaegle et al. (2000) was used, in addition to other air masses identified during the SONEX campaign. In addition, a global climatology was derived, based on a number of measurement campaigns, together with ozone, temperature and water vapour climatologies from the literature.

3 PARAMETERIZATIONS OF PLUME PROCESSING

In an assessment model, the emissions from all aircraft trajectories within each model grid cell over a given period of time are averaged and represented as a time-varying emission rate for each emitted species. What is required from a plume parameterization is a modification to the emissions (or a set of effective emissions), which takes into account the chemistry in the expanding plume. There have been two proposals on how this should be done.

The first (Kraabol et al., 2000a; Meijer, 2001) uses the plume model to calculate the chemical composition of the plume when the plume has expanded to dimensions corresponding rougly to a model grid cell. Emission conversion factors *ECF* are defined for each species X which is emitted or produced in the plume

$$ECF_X(t) = \frac{\mathrm{X}(t) - \mathrm{X}_a(t)}{\mathrm{NOy}(t) - \mathrm{NOy}_a(t)} \qquad (1)$$

where subscript *a* denotes ambient concentration into which the emission occurs.

The second approach (Petry et al., 1998) compares the composition of the plume after it has expanded to the dimensions of a model grid cell with a calculation in which aircraft emissions are diluted at time of emission into the same volume as occupied by the plume at the end of the integration. This “instantaneous dispersion” calculation is taken to represent the multi-dimensional model without plume corrections. The difference between these two calculations is used to calculate a set of effective emission indices to use in the multi-dimensional model. For each species X emitted or produced in the plume, a correction $d(\mathrm{X})$ is calculated which must be added to the concentration change $\Delta(\mathrm{X})$ produced by instantaneous dispersion. The relative emission change for X is then given by

$$d_{rel}(\mathrm{X}) = \frac{d(\mathrm{X})}{\Delta(\mathrm{NOx})} \qquad (2)$$

These relative emission changes can be used to define effective emission indices for each species X

$$EI_{eff}(\mathrm{X}) = \frac{m_X}{m_{NOx}} d_{rel}(\mathrm{X})\, EI(\mathrm{NOx}) \qquad (3)$$

These two approaches for including the effects of plume processes in multi-dimensional models are fundamentally quite different and there has been little discussion in the literature as to their relative merits. Both *ECF*s and d_{rel} values have been calculated in the present study and used in the 2-D model studies in Section 5.

4 RESULTS OF PLUME MODEL STUDIES

4.1 *Dependence on dynamical variables*

Dynamical variables affect the plume chemistry primarily through determining the cross-sectional area of the plume as a function of time. The evolution of the plume area can be changed either by changing the diffusion coefficients or by changing the wind shear. Wind shear results in stretching of the plume along its major axis, but little change in the dimension along the minor axis. Changing the wind shear from 0 to 0.01 s^{-1} results in a change in the cross-sectional area of the plume after 24 hours from 5.6×10^6 m^2 to 1.7×10^8 m^2, or approximately a factor of 30. Figure 1 shows relative emission changes for NOy species and for ozone as functions of wind shear for the background atmosphere. All relative emission changes tend to zero as the wind shear is increased (although not monotonically in all cases). This is to be expected, as the simulation approaches the instantaneous dispersion case. On the other hand, emission conversion factors (not shown) approach limiting values which are non-zero.

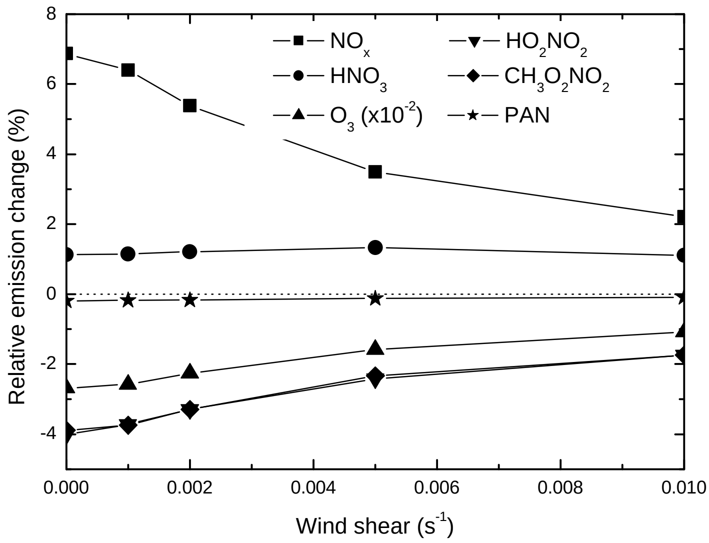

Figure 1. Relative emission changes (as percentages) as functions of wind shear for the base case.

Table 1. Important characteristics of different air masses used to study the influence of background atmosphere on plume processes.

Parameter	Background Influence	Stratospheric marine	Tropical marine	Midlatitude	Continental	Cirrus
Temperature (K)	227	223	225	231	223	231
H2O (µmol mol^{-1})	120	42	195	208	128	338
O3 (nmol mol^{-1})	55	149	33	47	55	50
NOx (pmol mol^{-1})	93	135	60	68	593	83
HOx (pmol mol^{-1})	3.8	1.8	4.8	4.8	0.98	5.2
Aerosol SA (μm^2 cm^{-3})	7.8	8.1	4.4	10	11.4	27.8

4.2 *Dependence on composition of background atmosphere*

Calculations were performed to determine the effect of composition of the background atmosphere on plume processing. The air masses considered are those identified in the SONEX campaign (Jaegle et al., 2000) and the important differences between the different air masses are summarized in Table 1.

Figure 2 shows emission conversion factors for NOx in the plume after 24 hours for the different air masses. There are clearly significant differences in the fractions of NOx remaining for the different background air masses. The continental air mass has the smallest conversion of NOx to products, while the stratospheric influence air mass has the largest.

Another notable feature of Figure 2 is the comparatively small variation in the amount of NOx remaining with time of day of the emissions. Other authors have reported larger variations (Karol et al., 2000; Kraabol et al., 2000a; Meijer, 2001). The reason for this can be understood by reference to Figure 3. This diagram shows the fraction of the initial NOy remaining as NOx as a function of time after emission for different emission times for the background atmosphere. For all times other than 24 hours after emission, there are much larger differences between the NOx for different emission times. This is because there are two main conversion routes for NOx: the daytime, which is dominated by reactions of NO_2 with OH and HO_2, and the night time, which is dominated by conversion to N_2O_5 and ultimately to HNO_3 via heterogeneous chemistry. As can be seen in Figure 3, conversion is more rapid during the day. As long as a 24-hour integration is used, the same total lengths of daytime are seen for all emission times, and similarly for night time.

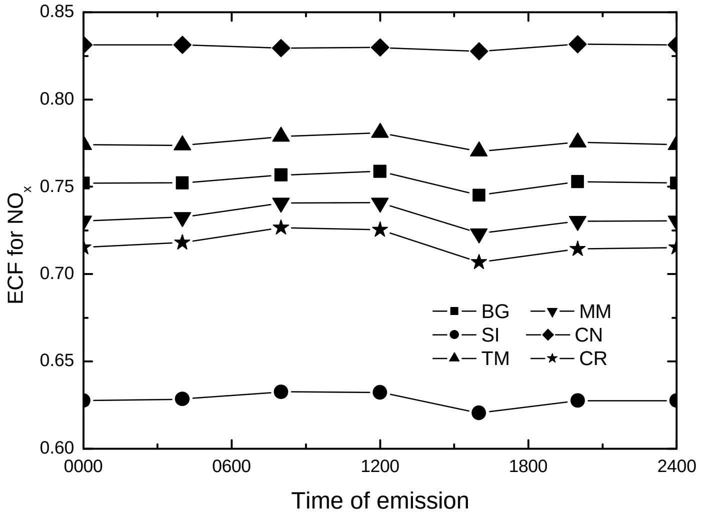

Figure 2. Emission conversion factors for NOx 24 hours after emission as functions of emission time for different air masses (BG = background, SI = stratospheric influence, TM = tropical marine convection, MM = mid-latitude marine convection, CN = continental convection and CR = cirrus cloud), for 1 November.

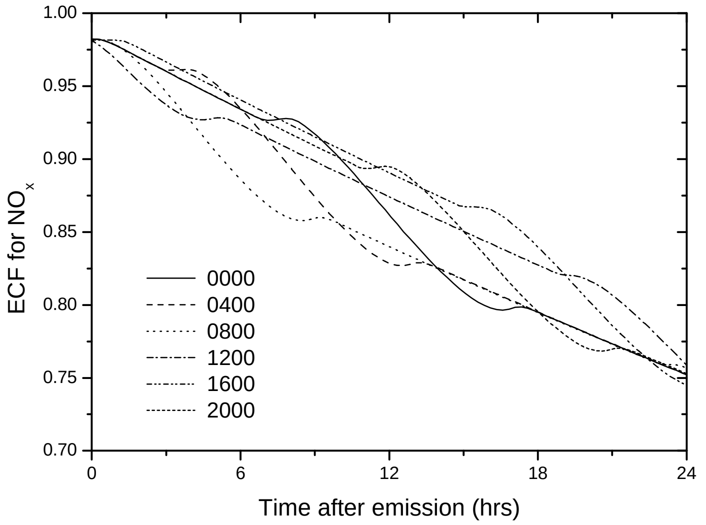

Figure 3. Emission conversion factors for NOx as functions of time after emission and emission time for background atmosphere, for 1 November.

The differences in conversion of NOx shown in Figure 2 can be explained in terms of differences in NOx, HOx and O_3 in the background atmospheres. For the air of stratospheric origin, the higher O_3 content means greater conversion to N_2O_5 at night, which more than compensates for the comparatively low HOx in this air mass. For the continental convection air mass, the high background NOx results in suppression of HOx and other peroxy radicals, so that formation of HO_2NO_2, $CH_3O_2NO_2$ and PAN are all reduced.

4.3 *Dependence on location and time of year of emissions*

Studies were made of the dependence of conversion of aircraft exhaust products on latitude, altitude and time of year. As an example, Figure 4 shows ECFs for NOy components as functions of altitude at 40°N, 1 October. As can be seen in Figure 4, there is a marked decrease in conversion of NOx to NOy with increasing altitude. At high altitudes, N_2O_5 and HNO_3 become the major products, due to increasing O_3 with altitude. At lower altitudes, HO_2NO_2, $CH_3O_2NO_2$ and PAN become significant, with PAN the largest product at 8 km.

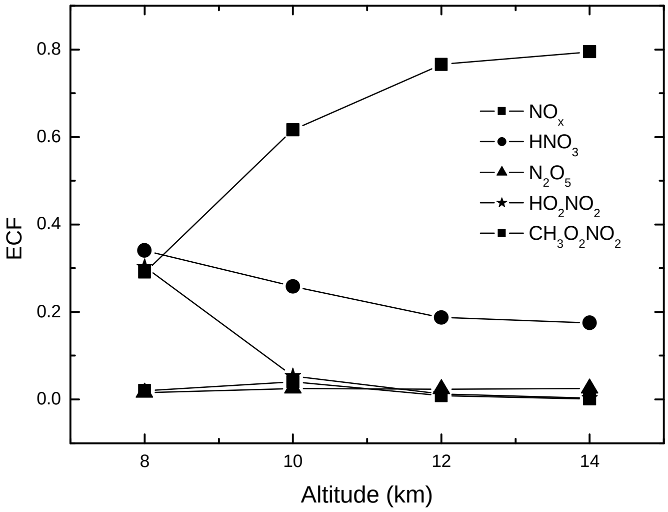

Figure 4. Emission conversion factors for NOy species 24 hours after emission as functions of altitude for 8 am emission time, for 1 October.

5 2-D MODEL CALCULATIONS

A first-order estimate of the importance of plume processes on aircraft assessment studies for the current subsonic aircraft fleet was made using the CSIRO 2-D CTM. This was done by comparing aircraft impact calculations without inclusion of plume processes with calculations made using either emission conversion factors or relative emission changes derived using the plume model. Several simplifying assumptions were made in the plume parameterizations. The plume parameters were derived for a single aircraft type (B747-400), using fixed dynamical variables, and using 24-hour-average mid-latitude plume corrections at all latitudes in the northern hemisphere.

For both plume parameterizations, the calculated annual-average NH mid-latitude subsonic aircraft perturbation changed by less than 3% when plume effects were included. This is much smaller than changes of 15-18% reported in a recent 3-D study of Kraabol et al. (Kraabøl et al., 2002) but more comparable to changes reported by Meijer (Meijer, 2001).

6 CONCLUSIONS

Conversion of aircraft exhaust products in the expanding plume is a strong function of composition of the background atmosphere, altitude, latitude and season. Most results can be explained in terms of daytime conversion of NOx to NOy via HOx chemistry and night-time conversion via heterogeneous chemistry. Inclusion of either of the two plume parameterizations used in the present study in a global model results in changes to calculated subsonic impact at northern mid latitudes of less than 3%.

REFERENCES

Atkinson, R. et al., 1999: Evaluated kinetic and photochemical data for atmospheric chemistry, organic species: Supplement VII, *J. Phys. Chem. Ref. Data*, *28*, 191-393.

Danilin, M. Y. et al., 1994: Evolution of the concentrations of trace species in an aircraft plume: Trajectory study, *J. Geophys. Res.*, *99*, 18951-18972.

Durbeck, T. and T. Gerz, 1995: Large-eddy simulation of aircraft exhaust plumes in the free atmosphere: effective diffusivities and cross-sections, *Geophys. Res. Lett.*, *22*, 3203-3206.

Jaegle, L. et al., 2000: Photochemistry of HOx in the upper troposphere at northern midlatitudes, *J. Geophys. Res.*, *105*, 3877-3892.

Karol, I. L. et al., 2000: Plume transformation index (PTI) of the subsonic aircraft exhausts and their dependence on the external conditions, *Geophys. Res. Lett.*, *27*, 373-376.

Konopka, P., 1995: Analytical Gaussian solutions for anisotropic diffusion in a linear shear flow, *J. Non-Equilib. Thermodyn.*, *20*, 78-91.

Kraabøl, A. G. et al., 2002: Impacts of NOx emissions from subsonic aircraft in a global three-dimensional chemistry chemistry transport model including plume processes, *J. Geophys. Res.*, *107*, doi:10.1029/2001JD001019.

Kraabol, A. G., F. Flatoy, and F. Stordal, 2000a: Impact of NOx emissions from subsonic aircraft: Inclusion of plume processes in a three-dimensional model covering Europe, North America, and the North Atlantic, *J. Geophys. Res.*, *105*, 3573-3581.

Kraabol, A. G. et al., 2000b: Modelling chemistry in aircraft plumes 1: comparison with observations and evaluation of a layered approach, *Atmos. Environ.*, *34*, 3939-3950.

Kraabol, A. G. and F. Stordal, 2000: Modelling chemistry in aircraft plumes 2: the chemical conversion of NOx to reservoir species under different conditions, *Atmos. Environ.*, *34*, 3951-3962.

Meijer, E. W., 2001: Modelling the Impact of Subsonic Aviation on the Composition of the Atmosphere, thesis, Technische Universiteit Eindhoven, Eindhoven.

Meijer, E. W. et al., 1997: The effects of the conversion of nitrogen oxides in aircraft exhaust plumes in global models, *Geophys. Res. Lett.*, *24*, 3013-3016.

Melo, O. T., M. A. Lusis, and R. D. S. Stevens, 1978: Mathematical modelling of dispersion and chemical reactions in a plume - oxidation of NO to NO_2 in the plume of a power plant, *Atmos. Environ.*, *12*, 1231-1234.

Moulik, J. B. and J. B. Milford, 1999: Factors influencing ozone chemistry in subsonic aircraft plumes, *Atmos. Environ.*, *33*, 869-880.

Petry, H. et al., 1998: Chemical conversion of subsonic aircraft emissions in the dispersing plume: Calculation of effective emission indices, *J. Geophys. Res.*, *103*, 5759-5772.

Sander, S. P. et al., 2000: Chemical Kinetics and Photochemical Data for Use in Stratospheric Modeling Supplement to Evaluation 12: Update of Key Reactions, *JPL Publication, 00-003*.

Aerosol and Gas Chemistry of Commercial Aircraft Emissions Measured in the NASA EXCAVATE Experiment

H. Boudries*, J. Wormhoudt, D. Worsnop , M. Canagaratna, T. Onasch, R. Miake-Lye
Aerodyne Research, Inc., Billerica, Massachusetts, USA

B. Anderson
NASA Langley Research Center, Hampton VA, USA

Keywords: PM1.0, Aircraft aerosol composition, Size distribution, HONO, organics, sulfates.

ABSTRACT**:** Results from ground-based measurements carried out in January of 2002 as part of the EXCAVATE (EXperiment to Characterize Aircraft Volatile Aerosol and Trace species Emissions) field campaign at NASA Langley Research Center (Hampton, Virginia, USA) of exhaust components emitted by a Boeing 757 aircraft with a Rolls-Royce turbo engine RB-211 are presented. During the EXCAVATE experiment, all measurements were made in-situ and in real time. The non-refractory PM1.0 chemical composition and size distribution were measured by an Aerodyne Aerosol Mass Spectrometer (AMS) and the gaseous constituents such as HONO (nitrous acid) and SO_2 (sulfur dioxide) by a Tunable Infrared Laser Differential Adsorption Spectrometer (TILDAS). During these measurements, the aerosol chemical compositions and size distributions for different engine thrust levels (varying from idle to 1.5 EPR (Engine Pressure Ratio)), fuels with three sulfur contents (810, 1050 and 1820 ppmv), and four different sampling distances behind the engine (1, 10, 25 and 35 meters) were characterized. The HONO concentration was found to increase with engine power by over an order of magnitude. Total particulate organics and sulfates were found in a range 1-45 $\mu g\ m^{-3}$, and 0.1-7 $\mu g\ m^{-3}$, respectively. During the start up of the engine (increase of engine power from 1.03 (idle) to 1.15EPR, and during the shift-down of the power from 1.5 to 1.03EPR, significant increases in particulate organics were observed and were found to be 3 to 5 orders of magnitude larger than those measured for engine powers between 1.15 and 1.5 EPR. The size distribution analysis shows the presence of externally mixed aerosols composed of organics and sulfates and a clear increase in the average size distribution between 30 nm and 300 nm when sampled further downstream from the engine.

1 INTRODUCTION

During the EXCAVATE (EXperiment to Characterize Aircraft Volatile Aerosol and Trace species Emissions) experiment, a series of experimental measurements were conducted in-situ and in real-time to characterize the gas and particle chemical composition and size distribution of major and trace chemical components present in the exhaust of a Boeing 757 equipped with a Rolls-Royce RB-211 engine. A Tunable Infrared Laser Differential Adsorption Spectrometer (TILDAS) was used to measure SO_2, SO_3, HONO and CO_2, while an Aerodyne Aerosol Mass Spectrometer (AMS) was used to measure the particle chemical composition and size distribution of non-refractory PM1.0. In this paper, the mass and size distributions of total particulate organics, particulate sulfates and the concentration of gas phase HONO will be reported and discussed for engine in steady condition.

2 SAMPLING AND ANALYSES

The exhaust gas and particles from the Rolles-Royce RB-211-535E4 engine were sampled through a sampling probe especially built for the EXCAVATE experiment by NASA Langley Research

---

[*] *Corresponding author:* Boudries, Hacene, Aerodyne Research, Inc., Billerica, Massachusetts, 01821-3976 USA. Email: hboudries@aerodyne.com

Center. Detailed information about the probe used during this experiment is documented in Anderson et al. (this issue). Table 1 summarizes the conditions of engine thrust, fuel sulfur content and sampling distance behind the jet engine used during EXCAVATE. As shown in Table 1, exhausts from three different fuel sulfur contents (FSC) were tested (low sulfate fuel 810 ppmv, intermediate 1050 ppmv and high sulfate fuel 1820 ppmv), five-engine thrust levels measured in Engine Pressure Ratio (EPR), (1.03 (Idle), 1.15, 1.3, 1.4, 1.5 EPR), and four sampling distances (1, 10, 25 and 35 meters) behind the Rolls-Royce RB-211 jet engine were used during this experiment. The exhaust aerosols PM1.0 emitted by the engine were sampled and immediately diluted using pure nitrogen and then sent to the AMS through a 20 m long and 1.27 cm internal diameter stainless steel tube at a flow rate of about 10 L min^{-1}.

Table 1: Aerosol and gas sampling conducted during EXCAVATE experiment. The fuel sulfur content used are 810, 1050 and 1820 ppmv and symbolized by +, x and o, respectively.

Probe Engine power	1 m	10 m	25 m	35 m
1.03	+ x o	+ x o	x o	+ x o
1.15	x o	+ x o	x o	+ x o
1.3	+ x o	+ x o	x o	+ x o
1.4	x o	+ x o	x o	+ x o
1.5	x o		x o	

2.1 Aerodyne Aerosol Mass Spectrometer

Ambient aerosols are sampled into a vacuum and focused in an aerodynamic lens. The focused particle beam exiting the lens is directed into the particle-sizing chamber maintained at a pressure of 10^{-5} Torr. By modulating the particle beam with a chopper and using the time-of-flight of particles between the chopper and the detector, the particle velocity and the aerodynamic diameter can be obtained. The particle detection scheme consists of an oven that is coupled to a quadrupole mass spectrometer. When the particles hit the oven surface, the volatile and semi-volatile components of particles are flash vaporized. The vaporization plume is ionized by an electron impact ionizer mounted at the entrance of a quadrupole mass spectrometer, operated at 70eV electron energy and scanned in a range of 1-300 atomic mass units. Detailed information about the Aerosol Mass Spectrometer is well documented in Jayne et al. (2000).

2.2 Tunable Infrared Differential Adsorption Spectrometer (TILDAS)

Ambient gaseous species were sampled and analyzed in real time by the TILDAS instrument. The laser diodes and infrared detectors used in the TILDAS measurement are all contained in a single liquid nitrogen dewar. Data acquisition and analysis software on the TILDAS computer collects and averages absorption scans and can least-squares fit them to model spectra to derive real-time outputs of multiple species concentrations. However, most data were saved as averaged spectra for post-test analysis. Detailed information about the TILDAS and sampling configuration is documented in Boudries et al., (2004).

3 RESULTS AND DISCUSSION

3.1 Aerosol chemical composition and size distributions

Figure 1 illustrates a typical temporal trend of organics' and sulfates' mass loadings measured for five different engine power settings (1.03, 1.15, 1.3, 1.4 EPR) and two sampling probe distances (1 and 25 meters) and FSC of 1050 ppmv of sulfure. Significant increases in organic mass loadings were observed during start-up, when the engine thrust was increased from 1.03 to 1.15 EPR, and also during the power downshift from 1.5 to 1.03 EPR. These transient periods are associated with high emissions of particulates, 3 to 5 orders of magnitude higher than the concentrations measured during engine powers from 1.15 to 1.5 EPR. These transients are shown off-scale at 11:35, 11:50 and 12:45 in Figure 1. Detailed analysis of these transient periods will be presented in detail in Boudries et al. (2004) and will not be discussed further here.

During steady engine conditions, the particulate organic and sulfate mass loadings were found to be in a range 1-45 µg m^{-3}, and 0.1 – 7 µg m^{-3} respectively. As presented in Figure 1, a significant increase in organics and sulfate mass loadings was observed when sampling was switched between 1 and 25 meters. For instance, at an engine power of 1.3 EPR, the organics concentrations increased from 4 to 40 µg m^{-3}. During the same period, sulfate particles also exhibited similar behavior, increasing from 0.5 to 3 µg m^{-3}. The increase in concentration between 1 and 25 meters may be explained by the condensation of gas-phase pollutants on pre-existing aerosols occurring downstream of the exhaust plume. If this hypothesis is true, we would expect to see an increase in the mean particle size further downstream in the engine exhaust. Figure 2 shows the average size distribution of organics and sulfate for engine powers 1.3, 1.4, and 1.5 EPR measured at 1 and 25 m. This figure shows that the size distribution shifts to larger sizes when sampled further downstream in the engine exhaust. This shift in size distribution confirms the presence of particle growth. Organics and sulfate have similar aerodynamic diameters of about 40 nm when measured at 1 m behind the engine and increase when measured further downstream. The increase in the aerodynamic diameter of organic aerosols is found to be more pronounced than that of sulfate particles. For organics, the aerodynamic diameters increase from 40 to 300 nm, and for sulfate from 40 to 65 nm. The different growth behavior of the sulfate and organic containing particles suggests that they are externally mixed.

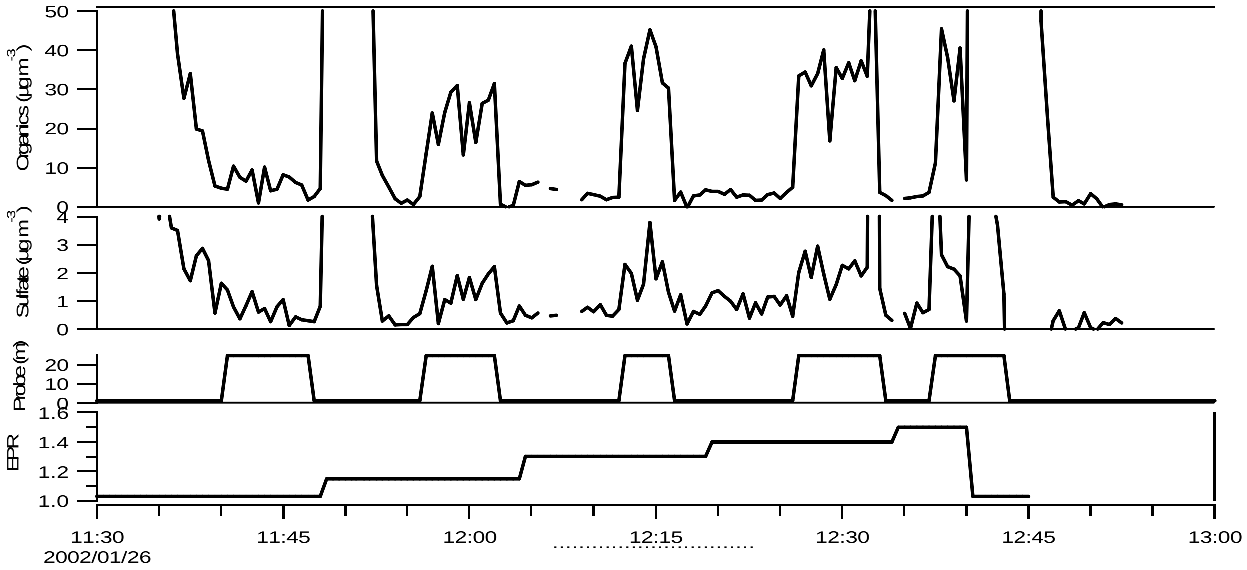

Figure 1: Time-series of total particulate organics and sulfates measures during EXCAVATE experiment.

3.2. Particle emission indices

The emission indices (EI) of sulfate and organics have been calculated for all engine power settings, fuel sulfur content and sampling distances behind the engine exhaust plume. All EI are normalized to CO_2 to account for dilution effect. Figure 3 shows the variation of EI for sulfate and organics as a function of engine power. Only EI measured at 25 m are represented here. The results show that the EI of organics increases with engine power. At high engine power (1.5 EPR), the organic EI is 0.04 g kg^{-1} of fuel, while at idle (1.03 EPR) the average EI is about 0.018 g kg^{-1} of fuel. It is also important to note that the EI of organics as a function of engine power is found to be independent of fuel sulfur content. The emission indices of sulfate appear to be independent of engine power settings, and proportional to the fuel sulfur content. The highest EI correspond to the highest sulfur fuel content. For fuel sulfur content of 1050 ppm and 1820 ppm, the average EI values of sulfate are found to be 0.0013 and 0.0023 g kg^{-1} of fuel, respectively.

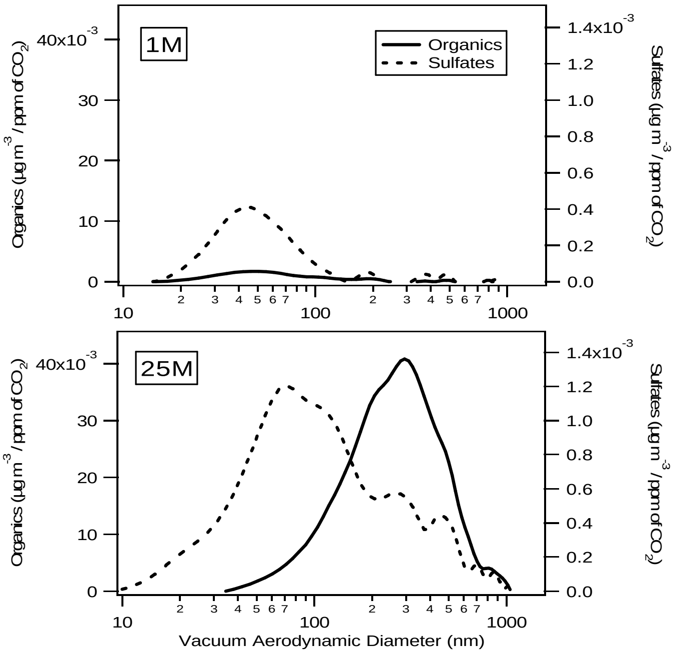

Figure 2: Variation of avarage aerodynamic diameter of sulfate and organics at 1 and 10 M for engine power of 1.3, 1.4, and 1.5 EPR.

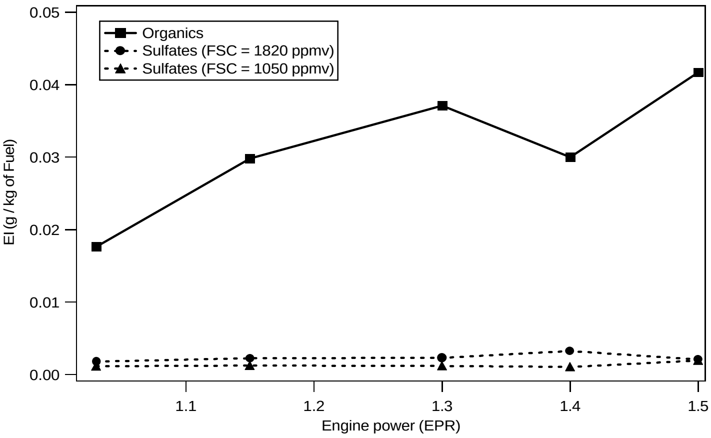

Figure 3: Average emission indices versus engine power measured 25 M behind the Engine.

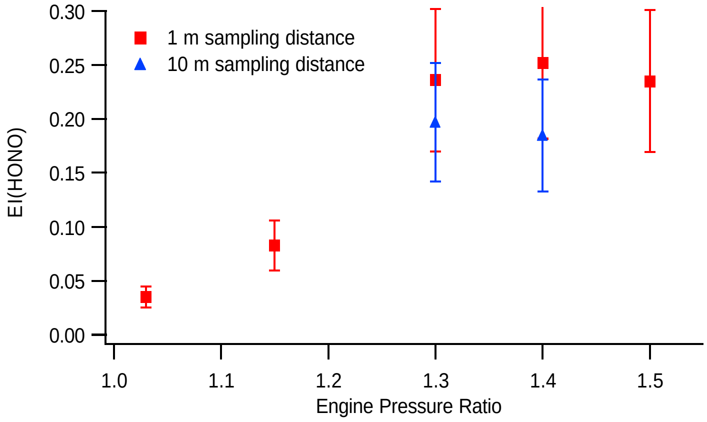

Figure 4: HONO emission indices in g/kg of Fuel measured at 1 m and 10 m behind the engine.

3.3 HONO measurement

During EXCAVATE experiment the detection limit for HONO was as low as 100 ppbv in the multipass cell of the TILDAS instrument. At high power (1.3 to 1.5 EPR), over 2 ppmv of HONO was observed. When converted to emission indices, the B757 HONO results shown in Figure 4 shows a clear power dependence, decreasing with decreasing power at the two lower settings but roughly constant at the highest three settings. These results are also consistent with the particulate organics emission already reported above. When the sampling point was moved back to 10 m behind the engine, the HONO concentration may have decreased somewhat, though when the total error estimates shown in Figure 4 are taken into account, this decrease is not necessarily significant. Results of SO_2 measured by the TDL instrument at 1m and 10m behind the engine showed good agreement with the total fuel sulfur. At 1m, the ratios of sulfur in SO_2 to total fuel sulfur lie in the range 0.75 to 1.0, while at 10 m they are distributed evenly above and below at ratio of 1.

4 CONCLUSION

During the EXCAVATE experiment, particulate and gaseous emissions from a Boeing 757 equipped with a RB-211 Rolls Royce engine were studied. Chemical composition and size distribution of PM1.0 were measured in real time with a resolution of 30 seconds. Time series profiles of total particulate organics were found in a range 1 to 45 µg m^{-3} and 0.1 to 7 µg m^{-3}, respectively when measured between 1 and 35 m behind the engine exit plume. Both particulate organics and sulfate show a clear increase of total mass loading when measured further downstream in the engine exhaust. Sulfate emission indices were found to be dependent on fuel sulfur content, and to be positively correlated to the sampling probe distance. Organics emissions are also found positively correlated with sampling distance but independent of sulfur fuel content. Gas phase HONO was found in the exhaust at concentrations above 2 ppmv. Similar to particulate organics and sulfate, the HONO emission index increases with increasing power. The average size distribution showed that sulfates and organics exhibit the same average vacuum aerodynamic diameter of 40 nm and increase to larger sizes when measured further downstream from the engine. The presence of two distinct average aerodynamic diameters for sulfate and organics measured further downstream in the exhaust suggests that they are externally mixed.

ACKNOWLEDGMENTS

This work was supported by the engine emissions characterization element of the UEET program through NASA Glenn Research Center.

REFERENCES

Boudries H., et al., Real time characterization of aircraft particulate and gas emissions during Excavate 2002. *In preparation.*

Anderson B.E., et al., Overview of results from the NASA experiment to characterize aircraft volatile aerosol and trace species emissions (EXCAVATE). *This issue*.

Jayne J., et al., Development of an Aerosol Mass spectrometer for size and composition analysis of submicron particles. *Aerosol Science and Technology 33, 49-70, 2000.*

Emission of Volatile and Non-Volatile Ultrafine Particles from a Combustion Source During PartEmis

M. Fiebig*, L. Fritzsche, C. Stein, A. Petzold
Institut für Physik der Atmosphäre, Deutsches Zentrum für Luft- und Raumfahrt Oberpfaffenhofen, Germany
S. Nyeki
Paul-Scherrer Institut, Villigen, Switzerland

Keywords: PartEmis, particulate jet-engine emissions, aerosol data inversion, ultrafine particles

ABSTRACT: During the PartEmis experiment, aerosol properties and precursor gas concentrations were measured in the exhaust of a jet engine combustion chamber. The particle size distribution in the ultra-fine range was investigated using a cascade of condensation particle counters together with a differential mobility analyser. To extract the full information from the data, a novel data inversion algorithm was developed and applied to the PartEmis data. The measured particle size distribution exhibited two modi centred at ~10 and ~30 nm consisting of carbonaceous combustion particles. An additional mode of secondary volatile particles with diameters < 10 nm was present at high fuel sulphur content.

1 INTRODUCTION

The PartEmis experiment was designed to improve the knowledge about the properties and formation processes of carbonaceous and volatile aerosol particles formed in jet engine combustion chambers as a function of the operating conditions and the fuel sulphur content (FSC). To this end, aerosol properties and precursor gas concentrations were measured simultaneously at the exit of a jet engine combustion chamber on a test rig. This work focuses on the ultra-fine fraction of the aerosol with particle diameters between 3 and 20 nm.

2 GENERAL PROPERTIES OF COMBUSTION AEROSOL PRODUCED BY JET ENGINES

The aerosol emitted by a jet engine combustion chamber consists on the one hand of carbonaceous, non-volatile combustion particles (CCP). These are formed by incomplete combustion and typically larger than 10 nm in particle diameter. Their size distribution exhibits two distinct maxima which are centred at approximately 10 nm and 30 nm particle diameter.

The other dominating particle species in jet engine combustion aerosol are volatile condensation particles. They are formed by nucleation from gaseous precursors, primarily sulphuric acid, and have particle diameters smaller than 10 nm. Also, combustion particles may be coated with volatile material. Figure 1 shows the described particle size distribution of CCP and volatile particles.

Figure 2 illustrates the state of mixture of CCP and volatile particles. When precursor species condense, they first form a coating on the surface of the CCP. If condensable precursor material is present in excess, additionally volatile particles are formed from the gas phase. This leads to an external mixture of coated CCP and volatile condensation particles.

---

* *Corresponding author:* Markus Fiebig, Institut für Physik der Atmosphäre, Deutsches Zentrum für Luft- und Raumfahrt Oberpfaffenhofen, D-82234 Wessling, Germany. Email: Markus.Fiebig@dlr.de

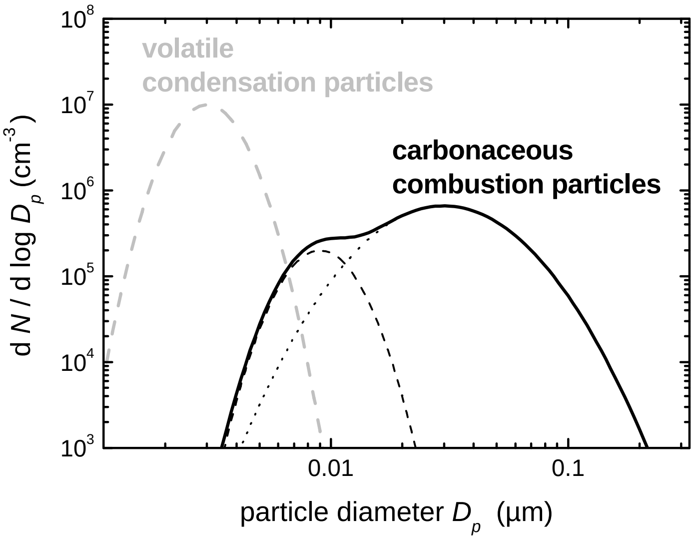

Figure 1. Exemplary size distribution of carbonaceous combustion and volatile condensation particles in jet engine combustion aerosol.

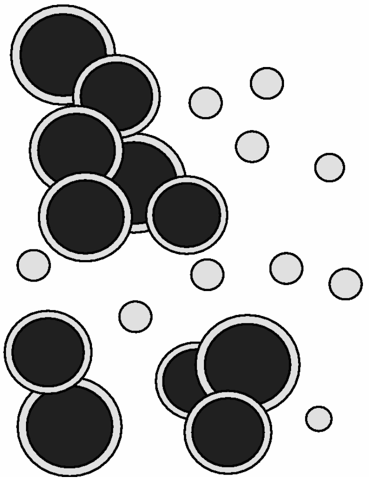

Figure 2. Sketch illustrating the state of mixture of coated carbonaceous combustion and volatile secondary particles.

FORMATION OF VOLATILE PARTICLES

The particle size distribution in the ultra-fine range was measured during PartEmis with the Condensation Particle Size Analyser (CPSA) (Stein et al., 2001). The CPSA is a cascade of 4 condensation particle counters (CPCs). A CPC measures the integral concentration of particles larger than an approximate threshold diameter. To this end, the aerosol sample is saturated with alcohol vapour and subsequently cooled to reach super-saturation with respect to the alcohol vapour. Particles larger than the threshold diameter are activated as condensation nuclei, grow by condensation of alcohol vapour onto the nuclei and are counted optically. The threshold diameter depends on the super-saturation reached in the CPC. In the CPSA, the approximate threshold diameters of the four channels are set to nominally 4, 7, 9, and 20 nm, respectively.

Figure 3 shows the data obtained with the CPSA in combustion aerosol sampled at the exit plane of a jet engine combustion chamber. By taking the differences of the particle concentrations measured by the CPSA channels, the concentrations of particles in the size ranges 4 – 7 nm, 7 – 9 nm, and 9 – 20 nm are obtained and normalised by the concentration of particles larger than 20 nm. The result in plotted in Figure 3 as function of fuel sulphur content (FSC) and operating state of the combustion chamber.

It is obvious that the contribution of particles between 7 – 9 nm and 9 – 20 nm are almost independent of the FSC. These are therefore thought to consist of CCP. Particles between 4 – 7 nm occur 20 times less frequently than CCP for low FSC, but 7 times more frequently at high FSC. These are volatile, secondary particles formed from excess gaseous sulphuric acid that was not deposited on the surface of the CCP.

3 INVERSION OF SIZE DISTRIBUTION DATA

3.1 *Inversion Method*

The threshold particle diameter at which a CPC begins to count particles is not a sharp boundary. The transfer function describes the counting efficiency of a CPC as a function of particle diameter. Figure 4 shows the measured transfer functions of the 4 CPSA channels.

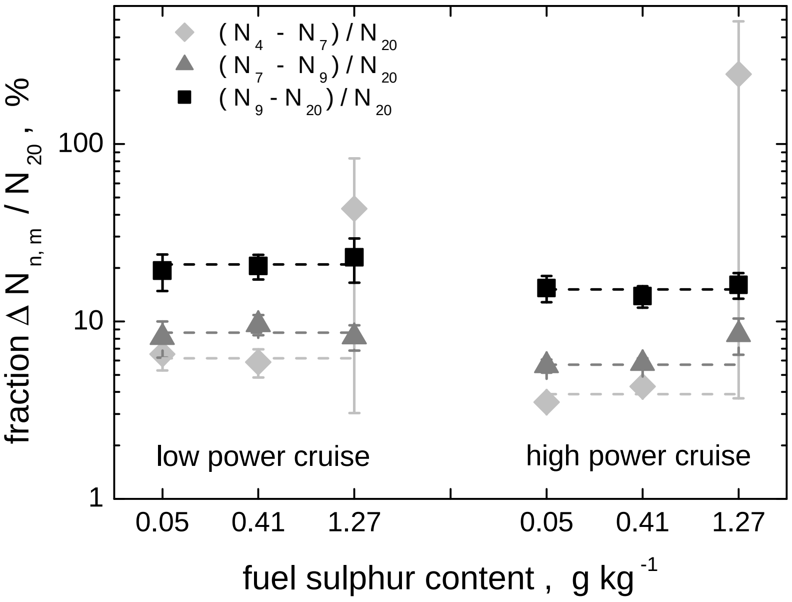

Figure 3. Concentrations of nano-particles in the size intervals measured by the CPSA, normalised to the concentration of particles larger than 20 nm, as a function of fuel sulphur content and operating state of the combustion chamber

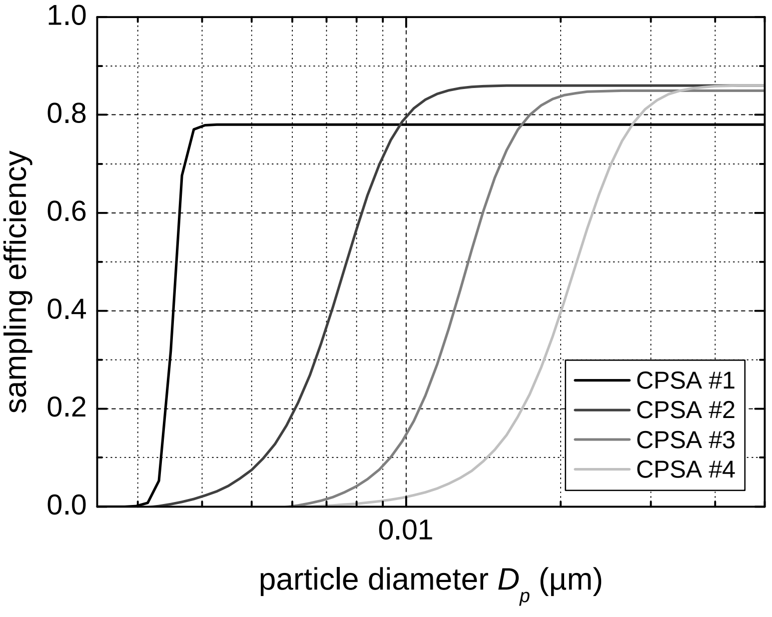

Figure 4. Measured transfer functions of the four CPSA channels for laboratory conditions.

To extract the full size distribution information from the CPSA data, a data inversion is required which is described by the equation

$$\left\| \mathbf{A}\vec{x} - \vec{b} \right\| \to 0 . \qquad (1)$$

Here, the vector $\vec{x}$ contains the discretised size distribution, the vector $\vec{b}$ the particle concentration measured by each CPSA module, and the rows of marix $\mathbf{A}$ the counting efficiency as function of particle diameter (transfer function) for each CPSA module.

Since the matrix equation is usually underdetermined, i.e. there are less measurements than points on the size distribution or less rows than columns in matrix $\mathbf{A}$, it is postulated that the resulting size distribution is smooth. The corresponding smoothing matrix is added to matrix $\mathbf{A}$.

The resulting equation is solved by the Non-Negative Linear Least-Squares Solver (NNLS) algorithm (Lawson and Hanson, 1974) requiring the solution also to be non-negative.

The transfer function of the CPSA modules depends sensitively on the temperatures of the saturation and condensation paths within the individual modules. Since the transfer functions of the CPSA were measured for a whole range of internal temperatures, it is possible to calculate the transfer functions contained in **A** based on the measured internal temperatures for each respective data-set before inverting equation (1).

3.2 *Resulting Particle Size Distributions*

To complement the CPSA measurements during PartEmis, the size distribution for particle diameters D > 20 nm was measured in high resolution by a differential mobility analyser (DMA). Figure 5 shows the obtained composite particle size distributions from CPSA and DMA data for low (50 µmol / mol) and high (1270 µmol / mol) FSC. Here, the CPSA data was evaluated in a first step by approximating the transfer functions of the CPSA modules by step functions. Already in this analysis, the CPSA detects a second mode of particles centred at ~10 nm in addition to the CCP mode measured by the DMA. Both modi are present independently of the FSC and must therefore consist of CCP. At high FSC, a third particle mode of volatile particles with D < 7 nm is present.

Figure 6 compares the result of the approximate CPSA evaluation with the respective size distribution obtained with the inversion method, both for medium (410 µmol / mol) FSC. Both methods use the high resolution DMA data to determine the position of the larger CCP mode. As obvious from Figure 6, the approximate evaluation method leads to numerical broadening of the small CCP mode and to a shift of the mode median diameter to smaller particle diameters. The inversion method extracts the whole size distribution information from the CPSA data and yields the true position, width and height of the small CCP mode at 12 nm.

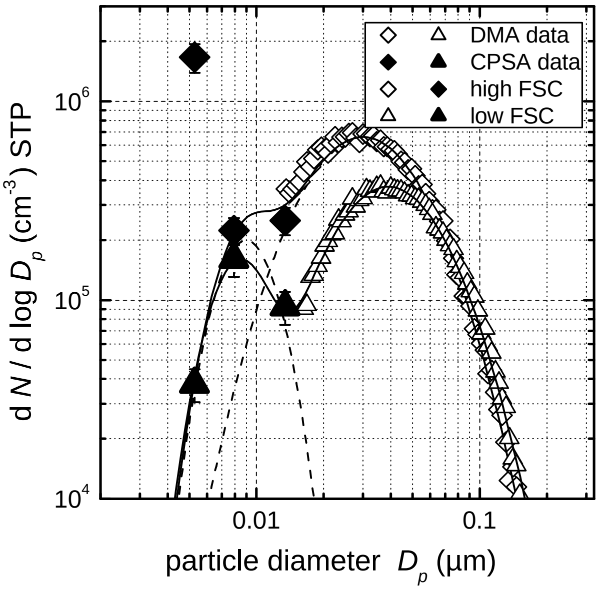

Figure 5. Ultra-fine range particle size distribution of jet engine combustor exhaust aerosol for high and low FSC. The size distributions are based on CPSA and DMA data..

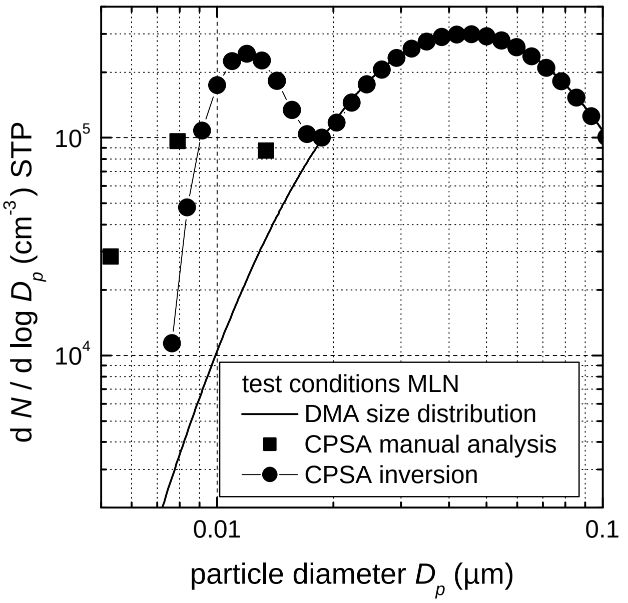

Figure 6. First results of inversion method applied to CPSA plus DMA data obtained in jet engine combustor aerosol. The size distribution obtained by data inversion is compared with the conventional analysis of the same data.

4 CONCLUSIONS

During PartEmis, the size distribution of ultra-fine particles in the range of 3 to 20 nm particle diameter was measured in the exhaust aerosol of a jet engine combustor using the CPSA. This data was augmented by measurements with a DMA for particle diameters larger than 20 nm. The size distributions measured consisted of two modi centred at ~10 and ~30 nm. Since the presence of these modi was independent of FSC, they had to consist of CCP. For high FSC, a third mode of secondary volatile particles with diameters < 10 nm was present.

To extract the full size distribution information from the CPSA data and transfer functions, an inversion algorithm was developed. The algorithm is robust and solves the inversion equation with the boundary conditions of non-negativity and smoothness of the size distribution. It takes the dependence of the CPSA transfer functions on the internal instrument temperatures into account.

REFERENCES

Lawson, C.L., and R.J. Hanson, 1974: *Solving Least Squares Problems*, Prentice-Hall, Englewood Cliffs.

Stein, C., F. Schröder, and A. Petzold, 2001: The condensation particle size analyzer: A new instrument for the measurement of ultrafine aerosol size distributions. *J. Aerosol Sci. 32*, S1, S381 – S382.

A USA commercial flight track database for upper tropospheric aircraft emission studies

Donald P. Garber, Patrick Minnis[1], and Kay P. Costulis
Atmospheric Sciences, NASA Langley Research Center, Hampton, Virginia, USA

Keywords: air traffic, flight tracks, aircraft emission, contrail simulation

ABSTRACT: A new air traffic database over the contiguous United States of America (USA) has been developed from a commercially available real-time product for 2001-2003 for all non-military flights above 25,000 ft. Both individual flight tracks and gridded spatially integrated flight legs are available. On average, approximately 24,000 high-altitude flights were recorded each day. The diurnal cycle of air traffic over the USA is characterized by a broad daytime maximum with a 0130-LT minimum and a mean day-night air traffic ratio of 2.4. Each week, the air traffic typically peaks on Thursday and drops to a low Saturday with a range of 18%. Flight density is greatest during late summer and least during winter. The database records the disruption of air traffic after the air traffic shutdown during September 2001. The dataset should be valuable for realistically simulating the atmospheric effects of aircraft in the upper troposphere.

1 INTRODUCTION

Air traffic is expected to increase globally by a factor of 5 or 6 between 1990 and 2050 with a commensurate rise in emissions and contrails that may significantly affect air quality and climate (IPCC, 1999). Some of the aircraft exhaust effects, especially those impacting contrail and cirrus clouds, are still highly uncertain requiring exhaustive research to more accurately prognosticate the climatic impact of enhanced commercial fleets. Contrail formation, growth, and dissipation and their optical properties are highly dependent on aircraft engine type, and the temperature, humidity, and wind speed and direction at flight altitude. The contrail-cirrus radiative effects, which ultimately affect the average state of the atmosphere, depend on the underlying conditions (surface temperature and albedo), the contrail optical properties, air traffic density and altitude, and the time of day when the contrails are formed. Thus, to accurately assess current air traffic effects and future flight scenarios, it is necessary to simultaneously know the meteorological state and the distribution of flights at a given location. This report addresses the latter need for the contiguous United States (CONUS) with a focus on the upper tropospheric portions of commercial flights.

The release of United States of America (USA) near-real time air traffic control information to the commercial sector during the late 1990’s made the collection of more refined flight path data much easier than before. This report documents the collection, reduction, analysis, and availability of commercial flight information taken above 25,000 ft over the CONUS since late 2000. The result of the analysis is a flight track database that can be easily accessed and used by modelers.

2 DATA AND ANALYSIS

Commercial flight information taken in real time over the USA from the FlyteTrax system (FlyteComm, Inc.) has been purchased and archived at NASA Langley Research Center since September 2000. The raw data consist of 2, 5, or 10-minute reports of flight number, aircraft type, download time, latitude, longitude, altitude, heading, destination and origination locations, speed, and departure and arrival times. All portions of flights above 25,000 ft (7.6 km) within the domain (20°N - 50°N and 60°W - 135°W) were quality controlled and sorted by flight number and time.

---

[1] *Corresponding author:* Patrick Minnis, MS 420, NASA Langley Research Center, Hampton, VA, USA 23681. Email: p.minnis@nasa.gov

Table 1: Monthly sampling statistics for flight track database.

Month	2001 (number of days)				2002 (number of days)			
	Full	Partial	Empty	% Full	Full	Partial	Empty	% Full
Jan	12	1	18	39	18	2	11	58
Feb	0	0	28	0	22	1	5	79
Mar	17	2	12	55	29	1	1	94
Apr	21	8	1	70	30	0	0	100
May	11	18	2	35	26	4	1	84
Jun	20	10	0	67	29	1	0	97
Jul	19	11	1	61	31	0	0	100
Aug	25	3	3	81	31	0	0	100
Sep	30	0	0	100	26	3	1	87
Oct	24	3	4	77	29	1	1	94
Nov	21	1	8	70	21	7	2	70
Dec	26	4	1	84	24	2	5	77

The summary statistics for each month in Table 1, which shows the number days in each month that have complete (full), partial, or no (empty) sampling, indicate that the best sampling occurred during late 2001 and 2002. No military flights are available in this database. Not all flights over Mexico and Canada are represented either. All commercial and private flights over the USA should be included for those days noted as complete.

Flights remaining after passing the quality control checks were then used to develop the database, which is divided into two parts: linear and gridded. The former computes the node points for each flight track on a 1° latitude-longitude grid using interpolation along great circle arcs between each report. These standardized flight track positions comprise the linear database in the form of one file for each day consisting of a series of flights, each with its own header describing the general flight characteristics and followed by a series of flight segments. The gridded database, provided in cell files, uses the segmented flight tracks to determine for each hour the number and total length of flights within a 1-km vertical range in a given 1° grid box. The linear dataset should be useful for detailed simulation studies, while the gridded data should be more valuable for use in climate simulations.

3 RESULTS

The main parameters of interest for this database are the number of flights and the cumulative flight length (CFL). CFL can be computed as the sum of all flight segment lengths within a given box or domain for a selected time period, usually 1 hour.

3.1 *Spatial Variability*

The 1° CFL distribution for 10 September 2001 is sliced by altitude ranges in Figure 1. The maximum CFL in a single 1° box in the lowest altitude range is only ~22,000 km over southern Michigan and northern Virginia. Most CFLs within that layer are less than 4000 km with many flights occurring in southern California, northern Florida, and the Midwestern USA. Flights at these lower levels consist of portions of longer legs near the terminals or of the apex segments of short-distance commuter flights. The maximum CFL between 9 and 11 km exceeds 40,000 km over parts of eastern Ohio and western West Virginia. In addition to the large area of heavy traffic over the northeastern USA, a relatively dense traffic lane is evident over the Atlantic coast south of New York City. These flights are generally mid-range or longer flights. The maxima over the western USA are found over Nevada and the border between New Mexico and Arizona away from the large hubs at San Francisco and Los Angeles. The CFLs at the highest altitudes (Figure 1c), generally consisting of long distance flights, are greatest over Lake Erie, the central Great Plains, southern Utah, and coastal north Florida. The combined levels in Figure 1d yield a large number of regions with total CFL > 40,000 km. These include much of the northeastern USA exclusive of New England, the Atlantic coast, central Great Plains, the Southwest, and lower Mississippi Valley. The few CONUS areas with total CFL < 4,000 km are found along the western Canadian and central Mexican borders.

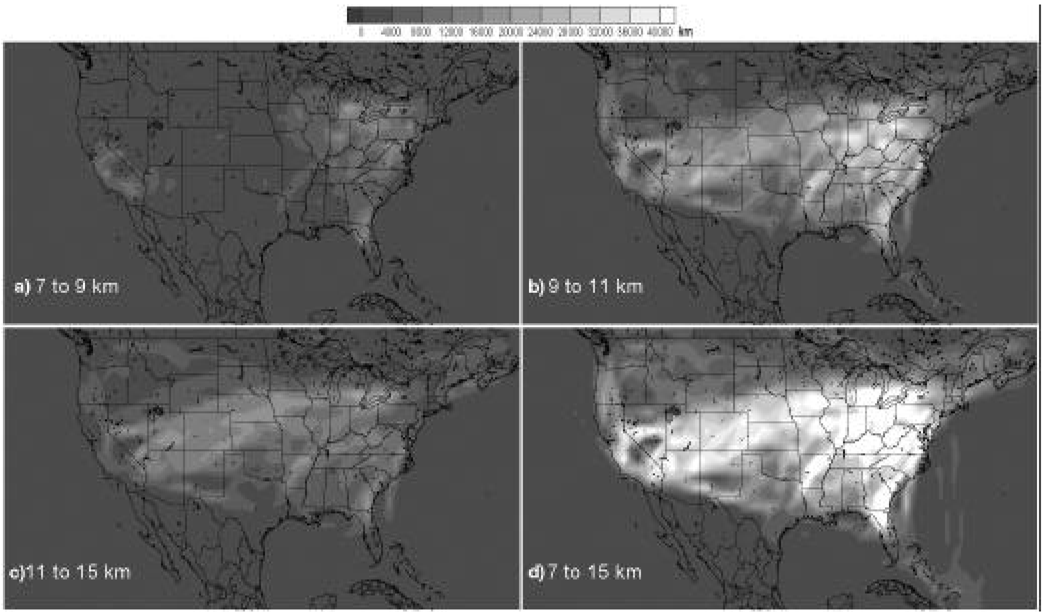

Figure 1. Cumulative flight lengths for 1° regions, 10 September 2001.

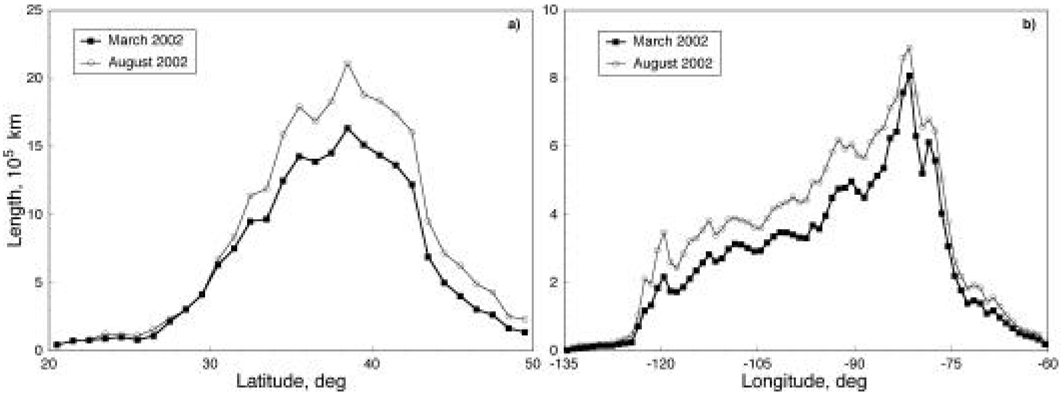

Figure 2. Mean daily cumulative flights lengths as a function of (a) latitude and (b) longitude over USA.

The latitudinal and longitudinal variations of the mean daily CFLs are summarized in Figure 2. Peak traffic occurs between 38°N and 39°N with a secondary maximum around 35.5°N (Figure 2a). A relative maximum (Figure 2b) at 120°W corresponds to the southern California traffic followed in the eastward direction by a dip and a relatively steady increase to the overall maximum at 81.5°W. The traffic then tails off to 30,000 km at 60°W. More flights are evident over the Atlantic than over the Pacific. The shapes of the longitudinal and zonal mean CFL curves are very similar for both March and August suggesting more of a general increase in traffic during summer than a changing of the air traffic patterns. The maximum CFL for the entire domain occurs between 10 and 11 km followed by the layer between 11 and 12 km (Figure 3). The March-August increase in air traffic is greatest between 10 and 11 km. The total daily CFLs for the domain are 19.6 and 25.1 million km during March and August, respectively.

3.2 *Temporal Variability*

The diurnal cycle over the entire domain is summarized in Figure 4 using monthly means from March and August 2002. The variation with in Figure 4a shows a rapid increase in flights after 1100 UTC to a peak around 1830 UTC during March with a secondary maximum around 2330 UTC. The minimum occurs near 0730 UTC. During August, the air traffic begins in earnest an hour earlier than during March because of a shift to daylight savings time. The maximum during August occurs at 2230 UTC. Overall, the air traffic during August is ~28% greater than during March. The diurnal variation of air traffic shows no seasonal shift in local time (LT) with the daily cycle beginning in earnest after 0500 LT, reaching two maxima at 0930 and 1230 LT with a minimum at 0130 LT (Figure 4b). Considering the hours 0600 – 1800 LT as daytime and the remaining hours as night, a rough estimate of the day-night ratio in cumulative flight length is 2.5 and 2.3, respectively, during March and August 2002. The true day-night ratio, valuable for calculating the relative shortwave and longwave radiative forcing by contrails, is more accurately determined for each month by considering the actual hours of daylight for each location and month. Such information can be easily computed from the gridded database. The plots begin at 0400 UTC because it corresponds to local midnight in the easternmost portion of the domain.

The number of CONUS flights has a distinct weekly cycle. The mean air traffic minimum occurs on Saturday following a peak of 25,500 takeoffs and landings on Thursday. The range in the number of flights per day of week is typically around 5,000 except for the extreme minima occurring during certain holidays or as a result of the air traffic shutdown period after September 11, 2001. The weekly range in the average daily number of flights is 18%.

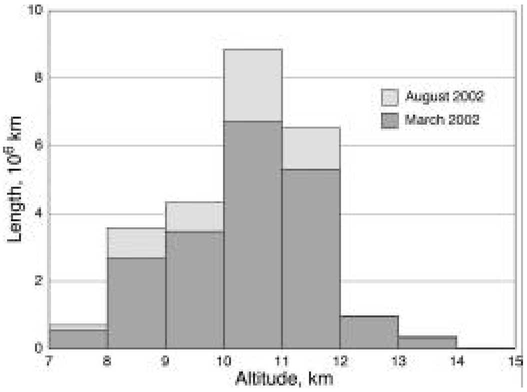

Figure 3. Mean daily layer CFL over USA domain.

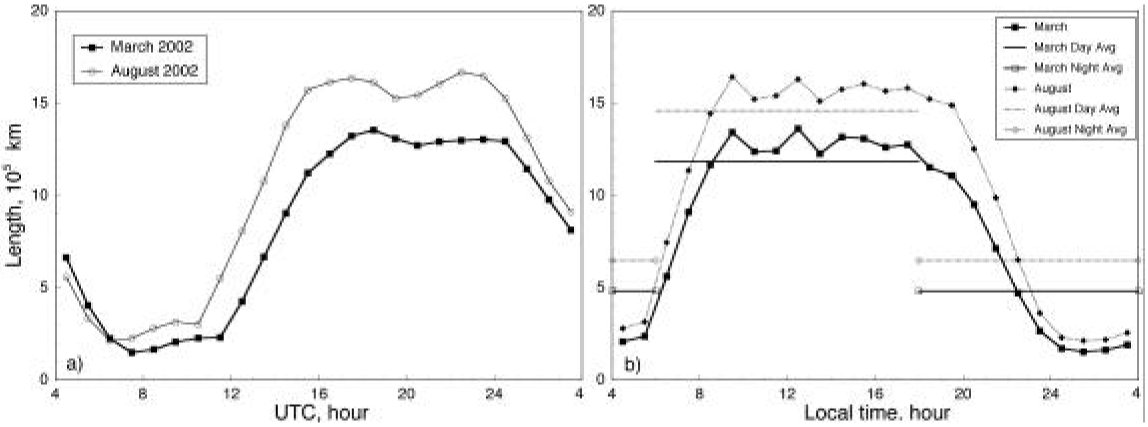

Figure 4. Mean hourly and day-night average CFL, (a) local time and (b) UTC.

4 DISCUSSION

While providing unprecedented air traffic detail, it should be noted that this dataset does not include flights below 25,000 ft, military air traffic, and some air traffic over oceans, Canada, Mexico, and Cuba. Development of a total inventory for this domain would require additional input. Data acquisition, while nominally continuous, was not complete except for a few months. Actions taken to ac count for the missing data when computing monthly means should minimize the impact of the poor data. Data were initially acquired from FlyteComm, Inc. every 2 minutes and the only time associated with each flight number was the local time on the acquisition computer. Thus, the actual flight time could be overestimated by up to 2, 5, or 10 minutes depending on the time interval of reporting for a given flight. Despite these uncertainties in actual time, the data should provide a realistic representation of air traffic over the CONUS.

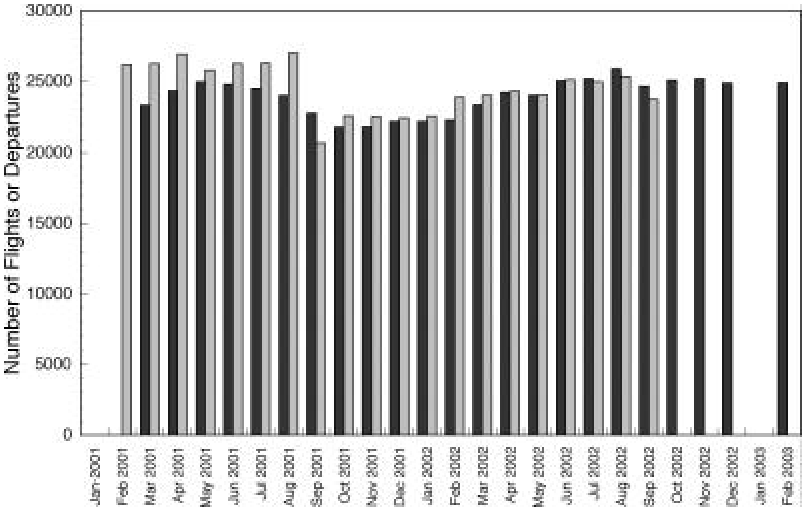

Figure 5. Mean number of daily flights above 7.6 km from FlyteTrax data (black) and departures of commercial carriers from OAI database (shaded).

Previous air traffic fuel usage data from USA sources were developed for 1992 (Baughcum, 1996, Gardner 1998) and include military sources (Metwally, 1995). A comparison of the fuel usage above 7 km from that earlier dataset (Figure 17 in Minnis et al. 1997) and the CFL distribution in Figure 1d reveal some differences that may be due to the lack of military and foreign flights and changes in air traffic patterns since 1992. For example, flights between California and Mexico evident in the 1992 dataset are absent in Figure 1d, while flights from Texas and the eastern USA to Acapulco and Mexico City (Figure 1d) are not as defined in the 1992 dataset. Air traffic over the Pacific is confined to a few narrow air lanes in the earlier dataset compared to the more diffuse air lanes in Figure 6d. Despite many similarities between the two datasets, this air-lane versus diffuse distribution difference is apparent over much of the domain. For example, the maximum fuel expenditure in the 1992 dataset is confined to a latitude strip between 40°N and 42°N between Philadelphia, PA and Iowa with a few secondary maxima over Las Vegas, NV and southern California. In Figure 1d, the maximum CFL covers a much larger area including the relatively narrow strip in the 1992 data. New secondary maxima are evident over northeastern Florida, eastern Arkansas, and eastern Kansas in Figure 1d. Perhaps, additional tourist traffic and the expansion of overnight delivery services with major hubs at Memphis, TN, Wilmington, OH, and Louisville, KY could have increased the traffic over the Midwest and Florida.

The seasonal variation in air traffic in the current dataset appears to be somewhat different than can be inferred from the seasonal variation in North American high-altitude aircraft emissions from the 1992 inventory (Figure 2-7, Friedl, 1997). The earlier data have a peak in NOx emissions during August followed by a 4% drop into September, nearly constant values through December, a 9% decrease to the January minimum, a gradual increase to May, and a rapid rise to the summer maximum. Figure 5 shows an initial May maximum with flight frequency decreasing into October. The number of flights remains depressed until March 2002 when they begin increasing until August 2002. A 6% decrease in flights during September is slightly offset by a 2% rise into October. The flight frequency remained steady through February 2003. This irregular variability is influenced by a number of factors, including the September 11, 2001 terrorist attacks, which can account for part of the October 2001 – February 2002 lull. The first maximum in May 2001 is probably due to sampling deficiencies that were not properly considered. The USA freight traffic, as expressed in overall ton-miles for scheduled and non-scheduled aircraft, increased almost monotonically by a factor of 2.7 between 1981 and 2000 with minor lulls during 1991 and 1999 (OAI, 2003). Similarly, the number of passenger originations increased by a factor of 2.4 during the same period. Both parameters decreased during 2001, especially the air passenger originations. The overall number of scheduled and non-scheduled airport departures for large certified air carriers, which account for most of the high-altitude air traffic are in good agreement with the current database (Figure 5) except for the period prior to September 2001 when sampling was the worst. When these sampling effects are taken into account, the monthly averages for the earlier period will probably be in better agreement.

The diurnal variation of flights is generally consistent with the available information on contrails over the CONUS. The unnormalized frequency of persistent contrails more than doubles between 0600 LT and 0800 LT when it reaches a maximum around 0900 LT (Minnis et al. 2003). The average CFL also increases by more than a factor of 2 between 0600 and 0800 LT and reaches a peak at 0930 LT (Figure 4). Mean CFL decreases very slowly during the daylight hours without a significant drop until after 1800 LT, while the contrail frequency also gradually decreases after 0800 LT before dropping at 1800 LT. The lack of contrail frequency data during the night precludes further comparison. However, the correspondence between contrails and flight lengths during the daytime suggests that the CFL data could be used to estimate the relative hourly frequency of contrail occurrence at night.

5 CONCLUDING REMARKS

This new database constitutes a different characterization of air traffic than previously available. It provides explicit flight paths and flight density in terms of cumulative flight length rather than fuel usage. Actual flight paths were used instead of estimated flight paths between terminals. Because of data dropouts, caution must be used when simulating the air traffic for a particular day. The statistics provided here represent an initial summary of the dataset but have not accounted for all of the effects of missing data. After final quality control has been completed (tentatively late 2003), the database will be made available via the World Wide Web.

Air traffic over the USA is marked by distinct daily, weekly, and annual cycles that can affect evaluations of aircraft effects on the atmosphere. When properly used, the dataset described herein should prove valuable for realistically simulating air traffic at a variety of scales.

REFERENCES

Baughcum, S. L., 1996: Subsonic aircraft emission inventories, In: *Atmospheric Effects of Aviation: First Report of the Subsonic Assessment Project*, NASA RP-1385, pp. 15-29.

Friedl, R. R. (ed.), 1997: *Atmospheric Effects of Subsonic Aircraft: Interim Assessment Report of the Advanced Subsonic Technology Program*, NASA RP 1400, 168 pp.

Gardner, R.M. (ed.), 1998: *ANCAT/EC Aircraft Emissions Inventory for 1991/92 and 2015.* Final Report EUR-18179, ANCAT/EC Working Group. Defence Evaluation and Research Agency, Farnborough, United Kingdom, 108 pp.

IPCC**,** 1996: *Climate Change 1995: The Science of Climate Change. Contribution of Working Group I to the Second Assessment Report of the Intergovernmental Panel on Climate Change* [Houghton, J.T., L.G. Meira Filho, B.A. Callander, N. Harris, A. Kattenberg, and K. Maskell (eds.)] and WMO/UNEP. Cambridge University Press, Cambridge, United Kingdom and New York, NY, USA, 572 pp.

Metwally, M. 1995: *Jet Aircraft Engine Emissions Database Development--1992 Military, Charter, and Non-scheduled Traffic*, NASA CR-4684.

Minnis, P. J. K. Ayers, and S. P. Weaver, 1994: *Surface-Based Observations of Contrail Occurrence Frequency Over the U.S., April 1993 - April 1994*, NASA RP 1404.

Minnis, P. J. K. Ayers, M. L. Nordeen, and S. P. Weaver, 2003: Contrail frequency over the USA from surface observations," *J. Climate*, in press.

OAI, 2003: *Air Traffic Statistics and Airline Financial Statistics, Historical Air Traffic Data for 1981-2001*, U.S. Department of Transportation, Bureau of Transportation Statistics, http://www.bts.gov/oai/indicators/top.html.

Validation of the Kinetic Soot Model: An Experimental and Theoretical Study on Soot Formation using LII and SV-CARS

K.P. Geigle*, Y. Schneider-Kühnle, V. Krüger, M. Tsurikov, R. Lückerath, M. Braun-Unkhoff,
N. Slavinskaya, P. Frank, W. Stricker, M. Aigner
DLR - Institut für Verbrennungstechnik, Stuttgart, Germany

Keywords: laser-induced incandescence, CARS, soot formation, kinetics

ABSTRACT: Temperature and soot concentration measurements from laminar, premixed flames at different conditions (pressures P, equivalence ratios ϕ and fuels), provide an excellent data base for the modelling of soot formation. For the verification of numerical simulations of sooting flames, the use of accurate, spatially and temporally resolved data measured with non-intrusive *in situ* measurement tools is necessary. We present the application of a recently developed technique for temperature measurements in sooting flames. Soot concentrations measured by laser-induced incandescence (LII) are compared to calculated profiles of soot formation, based on the measured temperatures. The overall agreement is quite satisfactory for the experimental conditions presented.

1 INTRODUCTION

Environmental concerns and decreasing pollutant emission limits are driving the need for a reduction of emissions such as soot. Therefore, fundamental understanding of soot formation and destruction is a current issue for industry and research. The first step to a better understanding is based on a separation of effects interacting in a complex way in realistic combustion systems. Thus, as one part of the problem, pure chemistry (no turbulence) needs to be investigated. Since chemistry is strongly dependent on temperature, the development and validation of a soot model needs accurate temperature information and soot concentrations measured under several flame conditions. Most practical combustion devices are operated at elevated pressure, but little data are available for flame experiments focusing on soot model validation at these conditions (Hanisch et al., 1994; Braun-Unkhoff et al., 1998). To provide the required information, we used laser-based, non-intrusive diagnostics which yield spatially-resolved data, necessary for resolving steep gradients. The main advantage of this approach over commonly-used line-of-sight techniques is that the assumption of a homogeneous distribution of the quantity of interest over large dimensions is not required (and in many flames not justified). The experiments are used to support kinetic computations in two respects. First, the measured temperature information is used for the calculation, thus including energy loss by radiation. Second, the predicted soot formation can be compared to the experimental soot volume fraction profiles. This comparison permits further refinement of the kinetic soot formation model.

2 EXPERIMENTAL SET-UP

2.1 *Burner configuration*

Validation experiments in high pressure flames for the support of a kinetic soot model without any influence of turbulence are a highly demanding challenge for burner design. First, a completely laminar flow resulting in a stable flame without flickering is required. In this case, a direct correlation of height above burner (HAB) with the time scale of the combustion process under study is possible.

---

* *Corresponding author:* Klaus Peter Geigle, DLR – Institut für Verbrennungstechnik, Stuttgart, D-70569 Stuttgart, Germany. Email: klauspeter.geigle@dlr.de

Furthermore, the flame needs to be sufficiently homogeneous over the measurement volume. For a comparison with 1D kinetical computations, any influence from the flame edges has to be excluded. Our design, based on the requirements stated above, is similar to the ones described in Hanisch et al. (1994) and Jander et al. (1995). Its main feature is the use of a non-sooting shielding flame (d = 61.3 mm), surrounding the axisymmetric inner flame to be studied (d = 41.3 mm). The additional flame reduces oxidising influences from the flame edges and provides a hot shielding film against the surrounding cold coflowing air (d = 150 mm). Moreover, two separately operated flames are useful while changing flame conditions (P, ϕ, flow rates), since they behave as mutually pilot flames. Both flames were stabilised on water cooled sintered bronze matrices (cell size 12 μm). Additional flow conditioning and mixing of fuel and air was achieved by using glass beads below the matrices. For finding the required stable flames, the stoichiometries of both flames and the exit velocities of three cold gases (methane/air, fuel/air of studied flame, coflowing air) must be carefully adjusted. The flow rates, supplied by five in-house calibrated massflow controllers, are chosen to avoid horizontal flickering and vertical fluctuations, and to ensure a sufficiently homogeneous radial temperature and soot distribution within the detection volume of the used laser techniques. Premixing of the fuel and the corresponding air took place approximately one meter before the burner.

The entire burner inlet system was mounted into a high pressure housing with large windows for optical access. For further flame stabilisation, particularly at high pressures, a stabilising grid was positioned at a height of 40 or 45 mm above the burner plate, depending on the position of soot formation (Pape, 1993). For the experiments with toluene, the required combustion air was passed through a toluene bubbler consisting of several sealed bottles immersed in a water bath whose temperature was precisely controlled. A part of the air-toluene mixture was sampled and the toluene volume fraction determined *ex situ*. Each of the flame settings (Table 1) has been checked for reproducibility, the different measurements were usually performed the same day.

Table 1. Flame settings for the presented flames. All flow rates are in standard liters per minute. Pressure is in bars.

	Inner flame			Ring flame		Coflow	P		Inner flame			Ring flame		Coflow	P
Fuel	ϕ	Q_{fuel}	Q_{air}	Q_{CH4}	Q_{air}	Q_{air}		Fuel	ϕ	Q_{fuel}	Q_{air}	Q_{CH4}	Q_{air}	Q_{air}	
C_2H_4	2.30	0.7	4.4	1.0	4.6	110	1	C_3H_6	1.95	1.17	13	9.9	58	490	5
C_2H_4	2.30	1.7	11	5.7	38	390	3	C_3H_6	2.00	1.20	13	9.9	58	490	5
C_3H_6	2.23	0.3	3.1	1.5	11	200	1	C_3H_6	2.10	1.26	13	9.9	58	490	5
C_7H_8	1.88	0.064	1.5	1.9	11	98	1	C_3H_6	2.15	1.29	13	9.9	58	490	5

2.2 *Temperature measurements in sooting flames with SV-CARS*

While the use of thermocouples provides the easiest way of extracting temperature information from the flame, the accuracy in sooting flames is too low for model validation and, furthermore, any object introduced into the flame clearly disturbs the flame (Stricker, 2002). An ideal tool for *in situ*, non-intrusive temperature measurements in flames is Coherent Anti-Stokes Raman Scattering (CARS), which is based on measuring the population of rotational and vibrational energy levels of the nitrogen molecule (Eckbreth, 1996) and comparing these to simulated spectra. Conventional CARS uses the frequency-doubled output of a Nd:YAG laser (532 nm) for the pump beam. However, in a sooting flame, the exciting beams produce C_2 molecules from laser heated soot particles, which in turn cause fluorescence (Swan bands) at the same wavelength as the CARS signal (473 nm). Our approach is to use a narrowband dye laser (591 nm) for the pump beam, thus shifting the CARS signal out of the Swan band region. So the CARS signal is spectrally shifted from 473 nm to 520 nm resulting in completely undisturbed spectra (Fig. 1a). For non-sooting parts of a flame this shifted vibrational CARS signal was validated with conventional CARS, resulting in good agreement. The accuracy for SV-CARS measurements is ±3% (Schneider-Kühnle, 2003).

In our experiment, a frequency-doubled Nd:YAG laser was used to pump a narrowband dye laser and a custom-built broadband dye laser, whose beams were overlapped in BOXCARS geometry and focused to a 4 mm long, 0.2 mm wide probe volume. All beams were equipped with polarisers and half wave plates for intensity control; an additional analyser could be implemented for background suppression in the case of pressurised flames. Two translation stages allowed a fast shift of the CARS measurement probe volume above the burner surface. The CARS signal was resolved in a spectrometer and detected with an intensified CCD camera.

2.3 *Soot distributions with laser-induced incandescence*

An excellent tool for *in situ* non-intrusive measurements of soot distributions is provided by laser-induced incandescence (LII), based on the emission of blackbody radiation resulting from strong laser induced heating of soot particles. In recent years, LII has matured into a reliable tool for the measurement of qualitative soot distributions and, with calibration, even for quantitative measurements in flames (Santoro and Shaddix, 2002). For calibration, an extinction measurement is typically performed. Uncertainties in the exact knowledge of the refractive index of soot, particularly at the position of the calibration measurement (Choi et al., 1994), determine the accuracy of calibration via extinction. To ensure a proper excitation especially in strongly sooting absorbing flames we used a power meter to monitor the energy in the laser sheet after it passed through the flame.

For excitation of the LII signal we used the 1064 nm output of a Nd:YAG laser. A set of sheet forming optics and a rectangular aperture produced a homogeneous excitation sheet of approximately 30 mm in height and 170 µm in width. The laser power was tuned by a half wave plate followed by a polariser to keep an energy of close to 35 mJ/pulse behind the flame. The LII signal was filtered at 450 nm and detected with an intensified CCD camera with two-frame capability. During the first gate immediately before the laser pulse, the flame luminosity was detected. The second gate of 40 ns duration over the laser pulse was used for detection of the signal.

For the extinction measurement the same optical pathway was used by the 532 nm output of the laser at low power (0.2 mJ/pulse in the sheet) to avoid processes other than extinction in the flame. Before entering the burner chamber a part of the laser sheet was reflected into a reference dye cell. The rest of the sheet was partially absorbed by the flame and afterwards refocused to a second dye cell. The use of an additional mirror in front of the CCD camera and changing to a 700 nm interference filter allows the detection of an extinction profile immediately after the LII measurement with the same camera. This approach is applicable since the measurement object is temporally stable. In contrast to other published data, where the integral extinction over the whole flame is measured (Axelsson et al., 2001) our set-up allows us to choose the best height for the calibration. While in the lowest regions of the flame extinction by soot is low, absorption by other species might influence the extinction measurement in a non-negligible way (Choi et al., 1994). Furthermore, in the region of initial soot production the soot properties are the least representative for the whole flame and not well known. High in the flame soot particles start aging, which again changes the optical properties. For data analysis we used the region between these extremes where the determined calibration constant remains stable (as indicated in Figure 1b).

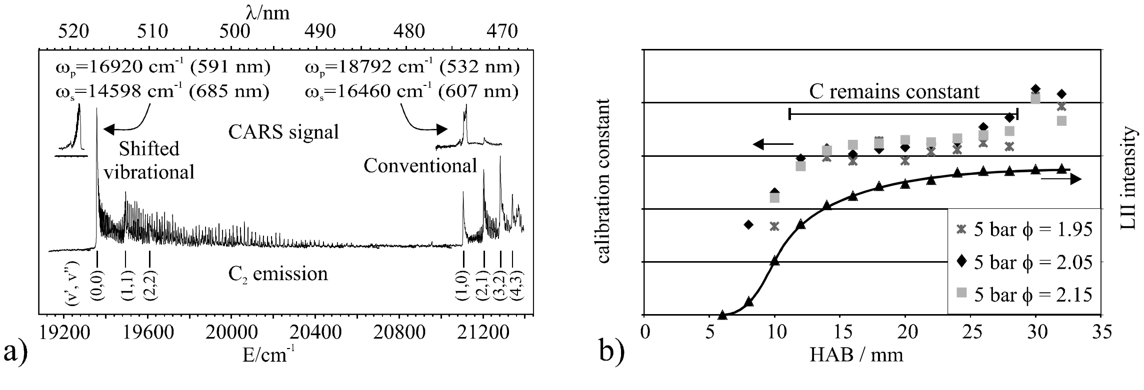

Figure 1. a) Spectral position of the conventional and the SV-CARS signal in the C_2 Swan-Band system. b) Variation of the calibration constant with height in different propene/air flames at 5 bar. Also shown for comparison is a LII signal intensity profile for the ϕ = 2.15 flame.

Since in strongly sooting flames the effect of signal trapping is not negligible, we followed the approach described in Bryce et al. (2000) to correct for signal losses by absorption in the flame. The refractive index used in the data analysis was 1.60 – 0.59i (Charalampopoulos and Felske, 1987). A change of optical pathways necessary for the mentioned techniques (CARS, LII, extinction) took only a few seconds by using the aforementioned translation stage system (Fig. 2a).

Figure 2a. Experimental set-up; translation stages enable a quick change between SV-CARS, LII and extinction measurements. b and c: Stability of the studied flames demonstrated for a 3 bar ethene/air flame; the upper image shows the standard deviation over a sequence of 100 LII images, the lower image displays some subsequently detected LII profiles along the burner axis.

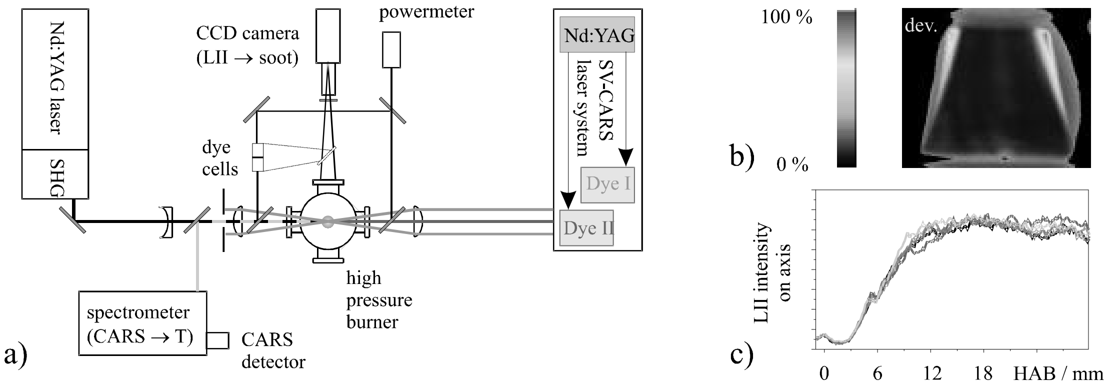

3 KINETIC SOOT MODEL

At present, detailed modelling of soot formation and destruction is executed by using a relatively large gas phase reaction mechanism - including an improved model which contains detailed chemistry for PAH growth - coupled with a mechanistic soot model for particle inception, coagulation of particles, condensation, surface growth by gaseous species and soot particle oxidation (based on Frenklach and Wang, 1994).

A recently published reaction mechanism (Wang and Frenklach, 1997), which comprises the reactions of aromatic species up to pyrene, was updated by taking into account results obtained by shock tube experiments, especially on reactions of toluene, phenol, phenylacetylene, cyclopentadiene, propargyl and phenyl and benzyl radicals (Hu et al., 1999). This updated mechanism was validated by modelling the concentration profiles measured in a laminar, sooting ethene/O_2/Ar flame operated at atmospheric pressure (Harris et al., 1988). Measured species profiles of C_1-, C_2- and first aromatic ring compounds were reproduced very well.

As the base model for calculating the measured soot volume fraction f_v, the original soot model (Frenklach and Wang, 1994) was applied without any changes. This soot model describes PAH growth by linear lumping in which reactions of hydrocarbons with different numbers of condensed 6C rings (ranging from 3 to 7) are described by a replicating HACA (H̲ydrogen A̲bstraction C̲arbon A̲ddition) reaction sequence. Particle inception occurs via PAH coagulation, starting with A4 (pyrene, $C_{16}H_{10}$). Further growth of the particles proceeds by coagulation of the particles and by surface growth controlled by reactions of the soot surface with OH and O_2.

One aim of the present study was to replace the PAH growth described by the HACA sequence by a comprehensive reaction mechanism which contains detailed kinetics for PAH species including the elementary reaction steps used in the HACA sequence. A reaction mechanism from MIT (Richter et al., 1999) comprising detailed kinetics to form species up to C_{30} was chosen. All the large PAHs formed in the PAH growth model were assumed to collide giving rise to nuclei: different combinations of PAH monomers are assumed to collide and form dimers; in a second step, these dimers collide with other monomers or dimers producing trimers etc. If the growing PAH has an amu > 760, a nucleus is born (Hu et al., 2000).

4 RESULTS AND DISCUSSION

Several flames using different fuels at different equivalence ratio and pressure were studied. LII intensity fluctuations in the central part of the flames typically remain below 15 % indicating sufficiently stable objects of measurement (Fig. 2b, c). Figure 3a shows the results for a 1 bar ethene/air flame at ϕ=2.3. The figure shows measured soot volume fraction and temperature as a function of HAB, along with soot volume fraction results from the kinetic soot model. The soot plateau level of 0.8 ppm fits into the set of measurements of Jander et al. (1995) and Axelsson et al. (2001). The used soot model which was improved in the present work especially with respect to the growth of PAH, gives better agreement with measured soot concentration profiles than the initial soot model by Frenklach and Wang (1994) that used only the lumped HACA mechanism (alternating H-abstraction and C_2H_2 addition) for PAH growth. This is caused by an increased particle inception predicted by the detailed model for PAH growth as a consequence of the increased rate of soot precursor formation and thus that of particles. A comparison of our measured temperatures with published temperatures for similar flames is not useful. Temperatures depend strongly on flow speed (losses to the burner plate) and radiative losses to the specific surroundings. Additionally, the published results are based on thermocouple data or line of sight measurements thus not providing the accuracy and spatial resolution to be used as input for simulations. Our CARS measurements resulted in peak temperatures of 1715 K. Evidence for radiative energy loss is given by the downstream temperature decrease. When performing statistical analysis of 600 single CARS spectra, even in the very steep temperature rise, the single pulse temperature distribution at one location is shown to be relatively narrow (±100 K), proof of the excellent temporal and spatial stability of this flame and excluding height fluctuations of the reaction zone larger than 0.5 mm.

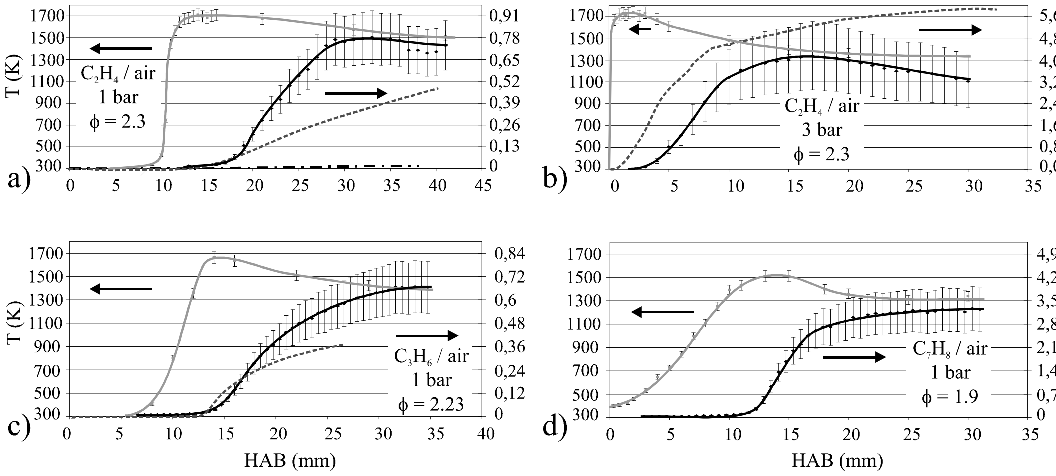

Figure 3. Measured temperature profiles (left scale) and soot volume fractions (right scale) for laminar premixed flames under the indicated conditions. Apart from the toluene flame (d) the actual kinetic computation results containing detailed gas phase chemistry are shown (dashed line). For the upper left flame (a) additionally a comparison with the pure HACA mechanism (dash dotted) is visible.

A clear benefit of the experimental set-up for simulations is to be emphasised: Even a lifted flame can be stabilised above the matrix surface by using the second (ring) flame. Thus, temperature measurements below the reaction zone can be performed resulting in well known starting conditions for the modelling.

It should be mentioned that the existence of a spatially resolved temperature profile measured with high accuracy is of great advantage with respect to the soot modelling especially as pressure increases and the reaction zone becomes very thin as in Figure 3a. Because temperature dominates the onset of soot formation, it is clear that modelling dynamic soot formation requires a realistic temperature profile between burner surface and post flame zone (Hu et al., 2000).

Increasing the pressure changes the profiles dramatically (Fig. 3b). At the lowest accessible height of 0.3 mm the temperature is already higher than 1600 K, indicating that the reaction takes place immediately above the burner surface. Absence of C_2 interferences at these high soot levels indicates the full functionality and reliability of the modified technique. At 3 bar the detected peak temperature was 1730 K, similar to the 1 bar case. At 2 mm above the reaction zone the soot concentration begins to rise, achieving a maximum of 4 ppm at 14 mm HAB.

These plateau soot volume fractions result in more than 30 % absorption of emitted LII signal, giving evidence to the need of correction for signal trapping.

For this flame, the starting conditions, i.e. the temperature at HAB = 0 for kinetic calculations, are not as well defined as in the 1 bar case. For the simulation a linear interpolation was performed between the first measured temperature and estimated room temperature at the burner surface. While the position of the soot rise is predicted too low, the slope of the calculated profile is in good agreement with the experiments and the final soot level is overestimating the measured values. Nevertheless, the overall agreement is satisfying.

Changing the fuel to propene does not dramatically influence the shape of the measured profiles (Fig. 3c). As for ethene, a lifted propene flame could be stabilised at atmospheric pressure and even the measured plateau soot level of 0.7 ppm is similar. The measured peak temperature is close to 1660 K. As in the former examples, there is good agreement of the calculated soot volume fraction with the measured one, clearly showing the correct trends.

Increasing the pressure to 5 bar resulted in significant problems in flame stabilisation. Even though the outer flame shape remained stable, the best achieved flames exhibited fluctuations of 1 – 2 mm at the lower edge and pronounced soot streaks at randomly changing positions. This caused unacceptable fluctuations in the CARS spectra, preventing accurate temperature measurements (i.e. narrow distribution at one position). Averaging 100 LII images removed the streaky structures completely, providing satisfactory qualitative information. Figure 4 shows LII images at 5 bar with inner flame ϕ=1.95 to 2.15. Since only the inner fuel flow rate was varied slightly (by less than 1 % of the total inner flow rate), the overall flow conditions are about the same for all flames. The richer the flame is the higher the plateau soot level.

The main components of aeroengine fuel are aliphatic hydrocarbons based on the above described ones. Even for longer chained hydrocarbons, the reaction mechanisms are not expected to be completely different. At lower concentrations available in the fuel but exhibiting higher soot forming potential, aromatic hydrocarbons are an essential object of interest for chemical kinetics. In particular, conventional models are based on soot formation over aromatic hydrocarbons after an initial fuel fragmentation. Thus, a direct study of an aromatic compound as fuel gives additional insight into the process of soot formation and the role of these species in the network of chemical reactions. As representative of aromatic molecules, toluene was chosen. Using the aforementioned liquid bubbler system, a laminar premixed toluene/air flame was stabilised at atmospheric conditions (Fig. 3d). Two main differences to the above described profiles are obvious: First, the temperature rise is much slower, proceeding over 8 mm and reaching a maximum of 1500 K, approximately 300 K below the adiabatic temperature for ϕ = 1.9, caused by the very low flow speed accompanied by radiative losses. Second, the plateau soot level is much higher indicating the large soot formation potential of aromatic compounds.

Figure 4. Soot distributions and vertical profiles upon change of the equivalence ratio for propene/air flames at 5 bar, not corrected for LII signal scattered at the burner surface.

5 CONCLUSIONS

For the measurement of accurate model validation data the need for spatially resolved, *in situ*, nonintrusive measurement methods has been addressed. The presented work describes the application of a modified CARS excitation scheme for temperature determination in sooting flames (SV-CARS) in combination with soot volume fraction measurements by LII. To obtain a comprehensive data set for the soot model development and validation, accurate measurements of temperature and soot concentration have been performed in quasi 1D flames for ethene, propene, and toluene with various equivalence ratios and at pressures up to 5 bar. These experimental data could successfully be used for comparison with soot formation calculated by kinetic computations. The model predictions showed satisfactory agreement with the measurements; the main features of the measured soot profiles are correctly predicted. Further research is necessary with respect to the transition from PAH species to the first coagulating particles (e.g. incorporation of combinative reactions, Böhm et al., 2003) and to soot oxidation.

6 ACKNOWLEDGEMENTS

The authors want to thank Dr. R. Hadef for support during measurements and data analysis, funded by the Alexander von Humboldt-Foundation, the Helmholtz-Gemeinschaft Deutscher Forschungszentren (HGF) for funding during the research program “Particles and cirrus clouds” (PAZI), and M. Kapernaum for performing the volumetric analysis of the toluene mixture.

REFERENCES

Axelsson, B., R. Collin, P.E. Bengtsson, 2001: Laser-induced incandescence for soot particle size and volume fraction measurements using on-line extinction calibration. *Appl. Phys. B 72*, 367.

Böhm, H., M. Braun-Unkhoff, P. Frank, 2003: Investigations on initial soot formation at high pressures. *Progress in Computational Fluid Dynamics 3 (2-4)*, in press.

Braun-Unkhoff, M., A. Chrysostomou, P. Frank, E. Gutheil, R. Lückerath, W. Stricker, 1998: Experimental and numerical study on soot formation in laminar high-pressure flames. 27th Symp. (Int.) on Combustion, The Combustion Institute, Pittsburgh, p. 1565.

Bryce, D.J., N. Ladommatos, H. Zhao, 2000: Quantitative investigation of soot distribution by laser-induced incandescence. *Appl. Opt. 39*, 5012.

Choi, M.Y., A. Hamins, G.W. Mulholland, T.Kashiwagi, 1994: Simultaneous optical measurement of soot volume fraction and temperature in premixed flames. *Combustion and Flame 99*, 174.

Charalampopoulos, T.T., J.D. Felske, 1987: Refractive indices of soot particles deduced from in-situ laser light scattering measurements. *Comb. Flame 68*, 283.

Eckbreth, A.C., 1996: Laser diagnostics for combustion temperature and species. Overseas Publishers Association, Amsterdam B.V.

Frenklach, M., H. Wang, 1994: Detailed mechanism and modelling of soot particle formation. Springer-Verlag Berlin, Springer Series in Chemical Physics 59, 165.

Hanisch, S., H. Jander, T. Pape, H.G. Wagner, 1994: Soot mass growth and coagulation of soot particles in C_2H_4/air-flames at 15 bar. 25th Symp. (Int.) on Combustion, The Combustion Institute, Pittsburgh, p. 577.

Harris, S.J., A.M. Weiner, R.J. Blint, 1988: Formation of small aromatic molecules in a sooting ethylene flame. *Combust. Flame 72*, 91.

Hu, D., M. Braun-Unkhoff, P. Frank, 1999: Modelling study on soot formation at high pressures. *Combust. Sci. & Technol. 49*, 79.

Hu, D., M. Braun-Unkhoff, P. Frank, 2000: Modelling study on initial soot formation at high pressures. *Z. Phys. Chem. 214 (4)*, 473.

Jander, H., N. Petereit, D.M. Razus, 1995: The influence of carbon density on soot growth in atmospheric C_2H_4 (air, O_2)-flames. *Z. Phys. Chem. 188*, 159.

Pape, T., 1993: Optische Untersuchungen zum Rußwachstum in vorgemischten Ethen-Luft Flammen bei 15 bar. Diplom-Thesis, Göttingen, 17 pp.

Richter, H., W.J. Grieco, J.B. Howard, 1999: Formation mechanism of polycyclic aromatic hydrocarbons and fullerenes in premixed benzene flames. *Combust. Flame 119*, 1.

Santoro, R.J., C.R. Shaddix, 2002: Laser-induced incandescence. In: Applied Combustion Diagnostics [K. Kohse-Höinghaus, J.B. Jeffries (eds.)]. Taylor & Francis, New York, 252, and references therein.

Schneider-Kühnle, Y., 2003: Experimentelle Untersuchung rußender Hochdruckflammen mit Laserdiagnostischen Messmethoden. PhD Thesis, DLR Stuttgart, in progress.

Stricker, W., 2002: Measurement of temperature in laboratory flames and practical devices. In: Applied Combustion Diagnostics [K. Kohse-Höinghaus, J.B. Jeffries (eds.)]. Taylor & Francis, New York, 155.

Wang, H., M. Frenklach, 1997: A detailed kinetic modelling study of aromatics formation in laminar premixed acetylene and ethylene flames. *Combust. and Flame 110*, 173.

AvioMEET Inventory Tool and its Applications

M. Bukovnik*, M. T. Kalivoda
psiA-Consult GmbH, Vienna, Austria

Keywords: air traffic, emission factors, calculation software, application

ABSTRACT: Increasing numbers of flights and still unknown effects of exhaust gasses on the high atmosphere have drawn most attention on air traffic and its emissions. In Europe, many institutions are working in this area, collect traffic and emission data, create emission inventories and assess effects. That lead to some work done in parallel while using different databases and methodologies which often lead to results that cannot be compared or matched. COST 319 action and MEET project were a starting point for a dialogue and discussions between the different communities involved and thus gave an incentive for harmonisation. MEET project came up with a methodology for estimating air pollutant emissions from present and future air traffic. Methodology and emission indices are now used for strategic environmental assessment and transport policy making. The COST 319 working group D2 – air traffic – has proposed minimum requirements for an harmonised approach to generate emission indices. This seems to be the only way make results from different inventories comparable and exchangeable. Harmonisation work is going on under the umbrella of the Thematic Network Aeronet. Methodology used in MEET project and presented here is based on a flexible design that allows to adjust it to the user requirements as well as on air traffic data and emission factors (easily) available. Based on the MEET methodology an MS-Access computer tool was created, called AvioMEET, which uses most of the Emission Indices published in the Emission Index Sheets of MEET/Deliverable 18. TRENDS finally uses all this more or less theoretical knowledge to apply it on existing traffic activity data to come up with a database of environmental indication for air transport.

1 INTRODUCTION

However with the number of aircraft movements ever increasing coupled with the fact that the impact that these gases have on the atmosphere varies in a non-linear manner with altitude has drawn considerable attention on this transport sector. For this reason many institutions have been working on collecting traffic and emissions data, generating emission inventories and assessing the effect that air transport has on the atmosphere. As well as work on the current situation, research into future scenarios and trends has also been undertaken.

Owing to much interest in the area a lot of research was conducted in parallel resulting in much duplication of work. As is to be expected with such a scenario many different results were reached. Also methodologies, tools and emission factors of various quality were used.

As this field of research has gained such attention it became apparent that a standard system would be needed in order for future work to be acceptable. COST 319 marked the start of a dialogue between the main players in this area in Europe. This dialogue has lead to steps being made towards harmonising methodologies and concentrating the activities with DG VII’s support.

The COST 319 working group D2 – air traffic – has worked out a proposal for a harmonised approach to generate emission indices (EIs). From the working group’s point of view this harmonisation is necessary to make results from different inventories and actions like Corine, IPCC etc. comparable and exchangeable.

---

2 THE MEET AIR TRAFFIC METHODOLOGY

MEET stands for Methodologies for Estimating Air Pollutant Emissions from Transport. The MEET project - funded by the European Commission under the transport RTD programme of the 4th framework programme - has been undertaken in order to provide a basic, Europe-wide procedure for evaluating the impact of transport on air pollutant emissions and energy consumption.

A methodology for estimating air pollutant emissions from air traffic was created. Although military operational flights and VFR (Visual Flight Rules) flights are included IFR (Instrument Flight Rules) flights were focused on. EIs for components NO_x, CO, HC, CO_2, H_2O, SO_2 and fuel consumption are published for 30 aircraft/engine combinations.

2.1 *Outline methodology for baseyear*

In common with the other MEET methodologies for emission calculations, estimation of air traffic emissions combines an estimate of the amount of transport activity with emission factors per unit of activity to derive total emissions (Kalivoda/Kudrna 1997). As with the other modes of transport, there needs to be a classification of the transport activity to take into account the differences between types of aircraft/engine combination, their different operating modes, the different pollutants and so on. The method used follows those for the other non-road modes: an initial estimate is made of the fuel consumed during an air transport operation and pollutant emissions are calculated using fuel-specific emission factors.

Three main classes of air transport can be distinguished:

- flights performed under Instrument Flight Rules (IFR)
- flights performed under Visual Flight Rules (VFR)
- military operational air traffic (MOT)

For each category a typical data set is available for traffic characteristics and engine emissions, although the accuracy of the data within the three categories is different.

2.2 *ATEMIS simulation program: Methodology for IFR flights*

Methodology for IFR flights is based on standard flight profiles for about 35 aircraft/engine combinations which represent about ¾ of European air traffic. Dividing each flight profile into several sectors of constant performance (= standard operating conditions SOC) and emission characteristics allows to adapt the algorithm to different user requirements (i.e. airport/in flight emissions) and gives the chance to improve results by increasing resolution:

$$TE_p = \sum_r \sum_j SE_{j,p,r} \cdot N_{j,r} \qquad (1)$$

$$SE_{j,p,r} = \sum_s FC_{j,s}(CR_{ALT}(D_r)) \cdot EI_{j,p,s}(CR_{ALT}(D_r)) \qquad (2)$$

TE_p	Total emission of pollutant p [kg per period]
$SE_{j,p,r}$	Specific emission of pollutant p, of aircraft/engine combination j on a route r [kg per aircraft]
$N_{j,r}$	Number of aircraft of category j on route r per period [aircraft per period]
$FC_{j,s}(CR_{ALT})$	Total fuel consumption of aircraft category j for standard operating condition s [kg_{FUEL}/SOC]
$EI_{j,p,s}(CR_{ALT})$	Emission index of aircraft category j for pollutant p and SOC s [$kg_{EMISSIONS}/kg_{FUEL}$]
Dr	Distance between city pair (=route r) [km]
j	Aircraft/engine category
p	Pollutant
r	Route from airport to airport
s	standard operating condition s

That leads to a set of emission indices (EI, the mass of pollutant produced per mass of fuel used) for eight typical operational conditions, which may be combined to cover most of an aircraft's operation during a flight profile. The standard operating conditions are:

- starting up engines,
- taxi out, take off,
- climb, cruise, descent,
- landing, taxi in.

Emission factors are based on engine certification data in the ICAO (International Civil Aviation Organisation) Engine Exhaust Emission Databank [ICAO 1995]. This databank contains data sets of thrust (engine performance), fuel flow and emissions of components CO, NO_X and VOC which apply to four different power settings, Mach number 0 and altitude 0 m.

Table 1. Example for an aircraft emission index sheet

B 737 generic			Boeing B 737 with engine mix						
			duration	distance	Fuel burned		specific Emission parameters		
			of OS	of OS	total	specific	EI.NOx	EI.CO	EI.HC
			[s]	[km]	[kg]	[kg/s]	[g/kg]	[g/kg]	[g/kg]
operational state (OS)		Index	*DUR*	*D*	*FC*	*SFC*	*SENOx*	*SECO*	*SEHC*
1	engine start	es	global figurs for duration and HC emissions, see chapter 3.5						
2	taxi out	txo	default		const	const	const	const	const
3	take off	tff	default		const	const	const	const	const
4	climb	cl		f(cralt)	f(cralt)		f(cralt)	f(cralt)	f(cralt)
5	cruise	cr				f(cralt)	f(cralt)	const	const
6	descent	dsc		f(cralt)	f(cralt)		f(cralt)	f(cralt)	f(cralt)
7	landing	ld	default		const	const	const	const	const
8	taxi in	txi	default		const	const	const	const	const
9	ground operations	go	global figurs for duration and HC emissions, see chapter 3.5						
	EI.CO2		[g/kg]	default					
	EI.SO2		[g/kg]	default					
	EI.H2O		[g/kg]	default					

Using additional information on the aircraft performance during the flight from the emission simulation model ATEMIS (Kalivoda/Feller 1995) leads to average emission indices. Simulations were carried out for thirty of the most common aircraft used in Europe, representing about 70% of flights. Components of the burnt fuel include H_2O, CO_2, CO, NO_X, VOC and SO_2. There is a great uncertainty about other pollutants such as soot, PAH, CH_4, NO_2 or NH_3 so these cannot be included at the moment.

For each of the 30-aircraft/engine combination, all essential parameters and all necessary information for calculating an emission profile are given in a so-called Emission Index Sheet (EIS). Table 2 gives an example of such a data sheet. Default values (*default*) are provided for duration of taxi out, take off, landing, taxi in as well as for the ground operations. Fields marked with '*const.*' contain a single number for fuel burned or EI. The rest of the EIs are strongly depending on the (*average*) cruise altitude (*cralt*). A grey box in the sheet means no data available or provided at the moment.

Distance flown *(D)* and cruise altitude *(CRALT)* are the two basic input parameters to determine the geometric shape of a flight profile on a mission. The total distance of a city-pair is the sum of the distances flown during the three operational states climb, cruise and descent. The average climb and descent rate has been defined so climb and descent distance are just a function of cruise altitude *(CRALT)*. Finally the aircraft type is needed to determine the profile. Additional information which is useful:

- average duration of taxi out [s]
- average duration of taxi in [s].

2.3 *Methodology for VFR and military flights*

EI for military and VFR flights are based on hours of operation and average fuel consumption per hour because of limitations in the nature of the data available. Components included are H_2O, CO_2, CO, NO_X, VOC and SO_2. Data availability for VFR flights is very similar to that of military air traffic. That means no detail information on flight path and specific emissions is available so an algorithm is used which is the same as for military.

$$TVE_p = \sum_v EI_{v,\,p} \cdot FC_v \cdot H_v \qquad (3)$$

TVEp ....Total VFR flight emission of pollutant *p* [kg per period]
Hv............Hours of operation of aircraft class *v* per period [hours per period]
FCv ....Fuel consumption of aircraft class *v* per hour [kg_{FUEL}/hour]
EIv,p........Emission index for pollutant *p* [$g_{EMISSIONS}/kg_{FUEL}$]
v ....VFR aircraft class
p ....Pollutant

The ICAO engine exhaust emission databank does not provide any information since there is no ICAO certification of such engines.

3 AVIOMEET SOFTWARE TOOL

The software tool AvioMEET is based on the data published in the Emission Index Sheets of MEET/Deliverable 18. This methodology includes the emission profiles for a single flight on a city pair, or mission, emission functions for fuel flow, NOX, CO and HC which allows an estimate of the total fuel consumption and emissions for each part of the mission. However there are slight changes to the MEET Methodology

- Additional aircraft types e.g. Boeing B737-400, B737/500/600/700/800, B747-400, ATR42, ATR72, BAe 146,
- Emission Indices were harmonised with ANCAT/EC2 data within UNECE Emission Inventory Guide Book,
- Additional fuel consumption and emission functions, for climb to 3000 ft and final approach down from 3000 ft, which are necessary to calculate ground related emissions
- Additional fuel consumption and emission functions, for climb to 3000 ft and final approach down from 3000 ft, which are necessary to calculate ground related emissions are added for ICAO category.
- For long distance step cruise was included in this computer tool as it is known from the ANCAT/EC2 global NOX emission inventory.

3.1 *Cluster screen*

When generating an emission inventory it is important to have a tool that helps to group air traffic movement data. Some users might wish to make an inventory for a whole country but airport-wise. In this case it is recommended to define each airport as an emission cluster and put movement data of this specific airport of a certain year into this cluster. What you will get at the end is emissions per airport (=cluster).

So the emission cluster concept is a most effective and useful way to input and maintain movement data. The emission cluster can be defined individually depending on the specific question to be answered.

3.2 *Single Aircraft screen*

Based on Eurocontrol data, average flight altitudes for each aircraft and distance of mission were added to the AvioMEET software tool. The user has the ability to use own data with this program. Figure 8 shows the software’s input screen. For an aircraft/engine combination selected an emission profile is generated for the components:

- Fuel Consumption and its related species CO_2, H_2O and SO_2, NO_X, UHC, CO.
- The minimum input data to generate such an emission profile is
- Aircraft type, number of aircraft (of this type) on this mission, distance of mission in km
- From the AvioMEET database defaults are proposed for:
- Cruise altitude in ft, time for taxi out and taxi in for the COST 319 category LTO-cycle , percentage of total cruise distance at a certain cruise altitude, seat capacity and load factor.

The main outputs from the tool are:

- Fuel consumption and emissions for the COST 319 category,

- Specific fuel consumption and Emission Indices for climb, cruise and descent,
- Fuel consumption, emissions and time for COST 319 category LTO-cycle or for the ICAO LTO cycle,
- Fuel consumption, emissions and distance for cruise and cruise related climb and descent,
- Total fuel consumption and total emissions for 1 aircraft on 1 mission,
- Specific fuel consumption and specific emissions per seat kilometre and passenger kilometre,
- Total fuel consumption and total emissions for n missions of n aircraft.

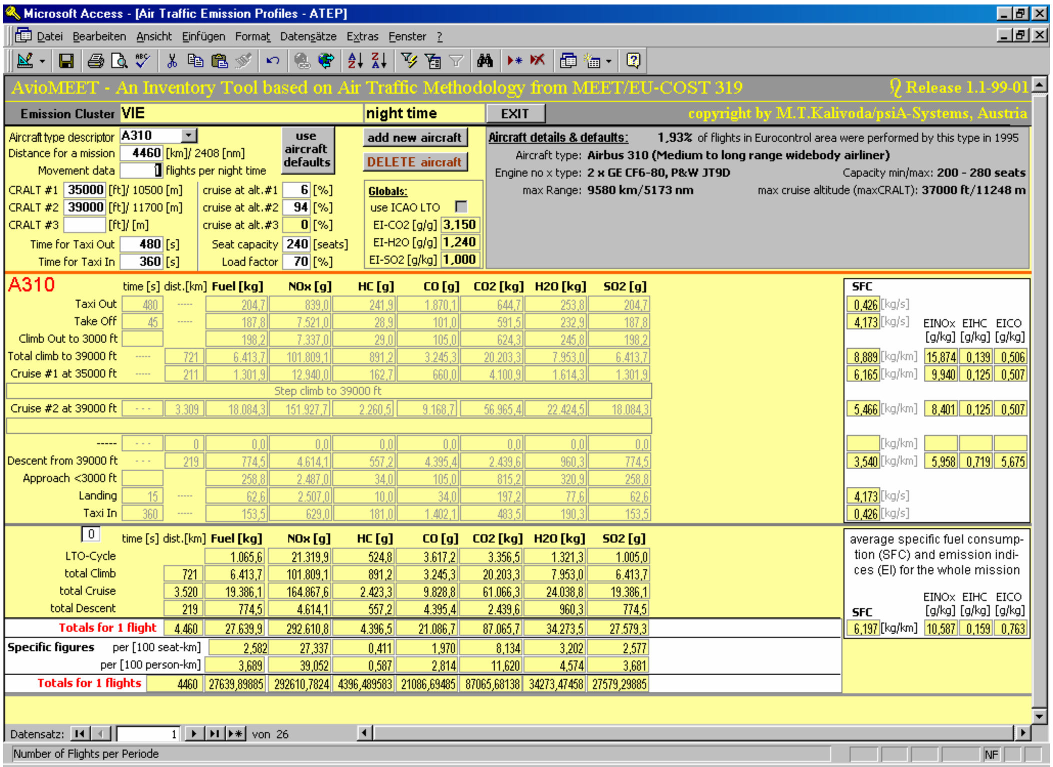

AvioMEET - An Inventory Tool based on Air Traffic Methodology from MEET/EU-COST 319 Release 1.1-99-01

Emission Cluster VIE night time

copyright by M.T.Kalivoda/psiA-Systems, Austria

Aircraft type descriptor A310
Distance for a mission 4460 [km]/ 2408 [nm]
Movement data 1 flights per night time

CRALT #1 35000 [ft]/ 10500 [m]
CRALT #2 39000 [ft]/ 11700 [m]
CRALT #3 [ft]/ [m]
Time for Taxi Out 480 [s]
Time for Taxi In 360 [s]

cruise at alt.#1 6 [%]
cruise at alt.#2 94 [%]
cruise at alt.#3 0 [%]
Seat capacity 240 [seats]
Load factor 70 [%]

Globals:
use ICAO LTO ☐
EI-CO2 [g/g] 3,150
EI-H2O [g/g] 1,240
EI-SO2 [g/kg] 1,000

Aircraft details & defaults: 1,93% of flights in Eurocontrol area were performed by this type in 1995
Aircraft type: Airbus 310 (Medium to long range widebody airliner)
Engine no x type: 2 x GE CF6-80, P&W JT9D
Capacity min/max: 200 - 280 seats
max Range: 9580 km/5173 nm
max cruise altitude (maxCRALT): 37000 ft/11248 m

A310	time [s]	dist.[km]	Fuel [kg]	NOx [g]	HC [g]	CO [g]	CO2 [kg]	H2O [kg]	SO2 [g]	SFC		EINOx [g/kg]	EIHC [g/kg]	EICO [g/kg]
Taxi Out	480	-----	204,7	839,0	241,9	1.870,1	644,7	253,8	204,7	0,426	[kg/s]			
Take Off	45	-----	187,8	7.521,0	28,9	101,0	591,5	232,9	187,8	4,173	[kg/s]			
Climb Out to 3000 ft			198,2	7.337,0	29,0	105,0	624,3	245,8	198,2					
Total climb to 39000 ft	-----	721	6.413,7	101.809,1	891,2	3.245,3	20.203,3	7.953,0	6.413,7	8,889	[kg/km]	15,874	0,139	0,506
Cruise #1 at 35000 ft	-----	211	1.301,9	12.940,0	162,7	660,0	4.100,9	1.614,3	1.301,9	6,165	[kg/km]	9,940	0,125	0,507
Step climb to 39000 ft														
Cruise #2 at 39000 ft	- - -	3.309	18.084,3	151.927,7	2.260,5	9.168,7	56.965,4	22.424,5	18.084,3	5,466	[kg/km]	8,401	0,125	0,507
-----	- - -	0	0,0	0,0	0,0	0,0	0,0	0,0	0,0		[kg/km]			
Descent from 39000 ft	- - -	219	774,5	4.614,1	557,2	4.395,4	2.439,6	960,3	774,5	3,540	[kg/km]	5,958	0,719	5,675
Approach <3000 ft			258,8	2.487,0	34,0	105,0	815,2	320,9	258,8					
Landing	15	-----	62,6	2.507,0	10,0	34,0	197,2	77,6	62,6	4,173	[kg/s]			
Taxi In	360	-----	153,5	629,0	181,0	1.402,1	483,5	190,3	153,5	0,426	[kg/s]			

0	time [s]	dist.[km]	Fuel [kg]	NOx [g]	HC [g]	CO [g]	CO2 [kg]	H2O [kg]	SO2 [g]
LTO-Cycle			1.065,6	21.319,9	524,8	3.617,2	3.356,5	1.321,3	1.005,0
total Climb		721	6.413,7	101.809,1	891,2	3.245,3	20.203,3	7.953,0	6.413,7
total Cruise		3.520	19.386,1	164.867,6	2.423,3	9.828,8	61.066,3	24.038,8	19.386,1
total Descent		219	774,5	4.614,1	557,2	4.395,4	2.439,6	960,3	774,5
Totals for 1 flight		4.460	27.639,9	292.610,8	4.396,5	21.086,7	87.065,7	34.273,5	27.579,3
Specific figures per [100 seat-km]			2,582	27,337	0,411	1,970	8,134	3,202	2,577
per [100 person-km]			3,689	39,052	0,587	2,814	11,620	4,574	3,681
Totals for 1 flights		4460	27639,89885	292610,7824	4396,489583	21086,69485	87065,68138	34273,47458	27579,29885

average specific fuel consumption (SFC) and emission indices (EI) for the whole mission

SFC		EINOx [g/kg]	EIHC [g/kg]	EICO [g/kg]
6,197	[kg/km]	10,587	0,159	0,763

Number of Flights per Periode

Figure 8. MS-Access form ATEPT for emission profiling

4 APPLICATION OF THE MEET/AVIOMEET METHODOLOGY

4.1 *ANCAT/ECAC*

ANCAT (Abatement of Nuisance Caused by Air Transport) represents a group of experts within the European Civil Aviation Conference (ECAC). The ANCAT/EC2 inventories prepared a global air traffic fuel and NOx inventory for base 1991/92 and forecast 2005. A subgroup developed an ANCAT/ECAC methodology for emission calculation were the UNECE methodology. Turboprop data from the ARTEMIS project (5th FP/DG TREN) have been verified and included in the methodology.

4.2 *EMEP/CORINAIR ATMOSPHERIC Emission Inventory Guidebook*

The EMEP/CORINAIR ATMOSPHERIC Emission Inventory Guidebook presents common guidelines for the estimation of emissions from traffic. The methodology presented for air transport (European Environmental Agency EEA 1997) includes three approaches (the very-simple methodology, the simple methodology and the detailed methodology) all based on fuel sold statistics.

Emissions associated with domestic aviation are to be reported to UNFCCC using the IPCC source sector split. International aviation emissions should be presented for information purposes only, but are not included in the national totals. Emissions associated with the LTO-cycle are to be reported to the ECE/CLRTAP. Activities include air traffic movements of scheduled and charter passenger and freight air traffic as well as taxiing, helicopter traffic and general aviation. Military air traffic is included if possible only. The detailed methodology is adopted in accordance with the COST 319 proposal (table above) and emission indices are used from ANCAT/EC2 (fuel consumption, NOx) and MEET (CO, HC).

4.3 *TRENDS*

Trends (TRansport and ENvironment Database System) is a joint DG VII/Eurostat project. The purpose of the study is to develop a system for calculating a range of environmental pressures due to transport. These environmental indicators include air emissions and energy consumption from the four main transport modes, i.e. road, rail, ships and air. These data give a general picture of the absolute environmental loads, in different time and spatial resolutions.

A user software with emission database was developed, where the calculation for air traffic was based on the MEET/AvioMEET methodology. The output of these software are emissions and fuel consumption per person and ton kilometre or per aircraft and engine type for the years 1975 up to 2015.

5 CONCLUSION

From the above discussion it is apparent that COST 319 and MEET were incentives that greatly advanced and harmonised joint activities in Europe in the field of air traffic emission calculation. This can be seen in the manner by which the air traffic community and the environmental community have adopted these Methodologies.

Although the research into calculating emissions and the efforts to harmonise the approach of calculations does not change the impact that emissions have on the environment nor does it make air traffic more environmentally friendly it does create an essential tool for policy making and in deciding which measures have the best effect on the environment.

However, due to the fact that the basic input data for the MEET methodology as well as for AvioMEET software tool are ICAO data from 1995, it should be addressed for decision makers that it is urgent necessary to invest in an update Databank combined with new data available from several influences like real life data, instead of certification data, engine age, weather conditions, as well as inflight emissions.

REFERENCES

Brasseur, G.P. et al.: 1997, European Scientific Assessment of the Atmospheric Effects of Aircraft Emissions, Environment and Climate Programme of the European Commission, October

Bundesamt für Zivilluftfahrt (ed): 1993, Die Auswirkungen der Luftfahrt auf die Umwelt - Synthese. Bern

Bundesamt für Zivilluftfahrt (ed): 1993, Die Auswirkungen der Luftfahrt auf die Umwelt - Kurzfassung. Bern.

EEA (ed.): 1997, EMEP/CORINAIR ATMOSPHERIC Emission Inventory Guidebook – Sub-sector Air traffic, Copenhagen (http:\\www.eea.eu.int).

Gardner R. M.: 1996, A Global Inventory of Aircraft NOx Emissions (ANCAT/EC 2) - A revised inventory (1996) by the ECAC/ANCAT&EC working group. Int. Colloquium Impact of Aircraft Emissions upon the Atmosphere, ONERA, Paris.

Gardner R. M.(ed.): 1998, ANCAT/EC2 Global Aircraft Emissions Inventories for 1991/92 and 2015, ECAC-EC Publication, Eur.No 18179, ISBN 92-828-2914-6,.

International Civil Aviation Organization (ICAO): 1995, ICAO Engine Exhaust Emissions Data Bank, First Edition 1995, Doc 9646-AN/943, Montreal.

Kalivoda M. T., Feller R: 1995, ATEMIS - A tool for calculating air traffic emissions and its application. The Science of the Total Environment 169, 241-247.

Kalivoda M. T., Kudrna M.: 1997, Methodologies for Estimating Emissions from Air Transport, MEET deliverable no.18, CEC DG VII contract ST-96-SC.204, Perchtoldsdorf

Samaras Z. (ed.): 1999, Development of a Database System for the Calculation of Indicators of Environmental Pressure Caused by Transport, Transport and Environment Database System (TRENDS). LAT, University of Thessaloniki, Thessaloniki.

ANCAT/ECAC: 2002, Sub Group on Emissions Calculation, Guidance Material